Okinawa Institute of Science and Technology
Graduate University

Thesis submitted for the degree

Doctor of Philosophy

Investigating color centers in diamond for microwave quantum technologies

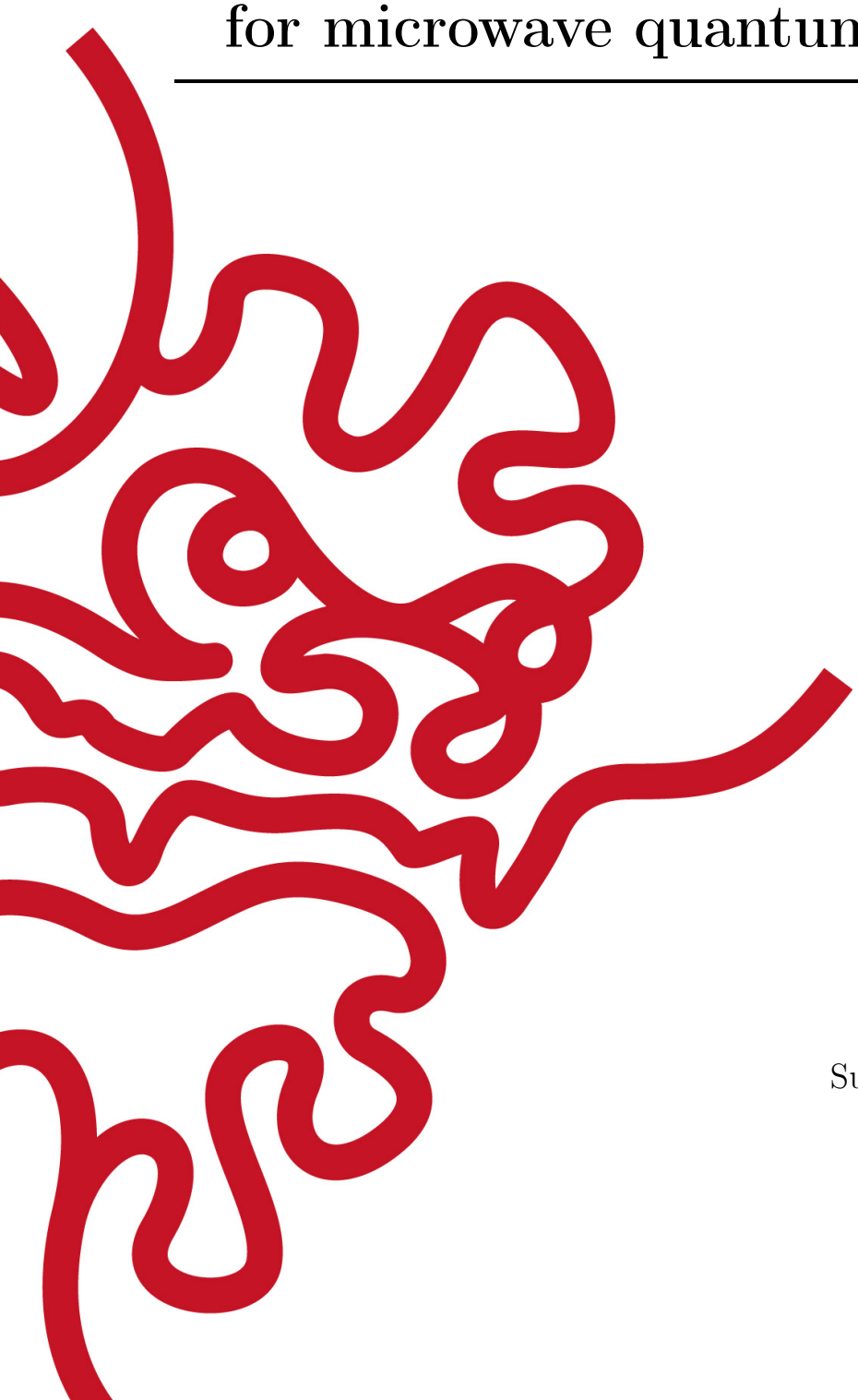

by

Jason Ball

Supervisor: **D. Konstantinov**

August 2021

Declaration of Original and Sole Authorship

I, Jason Ball, declare that this thesis entitled *Investigating color centers in diamond for microwave quantum technologies* and the data presented in it are original and my own work. I confirm that:

- No part of this work has previously been submitted for a degree at this or any other university.
- References to the work of others have been clearly acknowledged. Quotations from the work of others have been clearly indicated, and attributed to them.
- In cases where others have contributed to part of this work, such contribution has been clearly acknowledged and distinguished from my own work.
- None of this work has been previously published elsewhere, with the exception of the following:
  - Jason R. Ball, Yu Yamashiro, Hitoshi Sumiya, Shinobu Onoda, Takeshi Ohshima, Junichi Isoya, Denis Konstantinov, and Yuimaru Kubo, "Loop-gap microwave resonator for hybrid quantum systems," Applied Physics Letters **112**(20), 204102 (2018).

Date: August 2021
Signature:

Abstract

Investigating color centers in diamond for microwave quantum technologies

The rapid advancement of quantum technology in recent years has necessitated the development of many specialized microwave components such as the Josephson parametric amplifier (JPA), to be used in conjunction with superconducting qubits. In this thesis, I present research into impurity spins in diamond, which include nitrogen (P1), nitrogen-vacancy (NV), and vacancy clusters, in particular (R5) centers, for use in these microwave quantum technologies. I first present the development of a 3D loop-gap microwave resonator for use with these impurity spins. We were able to demonstrate strong coupling with an ensemble of nitrogen-vacancy (NV) centers as well as that of nitrogen (P1) centers at 10 mK. I next demonstrate two separate but related maser effects in the spin ensemble. The first of which is a thermally-generated inversion of the NV centers, produced by an abrupt cooling of the sample with a lifetime of several hours. Finally, I demonstrate another spin-based cavity maser, this time using the P1 centers and an active microwave pumping scheme. This cavity amplifier has several desirable qualities, including a large gain and low noise temperature. Such an amplifier may be promising for future quantum technology applications.

Acknowledgment

First of all, I should thank Dr. Junichiro Kono of Rice University and Dr. Keshav Dani, both of whom introduced me and encouraged me to apply to OIST. Without them, the last few years do not happen the same way.

Secondly, I want to thank my thesis supervisor, Dr. Denis Konstantinov, as well as all the members of the Quantum Dynamics Unit as OIST. From our first conversation in February 2015, I was moved by Dr. Konstantinov's enthusiasm for his experiments and quantum physics in general. I have been fortunate to complete my thesis research under such a supportive and knowledgeable advisor.

I would especially like to thank all the past and present members of the Hybrid Quantum Device team within our group, led by Dr. Yuimaru Kubo. Dr. Kubo oversaw most of my research and results and his guidance, input, suggestions, and revisions over the last six years were absolutely essential to the completion of this thesis. Dr. Peter Moroshkin, Dr. Shota Norimoto, Yu Yamashiro, Tatsuki Hamamoto, and Morihiro Ohta also all helped me along the way with experiments and data analysis. Many thanks to the fine people working at Sumitomo Electric Company, as well as Dr. Isoya, for providing our group with the diamond sample from which we obtained our most interesting results, and also to the variety of brilliant researchers I've had discussions with over the years, including Dr. Klaus Mølmer, Dr. John Morton, Dr. Patrice Bertet, Dr. Denis Vion, and many others.

My wife, Virginia, deserves special accolades. I'm not sure she was fully aware of what she was getting into at the beginning of all this, but she has been my rock through it all. I absolutely could not have completed this journey without her love, support, and encouragement, as well as that of our beautiful kids, Helen and Henry. Finally, I would like to thank Darren George, Loretta White, and Dr. Kazuyoshi Yamamoto for helping me take care of myself during the more stressful times of the last few years.

Abbreviations

AC	alternating current
AWG	arbitrary waveform generator
CQED	cavity quantum electrodynamics
CW	continuous wave
DC	direct current
DR	dilution refrigerator
ESR	electron spin resonance
FWHM	full-width at half-maximum
HQD	hybrid quantum device
HPHT	high pressure high temperature
JPA	Josephson parametric amplifier
LGR	loop-gap resonator
MSG	microwave signal generator
NV	nitrogen vacancy (in diamond)
P1	substitutional nitrogen center
QIS	quantum information science
SCQ	superconducting qubit
VC	vacancy cluster
VNA	vector network analyzer

Glossary

Coopertivity	The ratio of the square of the coupling rate g to the loss rates κ and linewidth Γ in a coupled quantum system. Determines the coupling regime of the system.
Decoherence	The relaxation towards zero of the x-y component of the total magnetization vector $\vec{M}$. Limits the storage time of quantum information in the spins.
Dynamic range	The regime of an amplifier where the input power and output power follow a linear relationship. The region begins at input powers above the noise floor and ends at the 1 dB compression point.
Filling factor	The proportion of electromagnetic field strength that the occupies the same region of space as the sample. Mathematically defined as the ratio of the total electromagnetic energy in the sample volume to the total energy within the mode volume.
Gyromagnetic ratio	For a paramagnetic spin in a static magnetic field, the ratio of the energy level splitting (in units of frequency) to the magnitude of the applied field.
Larmor frequency	The frequency of precession of a paramagnetic spin about a static magnetic field, as a result of the field exerting a torque on the object's magnetic moment.
Lattice relaxation	The relaxation of the z-component of the total magnetization vector $\vec{M}$ towards its equilibrium value.
Population inversion	The state of an ensemble of quantum systems where the majority of the population are in excited states.
Quality factor	The ratio of the electromagnetic energy stored in a resonator to the power dissipated in the resonator; equivalently the ratio of the cavity resonance frequency to the linewidth.

Rabi frequency	The rate of cycling between levels in a quantum system as the result of an applied oscillating B-field.
Saturation	The state of an ensemble of quantum systems where the ground and excited states are both 50% occupied; no further photons can be absorbed by the system.
Spontaneous emission	For a quantum system in a non-equilibrium state, the relaxation of an excited state to a lower state, resulting the release of a photon with random phase.
Stimulated emission	For a system in a state of population inversion, the triggering of the release of a photon by an external photon of the same frequency. These emitted photons are coherent with the input photon.
Vacuum field	The electromagnetic field resulting from quantum fluctuations.

Nomenclature

c	Speed of light in a vacuum (299792458 m/s)
γ_e	Free electron gyromagnetic ratio (28 MHz/mT)
$\hbar$	Reduced Planck constant (1.054×10^{-34} Js)
k_B	Boltzmann constant (1.380×10^{-23} J/K)
μ_B	Bohr magneton (9.274×10^{-24} J/T)
μ_0	Permeability of free-space ($4\pi \times 10^{-7}$ H/m)

Table 5: Commonly used symbols in this work

Symbol	Description
$a^\dagger, a$	Cavity photon creation and annihilation operators
$b^\dagger, b$	Bosonic creation and annihilation operators
B_0	static (DC) magnetic field
g_{single}	Single spin-cavity coupling rate
g_{ens}	Ensemble-cavity coupling rate
$\bar{n}$	Number of photons in the cavity
N	Number of spins in ensemble
ΔN	Population difference of spins in ensemble
T_1	Spin lattice relaxation time
T_2	Spin coherence time
T_2^*	Free induction decay time
$\mathcal{V}_c$	Resonator mode volume
α	inversion ratio of the spin ensemble
γ_{rad}	Spontaneous emission rate
Γ	Inhomogeneous broadening linewidth
δB	vacuum AC (alternating) magnetic field
Δ_s	detuning between cavity and spin resonance
η	Filling factor of sample mode volume
θ, ϕ	misalignment angles of the static B-field
$\kappa_1, \kappa_2, \kappa_{ext}$	Loss rates of port 1, port 2, and the combined rate
κ_{int}	Loss rate (linewidth) of the resonator
$K(\omega)$	Spin distribution function
σ_z	Spin angular momentum z-component operator
σ_+, σ_-	Raising and lowering operator of the spin
ω_c, ω_s	Resonant angular frequencies of the cavity and spin
Ω_n	n-photon quantum Rabi frequency

Since I now recall fondly
the painful days of the past
if I live long, I may look back
on these harsh days, too
and find them sweet and good.
- Fujiwara no Kiyosuke

Contents

List of Figures

List of Tables

Introduction

Quantum computing, which falls under the wider umbrella of quantum information science and technology, has advanced rapidly in the last two decades. In that span there have been a wide variety of systems proposed for use as quantum bits (qubits) in a quantum computer. Of these options, systems using microwave frequencies for manipulation and readout, including solid-state spins, spins in semiconductors, and superconducting qubits (SCQ) are popular due to well-established microwave and radiofrequency (RF) infrastructure. [1]

The rapid expansion of this field, due in no small part to massive investments of resources from tech giants such as Google, IBM, Microsoft, Intel, and Amazon, has pushed current microwave technology to its limits. Special (often custom-made) technologies are now required to suit the needs of the experiments performed by companies and academic groups at the cutting edge of SCQ research.

The low energy of individual microwave photons in particular provides a number of experimental challenges to overcome. The energy of a 5 GHz photon is equal to:

$$E = hf = 3.31 \times 10^{-24}\text{J}, \tag{1}$$

which corresponds to a thermodynamic temperature of:

$$T = \frac{3.31 \times 10^{-24}\text{J}}{k_B} = 240\,\text{mK} \tag{2}$$

For comparison, the peak emission wavelength of the sun is $\sim 500\,\text{nm}$ ($\sim 600\,\text{THz}$), which corresponds to a single-photon energy of $4 \times 10^{-19}\,\text{J}$ and a thermodynamic temperature of 30000 K.

This has several important ramifications. The first is that in order for the microwave photons to be in the quantum ground state, measurements involving spin qubits or SCQs must be performed at millikelvin (mK) temperatures, usually necessitating the use of a dilution refrigerator or other cryogenic system. The second is that microwave signals used for qubit manipulation must usually be cooled through several stages of attenuation and amplification during the course of the measurement. Any amplifier will add noise of its own in addition to amplifying any previous noise in the measurement chain. Ideally, the amplifier at the lowest temperature stage should have the lowest added noise as is physically possible. Finally, quantum information coded into microwave photons cannot be removed from the cryostat and transported over long distances, lest it be overwhelmed by thermal fluctuations at room temperature. Since optical frequencies do not have this problem, a device that could efficiently and bidirectionally convert between optical and

microwave photons, a so-called quantum transducer would be necessary for networking between quantum nodes.

It is the particular challenge of quantum-limited microwave amplification that is one of the subjects of this thesis. Quantum-limited amplification of microwave signals at millikelvin temperatures has already been realized through the Josephson parametric amplifier (JPA), which utilizes a chain of Josephson junctions (superconducting tunnel junctions) and a microwave pump to amplify the input signal [2]. Although used in a number of quantum information applications, JPAs do suffer from a few drawbacks, the most significant of which is a low input saturation power. The current state-of-the-art JPAs can theoretically read out about 20 qubits before saturating [3]. As the number of qubits used in QC experiments steadily rises, it will eventually be necessary to measure the state of many qubits simultaneously, which would overpower current technology.

Although only tangentially related to this thesis, the issue of a microwave-to-optical transducer deserves a mention. Contrasted with the JPA, there is no practical solution to this issue at the moment - at least not one with unit efficiency. The current record for efficiency uses an optomechanical resonator to achieve conversion ratios over 47% [4]. Ideas put forth over the years have included other nanomechanical devices [5][6][7], electro-optic sideband conversion schemes [8] and a wide variety of proposals using spins in diamond [9][10], magnons [11], atoms [12],and rare-earth crystals [13]. Williamson's proposal [13] is particularly interesting because it claims that unity efficiency can be achieved using spins of sufficiently narrow bandwidth and high-Q microwave and optical cavities. However, experimental implementations have so far fallen below this goal [14].

It was the idea of a quantum transducer and specifically the experimental implementation of the Williamson proposal that originally motivated my thesis research. Introductions to color centers in diamond and cavity quantum electrodynamics (CQED) are presented in Chs. 1 and 3, respectively, whereas Ch. 2 focuses on the development and history of microwave amplifiers, in particular masers. In Ch. 4 I describe the design, construction, and characterization of a 5-6 GHz microwave resonator, as well as the coupling of the device to color centers in diamond. Although the device was designed to be suitable for microwave upconversion experiments, over the course of the research it was discovered that under certain conditions the population of one particular spin transition of negatively-charged nitrogen vacancies (NV^-) could be inverted, essentially creating a thermally-pumped microwave amplifier, referred to from now on as a thermal maser. This phenomenon and its significance are discussed and analyzed in Chapter 5. Investigation into the mechanism of this thermal maser led to the discovery of another, independent maser effect in the substitutional nitrogen centers (called P1 or C centers) also present in the sample. The mechanism, results, and potential uses for this P1 maser are presented in Chapter 6. Lastly, some perspectives are discussed, including future directions and uses for maser technology.

Chapter 1

Overview of impurity spins in diamond

1.1 Why diamond?

Diamond has long been of interest to researchers in a wide variety of fields. The diamond lattice itself is simple to model and simulate, see Fig. 1.1, and is incredibly robust to any physical wear and tear. Moreover, isotopically engineered diamonds can be magnetically "silent" and thus provide an ideal environment to hold spin centers [15].

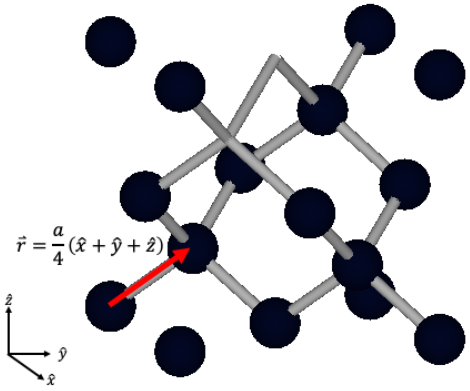

Figure 1.1: The pure diamond lattice, consisting of carbon atoms arranged in two face-centered cubic structures shifted by a/4 along the vector $\hat{x} + \hat{y} + \hat{z}$.

Pure diamond consists of 98.9% carbon-12, 1.1% carbon-13, and trace amounts of carbon-14, and of these only carbon-13 has a nonzero nuclear spin. Impurity spin centers, also commonly known as color centers, are created by the presence of various dopants which replace one or more carbon atoms within the diamond lattice. These dopants can occur naturally or can be specifically engineered using a variety of process. Common impurities include boron, nitrogen, silicon, nickel, and vacancies, although the presence and concentration of these dopants highly depends on the growth method and conditions [16] [17][18] [19].

One of the most popular impurity centers in diamond, negatively-charged nitrogen vacancies (NV^-), have long spin relaxation times (T_1) and coherence times (T_2), which

make them good candidates for storing quantum information [20], even at room temperature. NVs and other colors centers, including silicon vacancies (SiV^-) and germanium vacancies, are incredibly versatile for quantum information applications [21] [22] [23] [24]. Such spin centers have many desirable properties, namely the ability to manipulate the spins via microwaves as well as to readout and reset them via optical frequencies.

In this work we are mostly concerned with NV centers and substitutional nitrogen centers at millikelvin temperatures ($<$20 mK), where the spin relaxation times can reach several hours [25]. These main impurity centers, as well as others that interact with them, are discussed in detail below.

1.2 Negatively-charged nitrogen vacancies

Nitrogen is one of the most commonly-found impurities in both natural and synthetic diamond. When a substitutional nitrogen atom is located adjacent to a vacant lattice site, a nitrogen-vacancy center is formed. Such vacancies are usually formed by electron irradiation, which has other consequences as well, such as production of vacancy clusters (VC). See App. A for details on the specific samples used in the experiments in this thesis. The nitrogen atom provides two valence electrons, while each of the three dangling carbon bonds provide another, as seen in Fig. 1.2. This configuration forms what is known as a neutral NV center (NV^0), a spin-1/2 center. In cases where the system manages to capture another donor electron, usually from another nitrogen atom, then a spin-1 negatively-charged NV center (NV^-) is formed. This thesis concentrates exclusively on (NV^-) centers and will refer to them throughout the work as simply "NV centers."

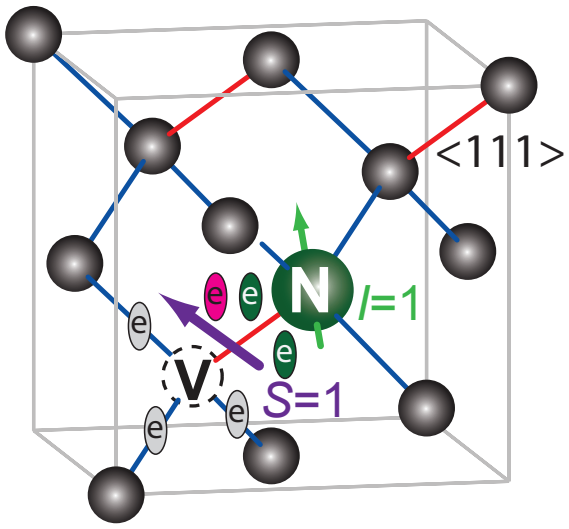

Figure 1.2: The negatively charged nitrogen-vacancy center in diamond, consisting of a substitutional nitrogen with an adjoining vacant lattice site. Three of the six electrons are provided by the dangling carbon bonds (grey), two are provided by the nitrogen atom (green), and one additional donor electron (pink) is captured to form a $S = 1$ spin triplet. The nearby ^{14}N atom has an innate spin $I = 1$ which contributes to the hyperfine splitting of the spin sublevels. The axes in red correspond to the $\langle 111 \rangle$ direction, along which the depicted site is aligned. An NV center may be aligned along any of the other blue-colored axes, with four possible orientations.

The NV center has trigonal symmetry located about the $\langle 111 \rangle$ diamond axis as indicated in Fig. 1.2. Importantly, there are four such equivalent axes in the diamond lattice, meaning that NV centers have four possible orientations. This becomes visible when a magnetic field is applied, as the NV centers can effectively become four subspecies depending on the B-field strength and orientation.

In terms of electronic configuration, the NV center has two unpaired electrons which can form a spin triplet or singlet state. The ground state is the triplet state, commonly referred to as the ^{3}A state. This state is also accompanied by a singlet state ^{1}A and first excited triplet state ^{3}E, see Fig. 1.3. Within the triplet ground state, the spin states $m_s = 0$ and $m_s = \pm 1$ are separated by 2.878 GHz, as shown in figure 1.3. As discussed more in Section 1.2.1, a unique property of NV centers is the spin-selective decay from ^{3}E to the ground states, which allows for efficient optical pumping.

1.2.1 Optical properties

One of the most attractive properties of NV centers is the way that their spin state can be optically pumped into the $m_s = 0$ state by means of radiative decay through a bright state ($m_s = 0$) or non-radiative decay through the metastable singlet state ($m_s = \pm 1$). As depicted in Fig. 1.3, when a 532 nm laser signal is applied to NV centers in the ground state, they are excited to the ^3E state. If an excited spin was initially in the $m_s = 0$ spin state, then it will fluoresce and decay back to the ground state. However, if the spin was initially in the $m_s = \pm 1$, then it will first decay to the metastable dark state ^1A, called

so because no optical photon is emitted during the process. The spin then continues to decay from the ^1A state to the ^3A state, where it populates the $m_s = 0$ sublevel. Using this process, a green laser pulse can pump around 90% [26] of the NV spin centers into the $m_s = 0$ state over tens of nanoseconds [27]. This is an incredibly useful property for applications in both the optical and microwave regimes. It allows the spin populations S_z of NV centers to be probed via optical frequencies in a technique known as optically detected magnetic resonance (ODMR) [28]. It also provides an active reset mechanism for NV centers storing quantum information, allowing the system to be quickly reinitialized.

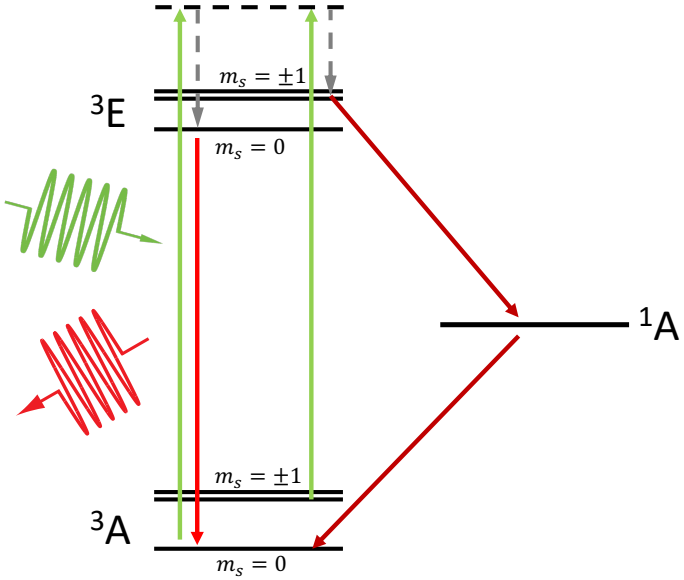

Figure 1.3: The electronic structure of the NV center, consisting of a ground-level spin triplet state ^{3}A, a ground-level singlet state ^{1}A, and an excited state ^{3}E. A green laser pulse can be used to excite the spins from ^{3}A into a higher-energy state above ^{3}E (green arrows), which then relax via phonon processes into ^{3}E. Spins that in the $m_s = 0$ state when they are excited will relax back to the ground state by emitting a photon, as indicated by the red arrows. Excited spins that are in the $m_s = \pm 1$ state will instead decay through ^{1}A in a non-radiative ("dark" path, shown in dark red). Repetition of this process for several cycles will eventually pump the majority of spins into the $m_s = 0$ state, effectively re-initializing the system.

1.2.2 Spin properties

Since the work in this thesis deal primarily with the spin transitions of NV centers, it is important to establish the system Hamiltonian while discussing the contribution of each term. As mentioned above, NV centers are a spin triplet with $S = 1$. We use the spin state basis $m_s = -1, 0, +1$ to characterize the three states. The principle axis ($\hat{z}$) is defined to be along the $\langle 111 \rangle$ axis, and we can use the spin-1 operators in the following

sections, given by

$$\hat{S}_x = \frac{1}{\sqrt{2}}\begin{pmatrix} 0 & 1 & 0 \\ 1 & 0 & 1 \\ 0 & 1 & 0 \end{pmatrix}, \hat{S}_y = \frac{1}{\sqrt{2}}\begin{pmatrix} 0 & -i & 0 \\ i & 0 & -i \\ 0 & i & 0 \end{pmatrix}, \hat{S}_z = \frac{1}{\sqrt{2}}\begin{pmatrix} 1 & 0 & 0 \\ 0 & 0 & 0 \\ 0 & 0 & -1 \end{pmatrix}. \tag{1.1}$$

For NV centers, the spin Hamiltonian has contributions from the zero-field splitting, the Zeeman splitting, and the hyperfine splitting due to the nearby ^{14}N nucleus. Contributions from nearby spin-1/2 ^{13}C nuclei can also be taken into consideration and will be shown in their relevant section. The full Hamiltonian is given by

$$\hat{H}_{NV} = \hat{H}_{ZF} + \hat{H}_B + \hat{H}_{Nuc}. \tag{1.2}$$

The contributions are discussed in detail below.

The Zero-field splitting

The first term in the Hamiltonian arises from the fact that there are two unpaired spins in the NV-center. These spins interact via dipole-dipole magnetic coupling even in the absence of an external field, hence the name it is given. The zero-field splitting term is represented as a 3×3 tensor $\hat{\bar{D}}$ and can be written

$$\hat{H}_{ZF} = \hat{\vec{S}} \cdot \hat{\bar{D}} \cdot \hat{\vec{S}} = D_{xx}\hat{S}_x^2 + D_{yy}\hat{S}_y^2 + D_{zz}\hat{S}_z^2. \tag{1.3}$$

These values are usually redefined as:

$$\hat{H}_{ZF}/\hbar = D\hat{S}_z^2 + E\left(\hat{S}_x^2 - \hat{S}_y^2\right), \tag{1.4}$$

with $D = 3D_{zz}/2$ and $E = (D_{xx} - D_{yy})/2$. The value of D is well-defined at 2.878 GHz [15], which is the value of the energy gap between the $m_s = 0$ and the $m_s = \pm 1$ states. The value E is nominally zero but in reality is local strain within the lattice and thus varies from center to center, and sample to sample. Despite this, the effect of E can be ignored at higher fields (>200 mT), as it is usually $\ll Dz$ [15]. The highly anistropic nature of the D-tensor means that NV centers are extremely sensitive to misalignment of the static magnetic field, with tilts of only a few fractions of a degree producing large shifts in the resonance frequencies. In our system, operating at about 200 mT, the transition frequency shifts by about 1 GHz per degree. This also has the effect of spreading out the transition frequencies of the four NV center orientations, as each can see a slightly different alignment of the B-field. We will use this phenomenon to our advantage in Chs. 5 and 6 to tune the NVs so that their transition frequencies overlap with other spin centers that are less sensitive to magnetic field and orientation.

The Zeeman splitting

As alluded to previously, NV centers are subject to a Zeeman splitting in the presence of a static magnetic field. The magnitude of the splitting is given by

$$\hat{H}_B/\hbar = \gamma_e \vec{B} \cdot \hat{\vec{S}}. \tag{1.5}$$

The g-factor of the NV center is nearly identical to that of the free electron, so the gyromagnetic ratio $\gamma_e = 28\,\mathrm{MHz/mT}$ can be used. The behavior of the energy levels as a function of field for the Hamiltonian $\hat{H}_{NV} = \hat{H}_{ZF} + \hat{H}_B$ in two orientations is plotted Fig. 1.4a-b and merits some discussion. The first point is that the levels change significantly as $\vec{B}$ is tilted further away from the NV $\langle 111 \rangle$ axis, becoming less linear and more quadratic, as seen in Fig. 1.4a-b. The case of 54.7°, namely $B_0 \parallel \langle 001 \rangle$, is plotted in Fig 1.4b, where the $m_s = 0$ and $m_s = -1$ states are strongly mixed for certain values of the magnetic field. This is the standard orientation of the diamond sample used in a majority of this work. See the details of Sample #2 in App. A.

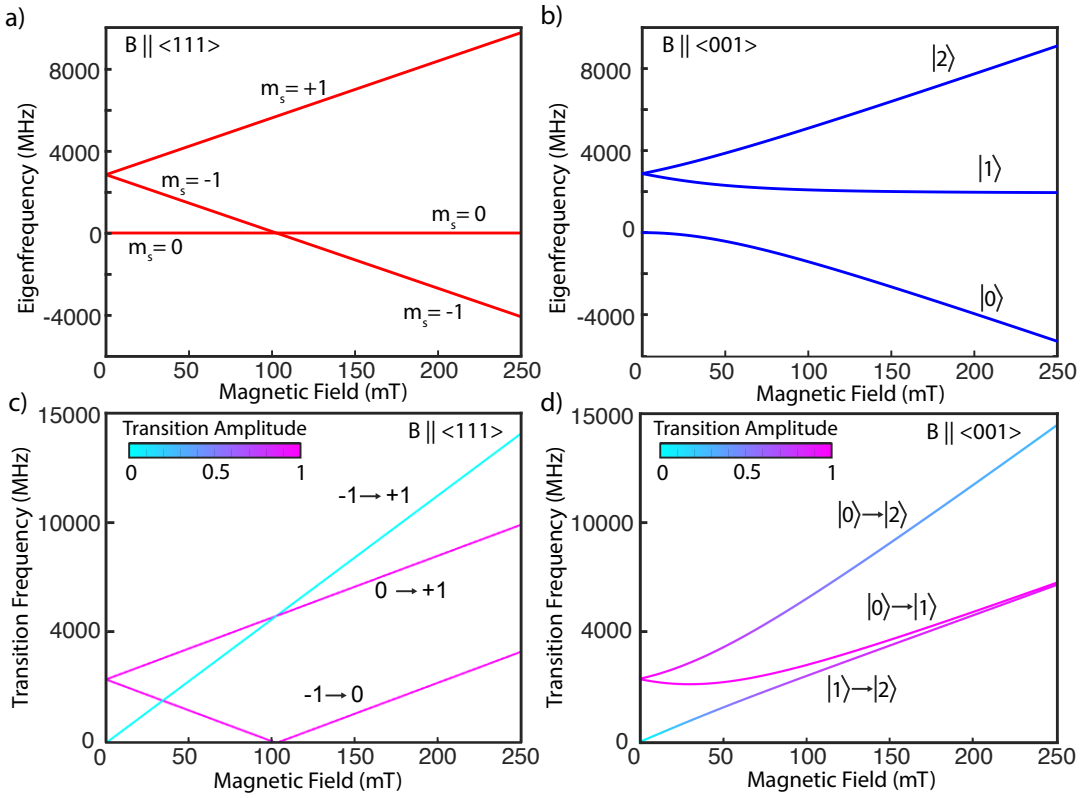

Figure 1.4: Energy level structure of the NV1 center in diamond. a) Energy levels (in units of frequency) as a function of B-field strength. In this case the B-field is applied along the [001] crystallographic axis, as is usually the case in our samples. b) Energy levels as a function of B-field strength when applied along the [111] crystallographic axis. Note the crossing of the $m_s = -1$ and $m_s = 0$ energy levels at $B \approx 102\,\mathrm{mT}$, which become pure states again at higher fields. c) The corresponding transition frequencies between the energy levels of a). Note that initially the lowest-energy transition has an amplitude near zero, as it corresponds to the $\Delta m_s = 2$ transition. However, after the energy level crossing between $m_s = |0\rangle$ and $m_s = |1\rangle$, the amplitude of this transition increases while the highest-energy transition goes to zero. d) The corresponding transition frequencies between the energy levels of b), showing an even starker difference between allowed and forbidden spin transitions, due to the lack of any off-axis B-field component.

An important point about the labeling of NV spin states should be noted here. As determined in the previous section, at zero-field the splitting between $m_s = 0$ and $m_s = \pm 1$ is 2.878 GHz. Adding a static magnetic field breaks the degeneracy of the $m_s = \pm 1$ states via the Zeeman effect. As shown in Fig. 1.4, a spin in the $m_s = 0$ state can be excited into either the $m_s = -1$ or $m_s = 1$ state, but the $m_s = -1$ to $m_s = 1$ transition cannot be driven due to selection rules. As long as the magnitude of the Zeeman splitting is smaller than the zero-field splitting, $m_s = 0$ will remain as the lowest energy state. This is the default configuration of many quantum information experiments using NV centers at room temperature, as it allows for optical pumping into the $m_s = 0$ state. This pumping serves as an active reset mechanism for NV spin qubits. However, as the field magnitude is increased the levels $m_s = 0$ and $m_s = -1$ form an anticrossing at $B_z = D/\gamma_e \approx 102\text{mT}$ (see Fig. 1.4b). The size of this anticrossing depends on the field orientation. In the "intermediate" regime near 102 mT, the mixing occurs between the lower energy levels and the m_s values are no longer good quantum numbers, hence they are renamed $|0\rangle$ and $|1\rangle$ as in Fig. 1.4. As the field is increased beyond this regime, corresponding to transition frequencies in the C-band and higher, the mixing between $m_s = 0$ and $m_s = -1$ states becomes insignificant, so the m_s values are restored as good quantum numbers and the pure state $m_s = -1$ becomes the new lowest energy spin state. This regime, corresponding to Fig 1.4a,c between 180-220 mT and 5-6 GHz, is where almost all of the experiments performed in this thesis take place.

The hyperfine splitting and nuclear effects

Lastly, it is important to note the effect of the nitrogen nucleus on the spin system. Almost every NV center contains a spin-1 ^{14}N nucleus, as the natural abundance of ^{15}N is less than 0.4%. In addition to the hyperfine interaction and its own splitting due to the Zeeman effect, the ^{14}N nucleus also has a quadrupole moment. Thus the total contribution to the Hamiltonian from nuclear effects is

$$\hat{H}_{HF}/\hbar = \gamma_{14N}\vec{B}\cdot\hat{\vec{I}} + \hat{\vec{S}}\cdot\hat{\vec{A}}\cdot\hat{\vec{I}} + P\hat{I}_z^2. \tag{1.6}$$

Compared to the zero-field and electronic Zeeman splitting in our typical working regime, around 200 mT, the contributions from the nuclear effects are rather small. The value of the ^{14}N hyperfine tensor is given by $A_\perp = 2.7\,\text{MHz}, A_\parallel = 2.14\,\text{MHz}$, whereas the quadrupole term has a magnitude $P = -5\,\text{MHz}$. The gyromagnetic ratio of ^{14}N is 3 MHz/T, so the effect of the nuclear Zeeman effect at 200 mT is around $\sim 600\,\text{kHz}$. Since these values can often be similar to the linewidth of the diamond sample itself, it is sometimes difficult to resolve the individual nuclear transitions in cw-ESR experiments. However, these hyperfine transitions can clearly be seen in pulse-ESR experiments.

The calculated energy levels using the full spin Hamiltonian for $B \parallel \langle 111\rangle$ can be seen in Fig. 1.5 below.

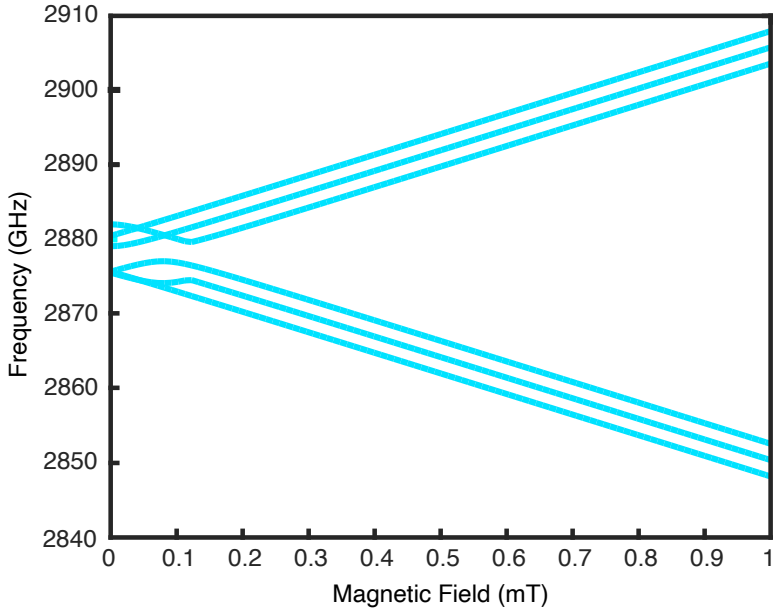

Figure 1.5: The hyperfine levels of an NV center at low field. Assuming the nuclear spin is conserved, this creates three possible transitions between each level.

1.2.3 Applications

The ease of access to NV centers by both optical and microwave frequencies as well as their good coherence times at room temperature mean that NV centers are popular in a vast array of quantum information research, including electric and magnetic field sensing [29], possible use as qubit registers in conjunction with nuclear spins [24][30], and as a multimode RAM for quantum information generated by a superconducting qubit [31][32].

Of particular interest to this work are experiments where an ensemble of NV centers has been inverted and subsequently emit microwave photons. Two such recent experiments come to mind. The first work, by Angerer *et al.*, generated inversion in an ensemble of NV spins by applying a high-power microwave π-pulse [33]. The spin system then underwent superradiance, a collective, coherent emission effect predicted by Dicke in 1954 [34], which was detected by measuring the spin population $\langle S_z \rangle$ via fluorescence (see Sec. 1.2.1). The superradiant nature was confirmed by measuring the power of the emission as a function of the number of spins, N, which was found to have nonlinear behavior [33]. The authors predicted that this device could provide for the basis for a superradiant maser.

NV centers were also the medium of choice for the first demonstration of a room-temperature, solid-state, continuous-wave maser [35]. This experiment, as well as the history and physics of the solid-state spin maser, will be discussed in more detail in the section on practical masers in Ch. 2.

1.3 Substitutional nitrogen centers

The most prominent spin centers in our samples are not, in fact, NV centers but rather substitutional nitrogen centers, known as the P1 center in ESR literature and also some-

times referred to as the nitrogen C center. P1 centers consist of a single nitrogen atom replacing a carbon in the diamond lattice as seen in Fig. 1.6, and are the most common paramagnetic impurity in diamond [36]. The presence of P1 centers in the diamond provides the nitrogen required for the creation of NV centers, hence why, in most cases, the concentration of P1 centers in a given sample is always higher than that of the NV centers.

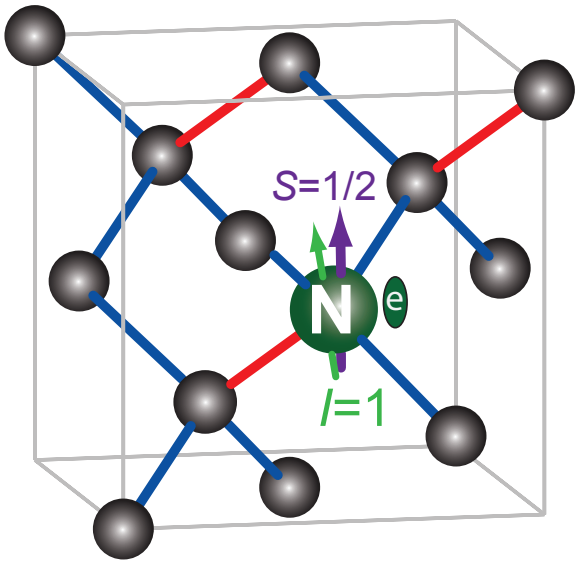

Figure 1.6: The substitutional nitrogen center in diamond, also known as the P1 or C center. The nitrogen atom provides both the donor electron with $S = 1/2$ and the nuclear spin $I = 1$ which form the energy level structure. The axes in red correspond to the $\langle 111 \rangle$ direction. Like the NV center, a P1 center may be aligned along any of the blue-colored axes, with four possible orientations.

1.3.1 Electronic structure and spin properties

Nitrogen is a group-V element, meaning that it has five valence electrons. When a nitrogen atom replaces a carbon atom within a diamond lattice, it introduces an additional donor electron. This electron can be ionized to the conduction band at energies above 2.2 eV (564 nm) [37], resulting in the yellow color of diamonds with a high nitrogen concentration. The electron itself constitutes a spin-1/2 paramagnetic center with a relatively simple spin Hamiltonian, given by

$$\hat{H}_{P1} = \hat{H}_B + \hat{H}_{HF}. \tag{1.7}$$

Like the NV center, the P1 center has a principle axis along $\langle 111 \rangle$ and thus can have four different orientations relative to an applied B-field. Unlike the NV center, though, the spin-1/2 nature of the P1 centers gives it a straightforward, linear energy level structure with no dependence on orientation. Perhaps the most dramatic feature of P1 is its large hyperfine coupling to the ^{14}N nucleus ($A_\parallel = 114\,\text{MHz}$, $A_\perp = 81\,\text{MHz}$), which results in three easily resolvable transitions for each of the nuclear sublevels, as seen in Fig. 1.7.

Although the center transition remains fixed for all orientations of $\vec{B}$ as stated above, due to the anisotropic hyperfine tensor the satellite transitions will broaden and split based on the direction of the applied field (see Fig. 1.7b).

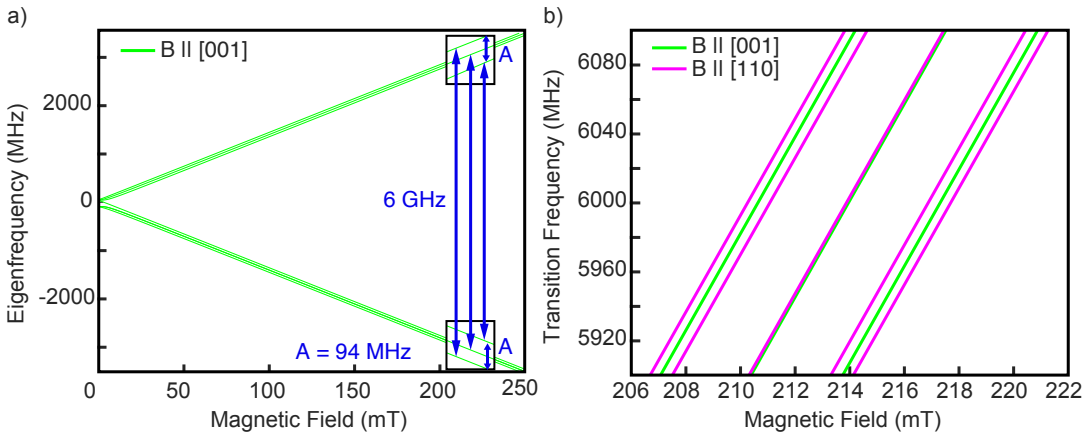

Figure 1.7: Structure of the P1 center in diamond. a) Energy levels (in units of frequency) as a function of B-field strength. In this case the B-field is applied along the [001] crystallographic axis. The transition frequency between the central ($m_I = 0$) levels is 6 GHz at about 214 mT, with the other energy separated by $A/2$ (blue arrows). b) Energy levels as a function of B-field strength when applied along the [001] and [110] crystallographic axes. The pictured region is the typical operating regime of our experiments. While the central transition frequency remains unchanged when the field is applied in the $\langle 110 \rangle$ direction, each satellite is split into two transitions. These correspond to the two different alignments of the P1 centers relative to the [110] plane, those lying in-plane and out-of-plane.

1.3.2 Four-spin cross-relaxation process

Due to its relevance to this work, it is important to describe the four-spin cross relaxation process that occurs among the three nuclear sublevels in P1 centers. This effect was discovered by Sorokin *et al.* in 1959 [38]. At a given value of the static B-field (for $B_0 \parallel \langle 001 \rangle$) the center $m_i = 0$ transition will have a frequency ω_0 and the upper- and lower-frequency satellites will have respective frequencies ω_{-1} and ω_1, as seen in Fig. 1.8. Due to the symmetry of the satellites about the center transition, it is possible for the spins populating these levels to undergo a four-spin "cross-relaxation" process that satisfies the energy-conserving condition $2\omega_0 = \omega_- + \omega_+$. As described in Fig. 1.8, this process can occur in both "forward" and "reverse" directions. If a steady microwave pump signal is applied at frequency ω_0, it is easy to see that all three P1 transitions can eventually be saturated due to this process. It is noted in Ref. [38], though, that population inversion can be achieved if there is any asymmetry in the relaxation times of the system. We use this effect to our advantage to create a microwave amplifier with a sizeable gain and large dynamic range, as detailed in Ch. 6.

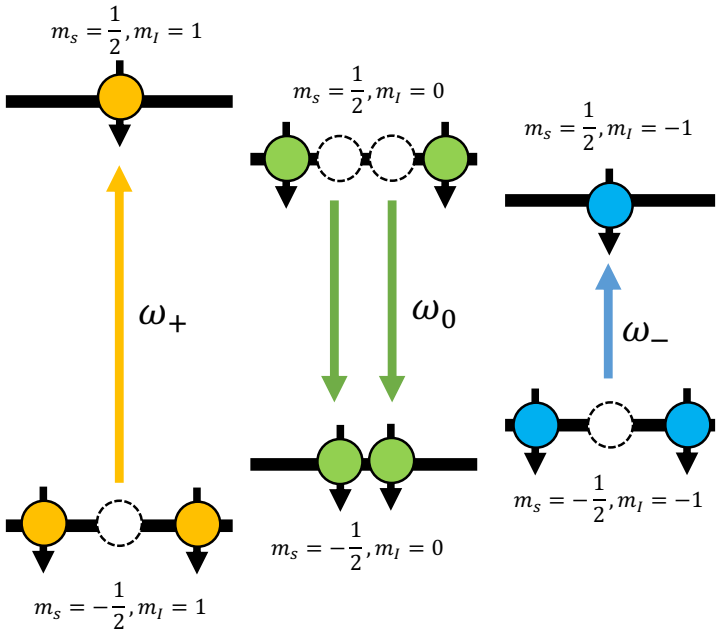

Figure 1.8: Energy level transitions for P1 centers for the magnetic field orientation $\vec{B} \parallel \langle 001 \rangle$. Two spins on the center transition with frequency ω_0 relax from $m_s = 1/2$ to $m_s = -1/2$. This is accompanied by the excitation of one spin on each of the satellites to the $m_s = 1/2$ level, fulfilling the condition $2\omega_0 = \omega_- + \omega_+$. Note that the inverse process is also possible; the directions of the arrows above are reversed and the same energy conservation condition is preserved.

1.3.3 Applications

In general, P1 centers have attracted less research interest than NV centers from the quantum information community. This is primarily due to the lack of optical control and the requirement of a static field $B_>$100 mT, although attempts have been made to control P1 centers optically via their NV counterparts [39]. They have, however, generated some interest as a possible maser medium due to the ability to invert the satellite transition population via the four-spin cross-relaxation process.

Interest in nitrogen-doped diamond was primarily motivated by the diamond mining industry in the first half of the 20th century [40]. The nitrogen concentration was initially determined to be the cause of the UV absorption that differentiated type-I and type-II diamonds [41], however it was later discovered that the UV absorption was not due to P1 centers particularly but to another unidentified nitrogen complex [37]. The ESR spectrum of P1 centers was first detected by Smith *et al.* in 1959 [36]. During the course of these experiments, the group discovered the P1 cross-relaxation mechanism described above could lead to an inverted population on one satellite [38]. Although NV centers constituted the first room temperature cw maser [35], inversion of P1 ESR transitions had actually been witnessed a few years earlier [42] [43], but this phenomenon attracted little further research. The P1 cross-relaxation mechanism was recently investigated in the context of hybrid quantum systems, with the P1 diamond sample coupled to a microwave

resonator [44], although no inversion was achieved.

In the context of quantum information, P1 centers are generally seen as an impediment to the performance of NV centers, as there are always stray P1 centers left behind as byproduct of NV center creation. Studies have been performed examining the effect of P1 centers on the coherence times T_2 and T_2^* of NV centers [45][46] and it is has been found that a higher concentration leads to accelerated decoherence [47].

1.4 Other spin centers

There are many other defects that can create other impurity spins in diamond. Below, we discuss a few specific centers that are confirmed to be present in our sample (see App. A for details), while some centers that may be present but are either unconfirmed or irrelevant to the experiments are gathered under "others."

1.4.1 Double vacancy

The creation of single (isolated) vacancies in diamond is primarily the cause of radiation damage, and is usually purposely done through electron bombardment [18] [48]. When the diamond is then annealed at temperatures above 600-700° C, the vacancies begin to migrate throughout the sample [48]. This migration forms both vacancy chains, and with higher nitrogen concentrations, NV centers. We suspect that some of these vacancies chains are present in our samples and thus some discussion of these vacancy chains is warranted. The first such center to be discussed is the divacancy, consisting of two nearest-neighbor vacancies aligned together along the diamond $\langle 111 \rangle$ plane, as pictured below in Fig. 1.9.

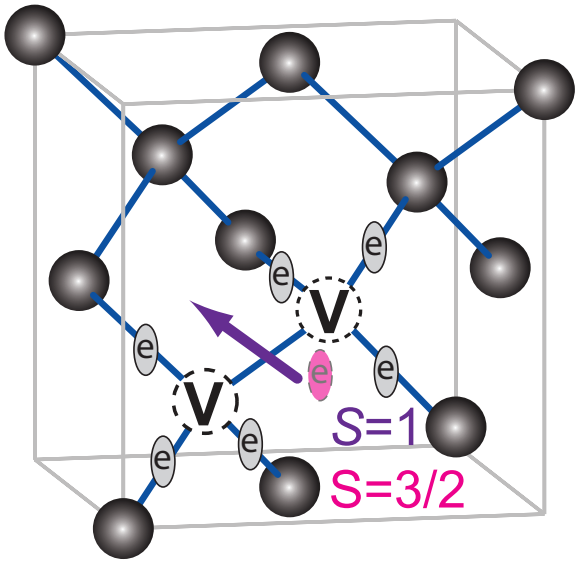

Figure 1.9: The divacancy center in diamond. The charge state $[\text{V-V}]^0$ is also known as the R4/W6 center, which is a spin-1 defect. When an extra electron from another donor (shown in pink) is captured, the center becomes the spin-3/2 $[\text{V-V}]^-$ center, also known as the W29 center. Both charge states have a principle axis aligned closely to the $\langle 111 \rangle$ direction.

Like other defect centers in diamond, the divacancy has multiple charge states. The first is the neutral divacancy, also known as the R4/W6 center, which has spin $S = 1$ [48]. The second is the negative divacancy, known as the W29 center, which captures an extra electron from a nearby donor and thus has $S = 3/2$ [18]. These centers anneal in and out of the diamond at a similar temperature range of 700-1200 K [49], the zero-field splitting terms of their spin Hamiltonians have similar orientations, and both exhibit a temperature-dependent linewidth [18]. The spin parameters for both of these centers, as collected in Ref. [18], are as follows:

Center	Pr. z-axis	D_{zz}	D_{yy}	D_{xx}
R4	[111]	−303 MHz	197 MHz	105 MHz
W29	≈ [111]	−453 MHz	156 MHz	297 MHz

Table 1.1: The spin Hamiltonian parameters for the R4/W6 center and the W29 center in diamond.

We can calculate the energy level structure and the transition frequencies in our specific region of interest, as shown in Fig. 1.10 below. For the [001] orientation of the B-field, some interesting behavior is seen. The transitions of both the R4/W6 and W29 centers are located closely to other $g \approx 2$ transitions such as those of P1 and NV. As the field is tilted into the $\langle 110 \rangle$ direction the degeneracy of all four orientations of the centers is broken and a behavior similar to NV centers is seen. Two pairs of transitions are seen (see Fig. 1.10b) corresponding to the R4/W6 sites orthogonal to and lying in the [110] plane. The spread between these transitions becomes larger for greater values of the D-tensor, as

seen with the W29 transitions of Fig. 1.10d. Under specific magnitudes and orientations of the B-field, it may be possible for the divacancy centers to have resonant transitions with P1 and NV, forming a spin relaxation bath for the long-lived P1/NV centers. As described in Chs. 5-6, these short-lived centers are critical to the functioning of the spin maser amplifier.

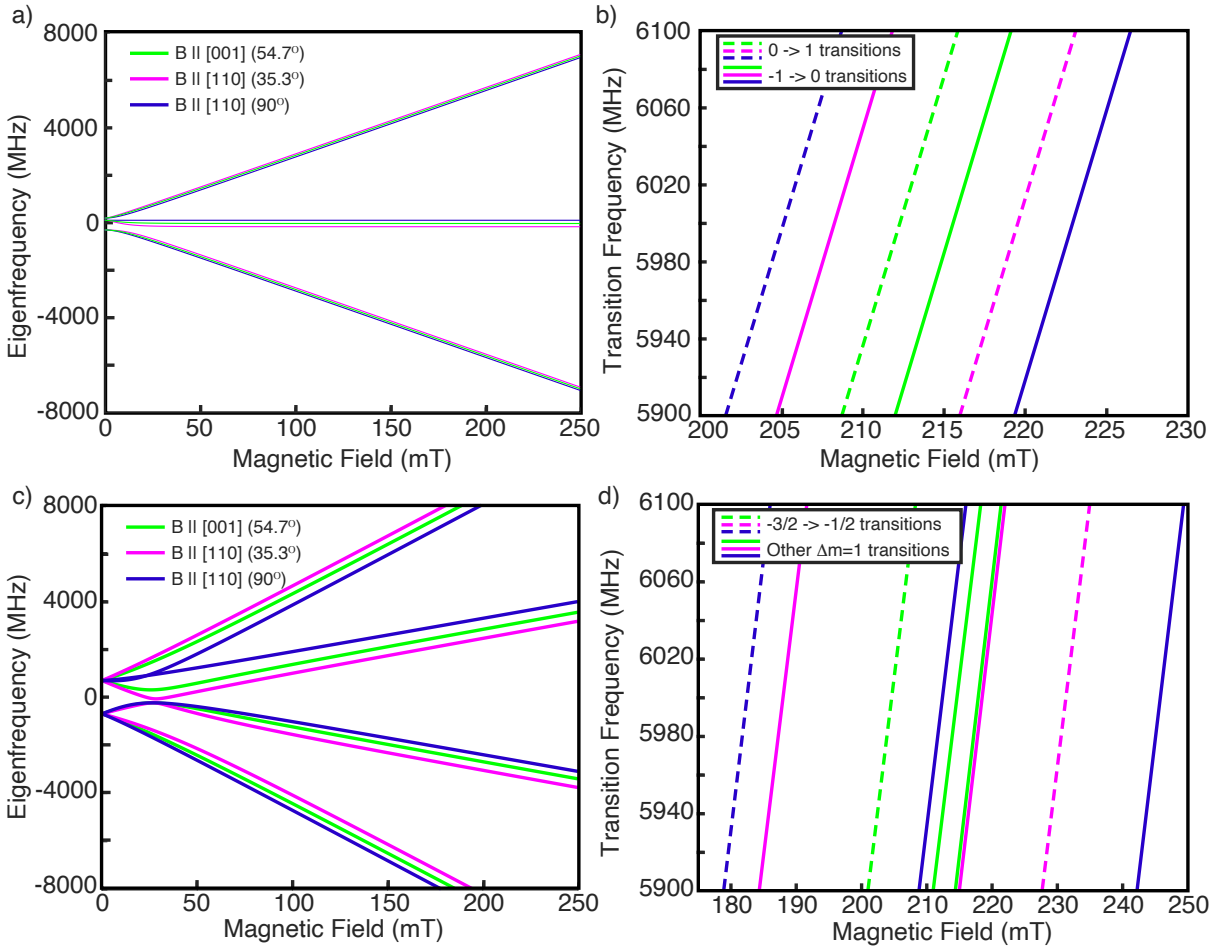

Figure 1.10: Energy levels and transition frequencies of the divacancy centers in diamond for different B-field alignments. a) Energy levels of the $[\text{V-V}]^0$ divacancy charge state (R4/W6). As the field is tilted from the $\langle 001 \rangle$ direction ($\theta = 54.7°$ to the $\langle 110 \rangle$ direction), two species of R4/W6 transitions emerge as the result of the different orientations relative to the [110] plane. b) The transition frequencies of R4/W6 in the region of interest. The ground state transitions ($-1 \rightarrow 0$) of each orientation are indicated with dashed lines. c) The energy level structure of the negatively-charged W29 center, featuring four levels due to its spin-3/2 nature. d) The transition frequencies of W29 in the region of interest. Note the substantially larger frequency spread of the transitions relative to R4/W6, a result of the larger D-tensor values. The ground state transition ($-3/2 \rightarrow -1/2$) of each orientation is indicated with a dotted line. Unlike the R4/W6 center, there are two other $\Delta m_s = 1$ transitions corresponding to ($-1/2 \rightarrow 1/2$) and ($1/2 \rightarrow 3/2$).

The R4/W6 has a heavily temperature-dependent linewidth above 50 K, the result of a rapid spin-lattice relaxation time [48]. The linewidth decreases to 0.13 mT (∼3.6 MHz) below 33 K. The W29 linewidth follows a similar pattern but with a smaller variation [18]. At the higher temperature (above 50 K for R4/W6), the linewidths are considerably larger than typical spin centers in diamond, which is attributed a fluctuation of the dangling bonds of the vacancies. For both R4/W6 and W29 centers, the defect is thought to be continually switching between different sets of four dangling bonds (out of the six total provided by the nearby carbon atoms) [18]. This results in a huge broadening of the linewidth at room temperature.

1.4.2 Vacancy clusters

When annealed at higher temperatures (>800°), the divacancy centers are annealed out and the vacancies forms chains of three or more. In this work we will collective refer to these centers as "vacancy clusters" (VC) center, all of which have the same general behavior and spin parameters. There are five centers in particular in this family, those corresponding to chains of 3-7 vacancies, known as R5, O1, R6, R10, and R11 centers, respectively. Evidence for chains of 8 or more vacancies exists but the spin parameters are not well-established [19]. We can examine the behavior of this family of centers as they all have $S = 1$ and a principle axis along the $\langle 110 \rangle$ direction. This gives the VC centers a different response to the B-field orientation than the other $\langle 111 \rangle$. In Table 1.2 below, the names given to the vacancy chains are shown, as well as the spin parameters. The only substantial difference among the various VC centers is the decrease of the D-tensor as the number of vacancies in the chain is increased.

Center	Num.	D_{zz}	D_{yy}	D_{xx}
R5	3	−524 MHz	244 MHz	283 MHz
O1	4	−205 MHz	95 MHz	109 MHz
R6	5	−120 MHz	59 MHz	62 MHz
R10	6	−73 MHz	36 MHz	36 MHz
R11	7	−53 MHz	27 MHz	27 MHz

Table 1.2: The spin Hamiltonian parameters for the vacancy chain centers in diamond. The values of the D-tensor generally decrease as the number of vacancies in the chain is increased.

The prevalence of different types of VC centers is strongly correlated with annealing temperature [50]. In our case (see App. A), the annealing temperature of 1000 °C corresponds to the R5 center being the dominant cluster, with the other VCs occuring in much smaller concentrations. In this work, we focus primarily on the R5 (triple vacancy) center as representative of the VC centers as a whole. The structure and energy levels of the R5 center are seen in Fig. 1.11 below.

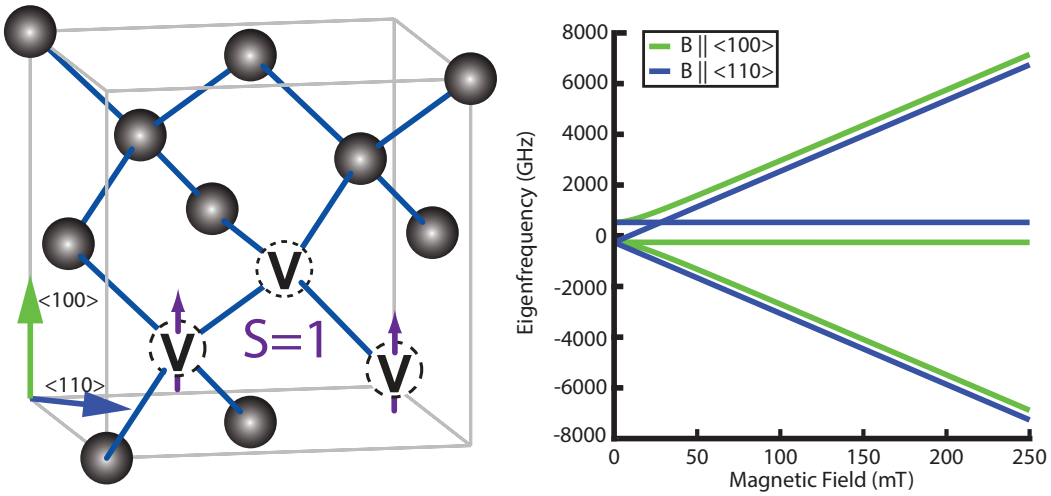

Figure 1.11: The triple vacancy (R5) center in diamond. a) The structure of the R5 center, showing the three vacancies aligned along the ⟨110⟩ axis within the diamond lattice. b) Energy levels (given in terms of frequency) as a function of the static B-field. The other VC centers have similarly-structured energy levels with the zero-field splitting being the only difference.

Similar to the calculations made for the R4/W6 and W29 centers, it is useful to plot the transition frequencies in our area of interest to see if these VC center transitions overlap with the transitions of other defect spins. In Fig. 1.12 below, transition frequencies for all five of the VC centers are plotted for the ⟨110⟩ and ⟨001⟩ orientations of the B-field. Interestingly, when the B-field is tilted into the ⟨001⟩ direction the energies of the $-1 \rightarrow 0$ transitions become lower than that of the $0 \rightarrow 1$ transitions. The presence of ground-state transitions at higher field values such as with VC centers means that they have interesting interactions with the NV and P1 centers, which will be explored in later chapters. The spread of energy levels is also much larger for the ⟨001⟩-aligned field, and it is the R5 center that shows by far the largest effect (see Fig. 1.12). Therefore, the R5 center transition frequency is the most responsive to "tuning" by adjusting the angle and magnitude of the B-field.

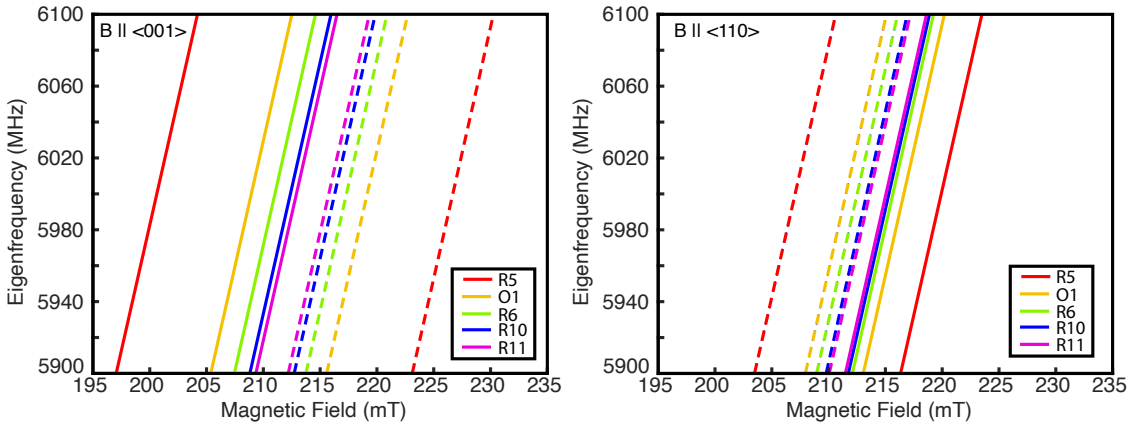

Figure 1.12: Vacancy cluster transition frequencies as a function of B-field. a) The transition frequencies of the R5, O1, R6, R10, and R11 centers in our region of interest. Transitions from $-1 \rightarrow 0$ ($0 \rightarrow 1$) are indicated with dotted (solid) lines. b) Tilting the B-field from $\langle 001 \rangle$ to $\langle 110 \rangle$ results in a shift of the transition frequencies, with R5 having the largest effect and subsequent centers having a smaller effect.

Like R4/W6 and W29, the linewidth of vacancy cluster centers is quite large, around 0.2-0.5 mT (6-14 MHz) [19] at room temperature but decreasing as the temperature is lowered. This homogeneous broadening of the R5 and R4 linewidth at room temperature is due to the rapid lattice relaxation time T_1, which in this temperature range is dominated by Orbach processes [19]. For the R5 center in particular, the linewidth decreases to around 0.1 mT at temperatures below 50 K. It has also been found that the R5 D-values have a temperature dependence - something that has not been observed for the other VC centers [19]. The characteristics of VC clusters at millikelvin temperatures, including the values of D, the linewidth, and the lattice relaxation time T_1, are currently unknown.

1.4.3 Carbon-13 nuclear spins

Diamond consists of 98.9% carbon-12 and 1.1% carbon-13, of which carbon-13 has a nuclear spin $I = 1/2$. Thus, it is possible that any given spin center discussed above could be located near a carbon-13 nuclear spin. The nuclear hyperfine interaction of the defect center with the carbon-13 spin doubles the number of energy levels, splitting each into two further sublevels. The magnitude of the splitting depends on the location of the carbon-13 atom relative to the defect spin, i.e. whether it is a nearest neighbor, next-nearest neighbor, and so far. For NV and P1 centers, the carbon-13 hyperfine tensor values are well-established [51]. The nearest-neighbor carbon-13 interaction has by far the largest hyperfine interaction, with the splitting from other neighboring sites becoming smaller as the atom is further removed from the spin center. As seen in figure below, in experimental ESR data it is common to see faint satellites appear on either side of a given NV/P1 transitions, separated by about 100 MHz.

Like with NV and P1 centers, the orientation of the carbon-13 atom relative to the B-field is crucial, and can result in multiple transitions due to different alignments. For example, when the B-field is aligned along the $\langle 110 \rangle$ axis, not only are two pairs of NV

spin subspecies seen, but each subspecies has two pairs of satellites due to the differing orientations of the nearest-neighbor carbon-13 relative to the NV center. This can quickly make identification of spin transitions quite complicated.

Although research has attempted to harness spin centers coupled to carbon-13 atoms as a tool (e.g. [24][30]), carbon-13 is primarily responsible for the accelerated decoherence of spin defects. At high nitrogen concentrations, spin-spin interactions between the defect centers themselves are the main mechanism of decoherence, but below a certain concentration carbon-13 atoms become dominant [47]. Isotopically purified carbon-12 diamond is thus the most desirable for experiments requiring long coherence times [32].

1.4.4 Others

Other possible impurities in the diamond include single vacancy centers (V^{-1} or GR1 centers) [17] created by electron irradiation, catalyst materials such as nickel, chromium, and iron [52] and silicon [19]. It is expected that most of the single-vacancy centers are annealed out of the sample at temperatures higher than 700-900 K, forming NV centers, double-vacancies, and multi-vacancies instead. Substitutional nickel centers, which form a spin-3/2 system, may be present in the sample with the $\Delta m_s = 1$ transitions in the same general region as P1 and NV1. However, nickel absorption lines have found to be isotropic (i.e. $D \approx 0$ [53]), so they have very little response to B-field misalignment and are thus not expected to contribute to the spin interactions described in later chapters.

1.5 Summary

Diamond is an incredibly rich host medium for paramagnetic spins. We have explored a number of these spin defects that are present in our samples. As will be seen in Ch. 2 multiple species of spin defects have been used previously in conjunction for a variety of interesting effects. If a particularly "fast" system (i.e. R4/W6 or R5) is paired in the correct way with a "slow" (P1 or NV) system, then population inversion can be achieved in the slow system. The challenge, then, is to engineer the system in such a way that two spin species can cooperate. See Chs. 5-6 for more details.

Chapter 2

Microwave amplification and the maser

2.1 History of the maser

2.1.1 Early proposals and demonstrations

In his 1917 paper, Albert Einstein described the process by which a quantum oscillator can undergo a transition from a higher energy state m to a lower state n by interacting with a radiation field, which frees a photon of energy $E_m - E_n$ [54]. Einstein called this process *Einstrahlung*, now known as *stimulated emission*. Over 30 years later, Basov and Prokhorov described the theory of what they dubbed a "molecular generator," a device that used a high-Q resonator in conjunction with a molecular beam, prepared so that the majority of the molecules are in the upper energy states. The cavity field helps drive the state transitions, creating a positive feedback loop [55]. As long as the power dissipation in the resonator is sufficiently low, the device could not only amplify an applied radiation field, but self-oscillate (i.e. generate a field of its own). This is widely recognized as the first theoretical proposal of microwave amplification by stimulated emission of radiation, or maser [56]. The challenge then for experimental implementation was how to prepare (invert) a system so that it was capable of emitting radiation. In 1954 the first experimental realization of a maser came from Gordon and Townes, using an ammonia beam to generate a 24 GHz microwave signal [57]. The physics of this maser are discussed in more detail in the section below. In summary, the device uses a focused beam of ammonia molecules to produce a self-oscillating microwave signal at around 10 nW (estimated) [57]. Even in cases where the masing threshold is not met, the device can still function as a microwave amplifier. This breakthrough resulted in Townes, Basov, and Prokhorov being jointly awarded the 1964 Nobel Prize in Physics. For a brief time, there was a period where many different types of masers were proposed. Potential uses for a maser as a microwave amplifier, spectrometer, frequency reference, and a microwave source were suggested, with narrow bandwidth and low noise figure cited at its most appealing features [58]. We discuss some of these permutations of masers in the next section.

2.1.2 Common types of masers

As noted above, the first working maser by Gordon *et al.* used a beam of ammonia molecules focused through a quadrupolar EM field. Ammonia (NH_3) molecules have an

innate electric dipole moment due to the orientation of the nitrogen atom relative to the three hydrogen atoms. When these molecules enter into the quadrupolar electric field, the orientation of the field forces the lower-energy ammonia molecules in the outer radial direction while the high-energy molecules remain in the center. They are fed into the resonant microwave cavity where the energy is emitted at around 24 GHz [57].

Hydrogen was proposed as a gaseous maser medium by Kleppner *et al.* [59] and later patented [60]. The proposal rests on the innate hyperfine splitting of the hydrogen electronic structure, which are separated by $\sim$ 1.42 GHz. The hydrogen particles are passed through a magnetic state selector similar to the resonant cavity. One of the more enduring maser designs, the hydrogen maser is still used as a frequency reference today.

Solid-state masers using paramagnetic spins also present an interesting medium for maser devices, and likewise several systems were investigated in the 1950s-1960s. The first proposal for such a device was published by Bloembergen in 1956, with the system of choice being gadolinium (Gd) ions in salts. The primary advantage of such a paramagnetic system was the ability to tune the output frequency of the maser via the external magnetic field [61]. However, using solid-state spins requires the cooling of the sample to liquid helium temperatures or lower in order to extend the spin relaxation time T_1 by reducing lattice vibrations. Indeed, when the first demonstration of a solid-state maser was performed by Scovil *et al.*, the system had to be performed in a helium cryostat at 1.2 K [62]. Using Gd ions ($S = 7/2$) in ethyl sulfate, an effective three-level system was created using a B-field of 0.29 T. When a pump tone of 17.5 GHz was applied at sufficient power, a self-oscillating output field of 9 GHz was measured from the cavity [62]. The schematic is seen in Fig. 2.1. The highest output power of the maser was measured to be around 18 μW (*c.f.* the 10 nW obtained by Townes [57]).

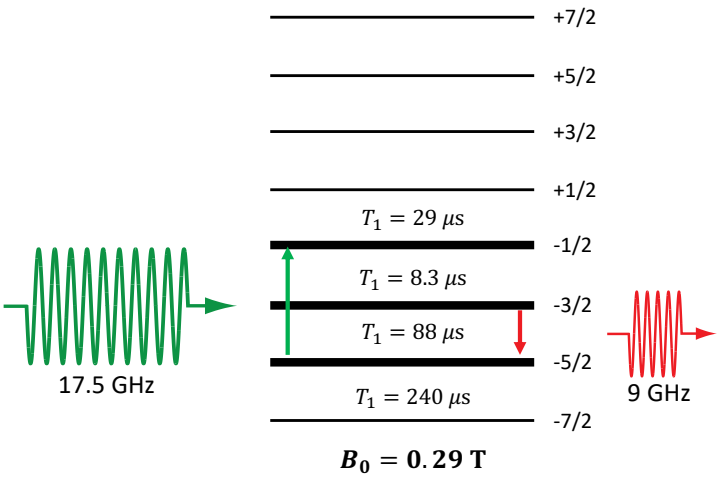

Figure 2.1: The first operating solid-state maser as demonstrated by Scovil and Schulz-DuBois. The energy levels of the spin-7/2 Gd^{3+} ions are shown with the respective lattice relaxation times for each level. This schematic represents an archetypal pumping scheme for lasers and masers, consisting of a three-level (or more) system with a difference in relaxation times between the levels. When the spins are pumped from the first level to the third level, the short lifetime allows the spins to accumulate in the middle level, creating inversion.

Ruby, consisting of chromium ions in sapphire, became a popular medium for masers, owing to its large number of spin-3/2 Cr ions [63], narrow linewidth, and convenient zero-field splitting [64]. Chang *et al.* demonstrated a cavity ruby maser amplifier with an output frequency of 2.74 GHz and a gain-bandwidth product of approximately 50 MHz; however they admitted that the operation of the maser was unstable [65]. The same work proposed and demonstrated a traveling-wave circuit design, also using ruby. In this case, the resonant cavity is replaced by a slow-wave transmission line which results in a large gain-bandwidth [1] [66]. In this design, the gain is dependent on the length of the slow-wave structure and the bandwidth is only dependent on the natural linewidth of the sample [65][66]. This improves its performance over a cavity maser, where it was estimated that the equivalent cavity maser would need a gain-bandwidth product of over 500 MHz for the same performance [65] Lastly, the estimated added noise of these amplifiers was extremely low, on the order of $T_N \sim \frac{S(\omega)}{k_B}$, where $S(\omega)$ is given by the outpower power per bandwidth $P_0/\Delta f$.

One interesting item of note is that the estimated input saturation power of both the cavity maser and traveling-wave design, around -50 dBm, was deemed "low" at the time [65], whereas on the scale of our experiments this value is extremely high and indeed one of the main advantages of a solid-state maser amplifier over its competitors.

Another ruby maser was demonstrated by Arams and Okwit near-simultaneously with Chang's work [64]. Their experiments focused on making a tunable maser and achieved a tuning range from 850 MHz to 2 GHz. This was achieved by using a typical X-band (~ 9 GHz) waveguide with a dielectric rod inserted to provide the necessary L-band ($\sim 2-4$ GHz) resonance [64]. The length of the the rod can be adjusted externally so that the cavity can be resonant with both the pump and probe frequencies. At helium temperature (1.5 K) the measured gain-bandwidth product for this three-level operation was 37.5 MHz [64].

In Section 1.3 we discussed the P1 cross-relaxation mechanism, orignally predicted by predicted by Bloembergen [67] and first experimentally observed by Sorokin *et al.* [38]. It was noted that the mechanism, by itself, is unsuitable for establishing population inversion, as an applied pump on the center transition will only result in the saturation of all three P1 transitions. However, as will be seen in Chapter 5, the presence of another paramagnetic spin transition resonant with one of the P1 satellites can indeed produce population inversion on the opposite satellite. Curiously, this exact effect was noted in Sorokin's work with the following passage:

> The effect of other impurity lines on the nitrogen spectrum in diamond is in certain samples strong enough to produce a large c.w. inversion of the low field satellite when the center line is saturated. That is, in contra-distinction to the ideal case, represented by sample W-2, in which both satellites drop to zero when the center line is saturated, in roughly half of the more concentrated stones the low field line displays a negative absorption when the pump is set on the center line. The amount of inversion varies from stone to stone; in one sample it was as high as 92%. [38]

Despite witnessing inversion in half of their samples, no maser data is presented in their paper, and the exact nature of the mechanism which contribute to the inversion process

is left unresolved. It is attributed to other impurities within the diamond, something that will be examined further in Chapter 6.

One final type of maser relevant to this thesis is the thermal maser, which was also investigated around the same time period. The first proposal for such a "heat engine" was also written by Scovil, in conjunction with Schulz-DuBois. In their work, a three-level system quantum system is placed in contact with a hot reservoir which can serve as a "pump" from levels $1 \rightarrow 3$ by equilibriating the population between the two levels. Simultaneously, a cold reservoir is place in contact to polarize the spins into level 2 [68]. This results in a gain of population in level 2 and an inversion between 1 and 2, essentially creating a Carnot cycle with efficiency

$$\eta_C = \frac{T_H - T_C}{T_H}. \tag{2.1}$$

The maser efficiency must be smaller than this value [68] [69]. In 1961 Schulz-DuBois obtained a patent for a practical implementation of this heat engine, proposing a sapphire rod with one end inserted into liquid helium and the other end surrounded with a heating element. The center portion of the rod is doped with chromium (i.e. ruby) to act as the maser medium. Like our thermal maser in Chapter 5, this design requires periodic heating and cooling of the sample and cannot produce continuous amplification or oscillation [70]. The authors, however, included a second system to overcome this limitation. Instead of ruby, a scheelite ($CaWO_4$) rod is doped in each section with various materials (erbium, germanium, and gadolinium) in an attempt to engineer the thermal conductivity of the rod to make it frequency selective [70].

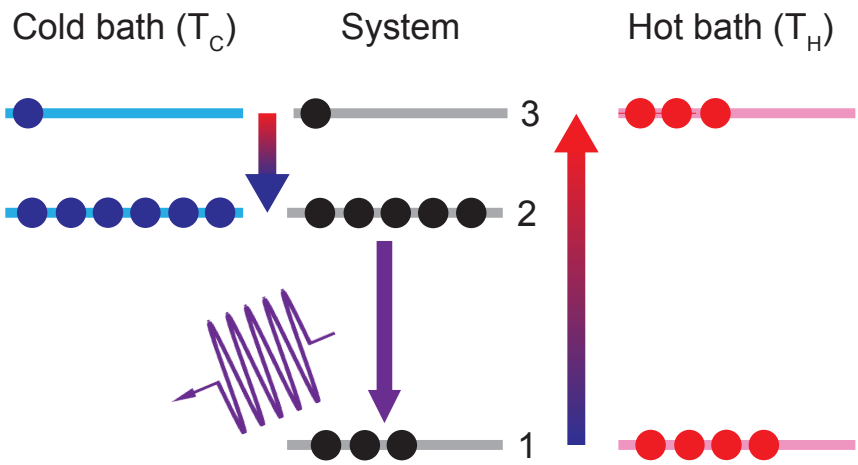

Figure 2.2: The quantum heat engine, as described by Schulz-DuBois in Ref. [68]. A three-level quantum system is coupled to a hot (cold) bath at temperature T_H (T_C). The hot bath, which has the same energy gap as the $1 \rightarrow 3$ system transition, has the effect of populating level 3. The cold bath, which has the same energy gap as the $2 \rightarrow 3$ system transition, has the effect of driving the population from level 3 into level 2. This creates a population inversion between levels 1-2, allowing for microwave amplification or self oscillation.

In 1963 Basov and Oraevskii published a similar proposal for obtaining inversion by rapidly heating and cooling a system, exploiting the differences in relaxation times between different energy levels. The rapid change in temperature functions essentially identically to the thermal baths of the Schulz-DuBois proposal, allowing for a short burst of inverted spin population [71]. This is similar to what takes place within the NV system in our diamond sample, as discussed in Chapter 5.

A few experimental realizations of thermal masers were developed in the 1980s, the first by Vaisfel'd *et al.* using cobalt crystals [72]. By carefully controlling the orientation of a static B-field and applying a perpendicular B-field pulse, they were able to generate spin flip-flops [1] between the Co^{2+} nuclear manifold ($S = 7/2$) and nearby cesium electron spins. This redistributed the populations of the nuclear sublevels so that some were inverted for a brief period of time [72]. A more in-depth study determined that the lifetime of the inverted state is 36 ms [73].

Imamutdinov demonstrated the first thermal maser using ruby and an external heating source, similar to the DuBois patent and depicted in Fig. 2.3. The spin sublevels were prepared at 1.75 K by applying a static B-field of 0.74 T to the ruby crystal, creating an energy gap of 9.1 GHz between the top two sublevels (see Fig. 2.3a). An energy pulse was applied to the crystal via a heating coil, which redistributes the spin population to all levels. Using the natural relaxation times of the ruby, the authors were able to generate inversion between the $+3/2$ and $+1/2$ energy levels with a lifetime of around 800 ms [74] (see Fig. 2.3b) and with an energy conversion efficiency of around 10^{-5}. The incredibly brief lifetimes of these thermal masers proved to be too difficult to overcome, and despite proposals for continuous-wave thermal masers [75], such a device never materialized.

However, the basic idea did live on in what are known as gasdynamic lasers [76]. In a paper describing the connection between thermal masers and gasdynamic lasers, Konyukhov outlines the following. A system of heated gas molecules with a long vibrational relaxation times (N_2) operates in conjunction with other molecules with short vibrational relaxation time (CO_2). The exchange of energy between the fast and slow system is similar in principle to that which occurs in a thermal maser, however the process is reversed and results in population inversion on the CO_2 (the "fast" system).

[1] Vaisfel'd, as well as many of the works cited here from the 1960s-1980s, refer to the process of energy exchange between different species of paramagnetic spins as "cross-relaxation." We appropriate the term "cross-relaxation" for processes taking place within a single defect type, for example the four-spin energy exchange within the three nuclear sublevels of P1 centers. However, in this work we use the term "spin flip-flops" to refer to exchanges between different spin species, and hence the term is applied here and throughout the rest of this thesis.

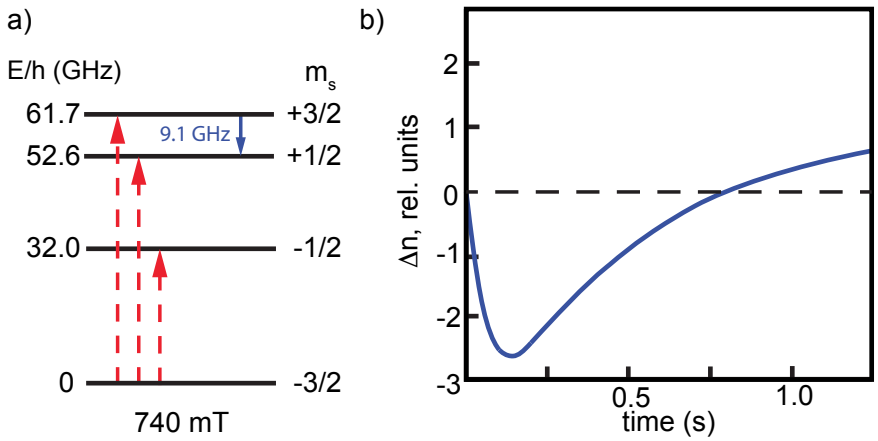

Figure 2.3: Ruby thermal maser implementation by Imamutdinov in Ref. [74]. a) The energy levels in the ruby crystal are set with a 740 mT B-field, creating an X-band frequency gap between the top two levels. A heat pulse redistributes the spins from the ground state to all levels (red arrows). After the pulse is applied, a brief population inversion is achieved between levels $m_s = +3/2$ and $m_s = +1/2$. b) Time-dependent behavior of the relative inversion ratio for the maximum pulse energy of $E = 48\,\mathrm{mJ}$, extracted from the observed ESR signal. The inversion lasts for approximately 800 ms.

2.1.3 Abandonment of masers

Although masers had been initially proposed for a wide variety of uses, including as frequency references, for radio astronomy, and as low-noise microwave amplifiers [58][66], they were hampered by numerous shortcomings. Among these were the difficulty of operation, low power output, and, especially for solid-state schemes, the required liquid helium bath and static magnetic fields. With a few notable exceptions, such as the hydrogen frequency reference [59] and the NASA Jet Propulsion Lab's use of ruby masers for astronomic data collection [77], masers gradually fell by the wayside as more efficient means of achieving similar results were invented. Famously, in 1958 Townes and Schlalow extended maser physics into the optical regime with their seminal work on what were then known as "optical masers," or lasers [78]. In this work, the authors proposed the first laser, using potassium vapor to produce a narrow monochromatic beam of around 400 nm [78]. The work also suggested the possibility of using solid-state crystals as a lasing medium, but acknowledged that at the time an efficient way to pump the crystals was lacking. Despite this, Maiman demonstrated the first operational laser using ruby only two years later [79]. Following this result, lasers, which did not require static magnetic fields, cryogenic operation, or high-vacuum chambers, eventually superseded the maser to become ubiquitous in research labs everywhere. Maser amplifiers and oscillators were generally overcome by semiconductor technology using transistors, which would be developed in the new few decades.

2.1.4 Recent experiments

Interest in maser systems began to resurface in the mid-2000s with the advent of rapidly-developing quantum technology. Spins in synthetic diamond were initially considered as a masing medium with the detection of inverted ESR signals arising from the P1 centers [42] [43]. However, the first demonstration of a room-temperature, solid-state maser was published in 2012 by Oxborrow *et al.* using organic materials, specifcally *p*-terphenyl crystals doped with pentacene. The pentacene is activated with a 585 nm laser, which can then decay non-radiatively via intersystem crossing into a triplet state [80]. This transition to the triplet state is spin-selective and results in an inverted population at the top level, which then undergoes a 1.45 GHz decay to the bottom level of the triplet. Although this system has many attractive features, including room-temperature operation and lack of a need for a static B-field, it was unable to sustain continuous operation [80].

A maser meeting all the following criteria: 1) solid-state, 2) room-temperature, and 3) continuous-wave would be proposed in 2015 by Jin *et al.* and finally achieved in 2018 by Breeze *et al.*, more than 60 years after the first solid-state maser proposals [81][35]. Using the unique optical properties of NV centers, Breeze *et al.* used a 532-nm laser to optically pump the NV centers to the $m_s = 0$ level. At fields above 102.5 mT, the $m_s = -1$ lies below the $m_s = 0$ level, allowing the green laser to act as a pump and producing inversion on the NV centers [35]. At a field value of around 430 mT, the microwave out put signal is 9.1 GHz, in the X-band of frequencies. By using the spins in conjunction with a high-Q microwave cavity, the masing threshold was overcome and produced a total power of around -90.3 dBm ($\sim$ 1 pW), comparable to a hydrogen maser [35].

Another type of micromaser was developed by Liu *et al.* in 2015, this time using double quantum dot (DQD) heterostructures instead of spins. By applying a bias voltage to two DQDs such that the electron tunneling rate to the DQD's upper level from the reservoir is faster than the electron relaxation and the coupling rate to the cavity, (i.e. higher population in the upper level than average), they were able to generate population inversion in the DQDs, resulting in transmission gain and free-running maser action. The total gain ($\times$1000) of both DQDs combined was much greater than the produce of either dot individually [82]. Free-running maser action action was also observed, although with a broader spectrum than predicted by the Schlalow-Townes theorem [82].

Masers, despite their historical importance, have been mostly confined to niche uses for the last 60 years. However, given the growing demand for quantum technology, especially low-noise amplifiers and microwave sources, it may be possible that the maser may see a resurgence in popularity. This would require a solid-state maser which could be operated continuously with microwave frequencies in a low-temperature environment, which excludes some of the more recent maser schematics that are activated with optical frequencies [80][35]. In the next section, we will discuss current low-noise amplifier technology, particularly solid-state (HEMT) and superconducting Josephson parametric amplifier, and end by discussing the potential for a spin maser in such a role.

2.2 General principles of signal amplification

2.2.1 Key properties of an amplifier

Gain and bandwidth

Having a high gain is obviously a desirable property for any amplifier. In reality, though, the highest possible gain is not always desirable as it can result in a number of sacrifices made to other key parameters, especially bandwidth. In simplest terms, the gain is defined as the ratio of the input power to the output power

$$G = \frac{P_{out}}{P_{in}}, \tag{2.2}$$

whereas the bandwidth is defined as the full-width half-maximum, or the difference between the frequencies where the maximum amplifier output is reduced by -3 dB ($0.5P_{max}$). For an amplifier based on a resonator, such as a maser or Josephson parametric amplifier (JPA), the gain and bandwidth are inversely proportional (i.e. $\Delta f\sqrt{G} = \text{const}$).

Thermal noise

Electrons are always in motion. In any circuit, no matter the medium, devices involved, or configuration, there will always be a minimum amount of noise due to the fluctuations of electrons. To quantify the noise due to thermal fluctuations, we imagine the following scenario, seen in Fig. 2.4 and following the derivation of Nyquist [83]:

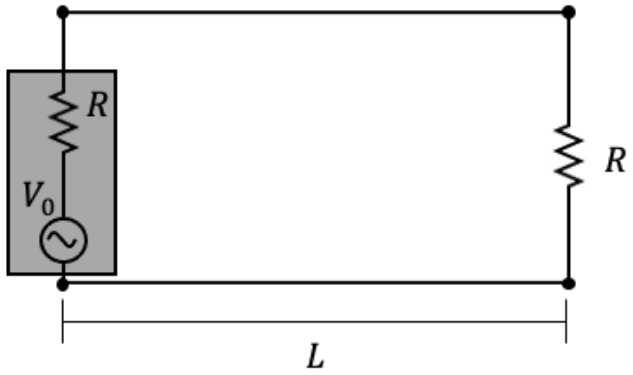

Figure 2.4: Nyquist noise of a simple resistor. The resistor R on the left has noisy electrons at temperature T. A distance L away is a load resistor, also of resistance R, where the power generated by the noisy electrons is dissipated.

The "noisy" electrons are confined to a resistor of resistance R at temperature T, with the noise represented by a fluctuating (AC) voltage, given by

$$V(x,t) = V_0 e^{-2\pi i f t}\cos kx, \tag{2.3}$$

where f is the center frequency of the oscillation and k is the wavenumber, which is related to frequency by the relation

$$k_n = \frac{2\pi f}{c}, \tag{2.4}$$

where c is the speed of light. Another load resistor, R is connected a distance L away to measure the power output of the noisy resistor. For the voltage to be a standing wave, the wavenumber k must be constrained by the condition

$$k = \frac{n\pi}{L} \quad (n = 1, 2, 3, ...), \tag{2.5}$$

which in frequency space corresponds to:

$$f_n = \frac{cn}{2L}. \tag{2.6}$$

The space between successive modes f_n and f_{n+1} is given by $c/2L$, so the number of modes in a given bandwidth Δf, represented as $N_{\Delta f}$, is

$$N_{\Delta f} = \frac{2L}{c}\Delta f, \tag{2.7}$$

which leads to the number of modes per length per bandwidth frequency

$$\frac{N_{\Delta f}}{L\Delta f} = \frac{2}{c}. \tag{2.8}$$

To get the energy, we can then take this quantity and multiply by the number of photons in each mode, and the corresponding energy of each photon. We know from Eq. 1 that the energy of a photon at frequency f is given by $E = hf$. From quantum mechanical principles, we also know that mode occupation at temperature T is

$$\overline{n} = \frac{1}{e^{hf/k_BT} - 1}. \tag{2.9}$$

Putting it all together, we can obtain the energy per length per bandwidth

$$u = \frac{2hf}{c}\frac{1}{e^{hf/k_BT} - 1}. \tag{2.10}$$

Since the energy is split between the two resistors, we must add an additional factor of $1/2$ to calculate the power at the load resistor. Additionally, we know that the distance a wave covers per unit time is equal to c. By multiplying each side of the above by c, we turn the left-hand side from energy per length per bandwidth to power per bandwidth

$$p = \frac{hf}{e^{hf/k_BT} - 1}. \tag{2.11}$$

Finally, we can multiple by bandwidth to get the total thermal noise power emitted by our electrons. This is known as *Johnson-Nyquist noise*, which is

$$P_{noise} = \frac{hf\Delta f}{e^{hf/k_BT} - 1}. \tag{2.12}$$

In the high temperature limit, we can simplify this further by assuming $hf \ll k_BT$. This removes the central frequency dependence and the expression is rewritten as

$$P_{noise} = k_BT\Delta f. \tag{2.13}$$

By looking at this equation we can obviously see that smaller bandwidth and lower temperatures result in lower noise power. Note that while this is a safe approximation for C-band microwave temperatures above 1 K, we will soon see that this approximation breaks down in the quantum regime.

Thermal noise is not the only source of noise, of course, especially in solid-state devices with a high number of charge carriers, which can also fluctuate at random. Therefore, it is convenient to define the *equivalent noise temperature* in order to characterize devices with many different sources of noise.

Figure 2.5: A noise source with equivalent noise temperature T_{eq} and producing noise power P_0, measured with a load resistor of resistance R.

In figure 2.5, an arbitrary source of noise is connected to a load resistor, similar to our earlier example. If a noise power P_0 is measured in a given bandwidth Δf, then using Eq. 2.13 the equivalent noise temperature can be written as

$$T_e = \frac{P_0}{k_B \Delta f}. \tag{2.14}$$

Note that this temperature is not necessarily the actual temperature of the device. Instead, the device produces a level of noise power as if it were a noisy resistor at temperature T_e, and can be treated as such in calculations. This makes comparisons between various devices in a measurement chain much easier, regardless of the actual temperature of the device. The equivalent noise temperature, especially for room temperature electronics, is typically much higher than a noise temperature due purely to thermal fluctuations. For example, a room temperature amplifier at 297 K can have an equivalent noise temperature of ~ 2000 K.

Quantum Noise

One can see a problem with the expression for the Nyquist noise as $T \to 0$, known as the quantum limit. As the temperature approaches absolute zero, the noise likewise goes to zero. This is not correct and is in fact unphysical, as it implies that there is no motion in the system, in violation of Heisenberg's uncertainty principle.

For situations where $T \ll \frac{hf}{k_B}$, the system will mostly reside in its quantum ground state. For the case of a quantum harmonic oscillator, the zero-point energy is given by

$$E_{ZP} = \frac{hf}{2}. \tag{2.15}$$

The total noise in a system, then, is the sum of the Johnson-Nyquist noise and the zero-point (or quantum) noise, or

$$P_{total} = hf\Delta f \left(\frac{1}{e^{hf/k_B T} - 1} + \frac{1}{2} \right). \tag{2.16}$$

The power spectral density $P/\Delta f$ is plotted in Fig. 2.6 below as a function of T, assuming a C-band microwave frequency (6 GHz).

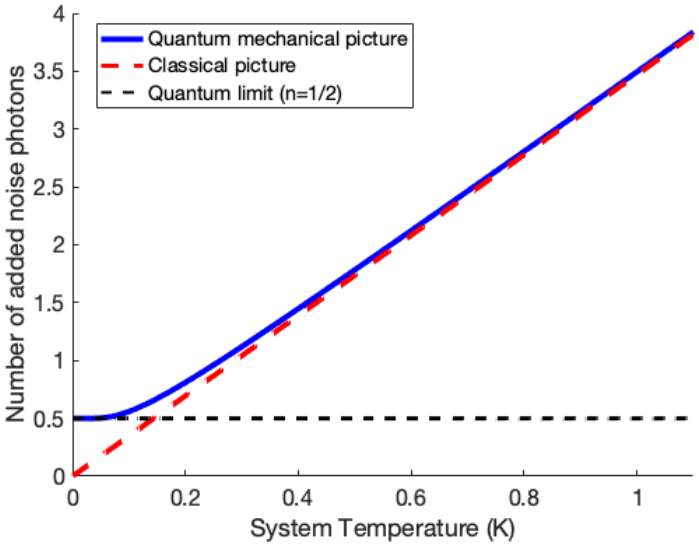

Figure 2.6: Noise power per bandwidth as a function of temperature for a fixed frequency $f = 6\,\text{GHz}$. At high temperature the function closely follows the linear relation $P_0 = k_B T$, but diverges at low temperature, reaching a minimum value of $hf/2$.

Dynamic range

If the power being fed to an amplifier is gradually increased, it is impossible for said amplifier to continue amplifying indefinitely. Thus, an important characteristic of an amplifier is its *dynamic range*, or the range of input powers over which the amplifier outputs a signal with gain in a linear fashion. An illustration of the dynamic range can be seen in Figure 2.7. The lower bound of the dynamic range is given by the noise floor, or the noise added by the amplifier itself. The upper bound is when the output signal begins to deviate from the ideal amplifier, called *compression*. A measure often used to define compression is the 1 dB compression point, which is the input power where the real output differs from the ideal amplifier curve by 1 dB. Going far above the 1 dB compression point can damage or destroy the amplifier. Cryogenic amplifiers, such as HEMTs and JPAs, have a small dynamic range and can be easily saturated by powerful microwave signals [3], such as those used in pulse-ESR experiments.

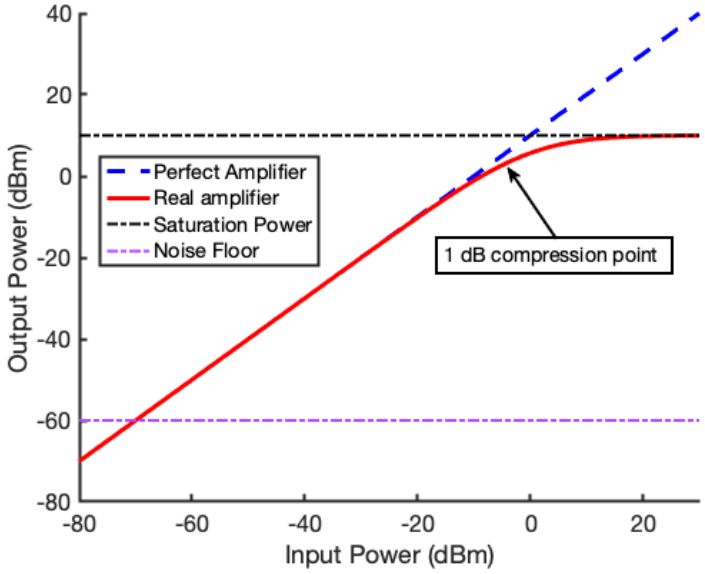

Figure 2.7: Output versus input power for an amplifier of $G = 10\,\mathrm{dB}$. At low input power the noise floor overtakes the signal. Above the noise floor, the input and output enter a linear regime, which then begins to break down at higher temperature. The dynamic range and 1 dB compression point are indicated.

Amplifier chains

A typical microwave spectroscopy measurement setup, including those used in this thesis, usually has several stages of attenuation and amplification. If the noise temperature of each individual stage is known, then the noise performance of the entire chain can be found. In our case, imagine the cw dilution refrigerator setup as described in Fig. B.1 of App. B. Before reaching the input port of the VNA, a signal with noise power N travels through a room temperature amplifier, where the signal is amplified with a gain of G_0. Thus we can calculate the output noise power N_0 via the expression [1]

$$N_0 = G_0(N_1 + N_{added}). \tag{2.17}$$

As we described in the previous section, the room temperature amplifier adds its own noise to the signal while amplifying the noise of the previous stage. We know that the added noise can be represented by the noise temperature as in Eq. 2.13:

$$N_0 = G_0(N_1 + k_B T_{e,0} \Delta f). \tag{2.18}$$

Where $T_{e,0}$ is the equivalent noise temperature of the room temperature amplifier. The input noise, N_1, is the product of the *previous* amplifier stage (in our case at 4 K),

$$N_1 = N_{4K} = G_{4K} k_B T_{e,4K} \Delta f, \tag{2.19}$$

where we assume, for the moment, that no signal is being transmitted from previous stages through the 4 K amplifier. Combining with Eq. 2.18, we obtain

$$N_0 = G_0(G_{4K} k_B T_{e,4K} \Delta f + k_B T_{e,0} \Delta f), \tag{2.20}$$

which can be rewritten

$$N_0 = G_0 G_{4K} k_B \Delta f \left(T_{e,4K} + \frac{T_{e,0}}{G_{4K}} \right). \tag{2.21}$$

Comparing this with Eq. 2.13, we can define the total gain as the product $G_0 G_{4K}$ and the equivalent noise temperature of the two-amplifier chain as

$$T_{e,sys} = \left(T_{e,4K} + \frac{T_{e,0}}{G_{4K}} \right). \tag{2.22}$$

This has some important ramifications. Note that the room-temperature equivalent noise temperature, $T_{e,0}$ is reduced by a factor equal to the gain at the 4 K amplifier. This means that the first amplifier in a given chain, in this case the 4 K amplifier, is weighted much more heavily than subsequent amplifiers in terms of contribution to the overall equivalent noise temperature. If an amplifier were to be added earlier in the chain, for example at the lowest temperature stage of the dilution refrigerator, known as the mixing chamber (MXC), the steps above could be repeated and the equation would become

$$N_0 = G_0 G_{4K} G_{MXC} k_B \Delta f \left(T_{e,MXC} + \frac{T_{e,4K}}{G_{MXC}} + \frac{T_{e,0}}{G_{4K} G_{MXC}} \right), \tag{2.23}$$

which corresponds to an effective system noise temperature

$$T_{e,sys} = \left(T_{e,MXC} + \frac{T_{e,4K}}{G_{MXC}} + \frac{T_{e,0}}{G_{4K} G_{MXC}} \right). \tag{2.24}$$

The amplifier at the mixing chamber has now become the most critical component. Indeed, this is the basis for quantum-limited amplification at the mixing chamber of the dilution refrigerator. By adding the minimum allowed noise at the first amplifier stage, the overall noise of the system is reduced, preserving a signal-to-noise ratio capable of detecting the small powers characteristic of microwave photons.

2.3 Modern amplifier schemes

2.3.1 High-electron mobility transistor

The high-electron mobility transistor (HEMT) amplifier is a type of field-effect transistor, a device that uses a gate electric field to control the conductivity, and thus the flow of current between the source and drain terminals. While the transistor effect was first demonstrated (using a bipolar junction transistor) at Bell Labs in 1947 [84] and the now-ubiquitous metal-oxide-semiconductor field-effect transistor following in 1959 [85], the HEMT was not proposed until 1979 by Fujitsu engineer Takashi Mimura [86]. Mimura, inspired by a device patented by Dingle *et al.* at Bell Labs [87][86], eventually came up with his own patented device and demonstrated the first working HEMT in 1980.[88]

Physically, a HEMT consists of a of two semiconductors with differing bandgaps forming a junction as they are layered on top of each other (*heterojunction).* The most commonly-used materials for this junction are galium arsenide (GaAs) and aluminum galium arsenide (AlGaAs). This difference in bandgaps results in the deformation of the

band structure at the interface, which in the case of GaAs/AlGaAs takes the form of a potential well. If the AlGaAs is n-doped (i.e. has excess donor electrons), the electrons in the conduction band leak into this potential well. By applying a gate voltage, these electrons can become tightly confined in the $z-$direction, resulting in the formation of a 2-dimensional electron gas (2DEG). The electrons in the 2DEG have extremely high mobilities, resulting in high gain and speed with relatively low noise.

HEMT amplifiers outperform other field-effect transistors at microwave frequencies in terms of gain and switching speed. One of their earliest commercial uses was in radio astronomy [88], and this was later expanded to many other fields. Although useful in a wide variety of circumstances, the advent of highly specialized and sensitive quantum information experiments (e.g. [89]) imposes a new set of requirements on amplifiers. For one, in order to minimize the added noise photons of already small (i.e. few photon) microwave signals, the amplifier should be located at the same temperature stage as the measurement. In a dilution refrigerator, this corresponds to the 20 mK mixing chamber stage, where cooling power is extremely limited ($\lesssim 100\,\mu$W. A HEMT is unsuitable for this stage since they can dissipate milliwatts of power [2]. The noise temperature of a cryogenic HEMT (around 3 K), although very low, is still enough to disturb quantum measurements at millikelvin temperatures. While cryogenic HEMT amplifiers continue to be used in quantum information experiments at the 4 K stage, where the cooling power is much higher, it is clear that a new type of amplifier is needed for the lowest temperature stage. [2].

2.3.2 Parametric amplification

Though primarily used now for superconducting quantum computing applications, the concept of parametric amplification goes back to the 1960s [90], shortly after the Josephson effect was discovered. After appearing sporadically throughout the 1980s [91] and 1990s [92], interest stated to grow again as the result of the rapid development of quantum information science and the need for ultra-low noise measurement. A series of JPA experiments were demonstrated in the mid-2000s [93] [94] and have been used in a number of influential experiments, particularly those involving transmon qubits [95]. The principle of parametric amplification involves the periodic exchange of energy between two conjugate variables [2]. In the case of the JPA these are voltage and current, but can also be, for example, position and momentum. In fact, an oft-invoked classical example of parametric amplification involves a child sitting on a swing and generating momentum by periodically shifting their center of mass (i.e. pumping). This can analogously be done using an LC resonator and modulating the inductance via the Josephson effect.

An LC circuit has a natural frequency of $f_0 = 1/(2\pi\sqrt{L_0 C})$, where L_0 is the center frequency of the Josephson junction. If a signal frequency f_s is passed into the LC resonator which is then modulated at a frequency f_p, then the mixing operation $f_i = f_s \pm f_p$ occurs, producing two sidebands. In this case, when $f_p = 2f_0$, then the signal and lower sideband (called the *idler*), are equal and can be detected via homodyne detection with $f_{LO} = f_S$ [2].

Critically, JPAs do not dissipate heat in any of the elements due to the superconducting nature of the device, meaning that quantum-limited amplification can be achieved, and indeed this has been demonstrated in a number of experiments.

However, JPAs suffer from two main limitations. The first is that the LC-resonator basis of the device imposes a limitation on the gain-bandwidth product. This fundamental limitation can be overcome by moving the geometry from a standard LC-resonator to a traveling-wave geometry using a series of Josephson junctions. Such a device, coined a Josephson traveling wave parametric amplifier (JTWPA) was demonstrated with near-quantum limited noise by Macklin *et al.* [3]. This JTWPA was able to provide over 3 gigahertz of bandwidth while producing a noise temperature of 0.6 K, making it incredibly promising for future applications [3].

The second problem is that of the limited power handling. This is unfortunately more innate to the nonlinear nature of the Josephson junction [2], since it is primarily limited by the critical current. This value is typically no more than a few microamps, although it can be pushed to milliamps at the cost of requiring extra pumping power. The corresponding saturation power of a JPA is around -110 dBm, meaning that only a few qubit channels can be read out simultaneously [96]. This problem still extends to JTWPA, as the one measured by Macklin *et al.* is estimated to be able to read out a maximum only 20 qubits [3]. JPAs, while being incredibly impactful in the field of superconducting quantum computing, are fickle devices that require constant tuning [2]. As quantum computing becomes more sophisticated and commercialized, more reliable devices with better saturation powers may be needed in order to read out the growing number of qubits simultaneously.

2.3.3 Spin maser

Although recent research on solid-state spin masers has focused on room temperature-operation, solid-state spins could also be an attractive choice for low-temperature quantum technology applications. The noise temperature of such an amplifier is, hypothetically, limited only by the operation temperature of the spins [66]. A spin maser could also potentially have a much larger saturation power than is possible for a JPA, due to the large number of spins present. Typical spin maser amplifiers investigated in Refs. [65][64] begin to saturate at output powers between -30 and -50 dBm. Operation in a dilution refrigerator at millikelvin temperatures also serves to overcome the main drawback of a spin maser, and the advantages are such that a spin maser could directly compete with JPAs in situations where the readout of many qubits is necessary. In Chs. 5 and 6 we will develop a spin-maser that can operate as a low-noise amplifier in a millikelvin environment.

2.4 Summary

We have investigated the history, significance, and applications of various maser schemes, as well as a few key parameters that are of significance to a practical amplifier. Since masers have the potential to be particularly useful within the context of quantum technology, in the next section we derive a link between classical spin physics and cavity quantum dynamics (CQED). I will introduce some of the core concepts of CQED and calculate some of the key parameters of the cavity spin maser within these confines.

Chapter 3

Coupling spins in diamond to a resonant cavity

3.1 Theory of a resonant cavity

3.1.1 The quantum LC circuit resonator

We begin with a simple circuit studied in almost every introductory physics class, the LC circuit. The circuit is so named because of its two components - a capacitor C and an inductor L, as seen in Fig. 3.1.

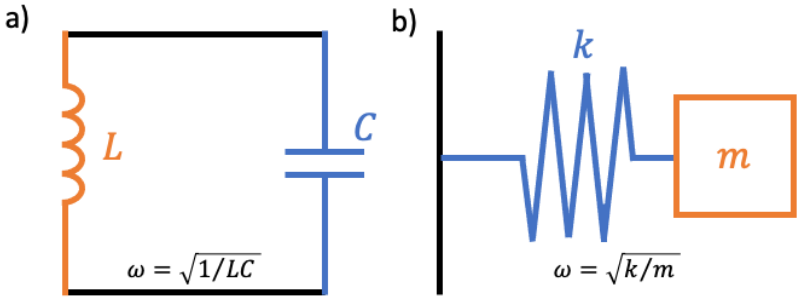

Figure 3.1: Common simple harmonic oscillator models. a) The LC simple harmonic oscillator. b) the equivalent mechanical simple harmonic oscillator

If the capacitor is charged prior to being connected to the inductor, then current will begin to flow as a result of the charged plates equilibriating. However, due to the response of the inductor to current flow through it, the charge will undergo simple harmonic oscillation between plates with a frequency given by

$$\omega = \sqrt{\frac{L}{C}}. \tag{3.1}$$

Since the circuit lacks any dissipative element, the sum of the energy stored in the

capacitor and inductor is always conserved, or

$$E_{tot} = \frac{1}{2}\frac{Q(t)^2}{C} + \frac{1}{2}LI(t)^2 = \text{constant}. \tag{3.2}$$

Note that the current $I(t)$ is equal to the time derivative of the charge $dQ(t)/dt$, which itself is proportional to the flux through the inductor $\Phi(t)$,

$$I(t) = \frac{dQ}{dt} = \frac{\Phi(t)}{L}. \tag{3.3}$$

Thus we can then express Eq. 3.2 in terms of the variables $Q(t)$ and $\Phi(t)$,

$$E_{tot} = \frac{Q(t)^2}{2C} + \frac{\Phi(t)^2}{2L}. \tag{3.4}$$

The motivation for representing the variables this way is that Φ and Q represent a pair of *conjugate variables*, or variables that are Fourier transforms of each other. This is analogous to the position and momentum of a mechanical simple harmonic oscillator, seen in Fig. 3.1b. We now move to the quantum mechanical picture, where these conjugate variables are defined as observables whose operators do not commute,

$$[\hat{A}, \hat{B}] = \hat{A}\hat{B} - \hat{B}\hat{A} = i\hbar. \tag{3.5}$$

Returning to the LC resonator, we now make the following substitutions of classical observables with their quantum operators:

$$\begin{aligned} Q &\rightarrow \hat{q} \\ \Phi &\rightarrow \hat{\phi}, \end{aligned} \tag{3.6}$$

which yields a Hamiltonian

$$\hat{H} = \frac{\hat{q}^2}{2C} + \frac{\hat{\phi}^2}{2L}. \tag{3.7}$$

This Hamiltonian is exactly analogous to the commonly-studied quantum harmonic oscillator. The solution consists of a series of Fock states, represented in bra-ket notation by $|n\rangle = |0\rangle$, $|1\rangle$, $|2\rangle$,... which satisfy the condition

$$\hat{H}\,|n\rangle = \hbar\omega_0\left(\hat{a}^\dagger\hat{a} + 1/2\right), \tag{3.8}$$

where ω_0 is defined as in Eq. 3.1. The operators $\hat{a}^\dagger$ and $\hat{a}$ are the state raising and lowering operators (also known as "ladder operators"), respectively, given by

$$\begin{aligned} \hat{a} &= \frac{1}{\sqrt{2\hbar Z_0}}\left(\hat{\phi} + iZ_0\hat{q}\right) \\ \hat{a}^\dagger &= \frac{1}{\sqrt{2\hbar Z_0}}\left(\hat{\phi} - iZ_0\hat{q}\right), \end{aligned} \tag{3.9}$$

where $Z_0 = \sqrt{L/C}$ is the LC circuit impedance. The ladder operators are called so because they have the following effects on a given Fock state:

$$\begin{aligned} \hat{a}\,|n\rangle &= \sqrt{n}\,|n-1\rangle \\ \hat{a}^\dagger\,|n\rangle &= \sqrt{n+1}\,|n+1\rangle\,. \end{aligned} \tag{3.10}$$

Thus the corresponding energy of the nth state is

$$E_n = \hbar\omega_0\,(n+1/2)\,. \tag{3.11}$$

We can then express the physical observables of the system in terms of the ladder operators

$$\begin{aligned} \hat{V} = \frac{\hat{q}}{C} &= i\omega_0\sqrt{\frac{\hbar Z_0}{2}}\left(\hat{a}-\hat{a}^\dagger\right) \\ \hat{I} = \frac{\hat{\phi}}{L} &= \omega_0\sqrt{\frac{\hbar}{2Z_0}}\left(\hat{a}+\hat{a}^\dagger\right). \end{aligned} \tag{3.12}$$

An interesting result of Eq. 3.11 is that even in the $n = 0$ state there is a nonzero energy $E_0 = \hbar\omega/2$, known as the zero-point energy. This energy is the source of the *quantum noise* seen in Chapter 2. This zero-point energy also has associated voltage and current fluctuations which can be calculated by the variance of Eqs. 3.12,

$$\begin{aligned} \langle \delta I^2 \rangle &= \langle 0|\hat{I}^2|0\rangle = \frac{\hbar w_0^2}{2Z_0} \\ \langle \delta V^2 \rangle &= \langle 0|\hat{V}^2|0\rangle = \frac{\hbar Z_0 w_0^2}{2}. \end{aligned} \tag{3.13}$$

These fluctuations produce small electromagnetic fields known as the *vacuum field*, usually written as δE and δB. Later, in Section 3.3, we will use this vacuum magnetic field to calculate the coupling between the spin ensemble and the loop-gap resonator.

3.1.2 The lumped element resonator

We can now move on to modeling a more realistic system. The first thing we can do is to add a resistance R in parallel to L and C to represent the losses of the resonant cavity. This is seen in Fig. 3.2a. Secondly, the cavity can be capacitively coupled to and input and output transmission line, each of which has a capacitance C_κ. Each line also has a resistance R_L Such a system can be represented by the Norton equivalent in Fig. 3.2b, with the definitions [97]

$$R' = \frac{1 + {w_0}^2 C_\kappa^2 R_L^2}{{w_0}^2 C_\kappa^2 R_L} \tag{3.14}$$

$$C' = \frac{C_\kappa}{1 + {w_0}^2 C_\kappa^2 R_L^2}. \tag{3.15}$$

Since the elements are now all in parallel, the total resistance can be written as

$$\frac{1}{R_{tot}} = \frac{1}{R} + \frac{2}{R'}, \tag{3.16}$$

and total capacitance as

$$C_{tot} = C + 2C'. \tag{3.17}$$

This also has the effect of shifting the cavity resonance to the new value

$$\omega_0' = \frac{1}{\sqrt{L(C+2C')}}. \tag{3.18}$$

In order to simplify these expressions, we will assume that the coupling capacitors are small relative to the capacitance of the resonator, $C_\kappa \ll C$. This implies that $w_0 C_\kappa R_L \ll 1$ and thus $C' \approx C_\kappa$. The total capacitance of the system is then assumed to be approximately equal to C. We now introduce the concept of the *quality factor* Q, defined as the ratio of the energy stored in a resonator to the energy lost per cycle. For a damped LRC oscillator, $Q = \omega CR$. The above approximation makes calculation of our current system's quality factor relatively straightforward [97],

$$\begin{aligned} Q_L &= \omega_0' C_{tot} R_{tot} \\ Q_L &= \omega_0' \frac{C+2C'}{1/R + 2/R'} \\ &\approx \omega_0 \frac{C}{1/R + 2/R'}. \end{aligned} \tag{3.19}$$

We can define this quantity as the total quality factor and separate out the contributions from the resonator (Q_{int}) and the coupling lines (Q_{ext}), such that

$$\begin{aligned} Q_{tot}^{-1} &= \frac{1}{\omega_0 CR} + \frac{2}{\omega_0 CR'} \\ &= Q_{int}^{-1} + Q_{ext,1}^{-1} + Q_{ext,2}^{-1}. \end{aligned} \tag{3.20}$$

An alternative definition of Q is the ratio of the central frequency to the resonator linewidth ($Q = \frac{\omega_0}{\kappa}$. This allows us to define the linewidths (i.e. loss rates) due to the cavity and coupling lines as

$$\begin{aligned} \kappa_{int} &= \frac{\omega_0}{Q_{int}}, \\ \kappa_1 &= \frac{\omega_0}{Q_{ext,1}}, \\ \kappa_2 &= \frac{\omega_0}{Q_{ext,2}}. \end{aligned} \tag{3.21}$$

Note that the final two quantities are usually referred to, including in this work, by their combined rate $\kappa_{ext} = \kappa_1 + \kappa_2$. These rates will be used in the definition of the S-matrix in the next section.

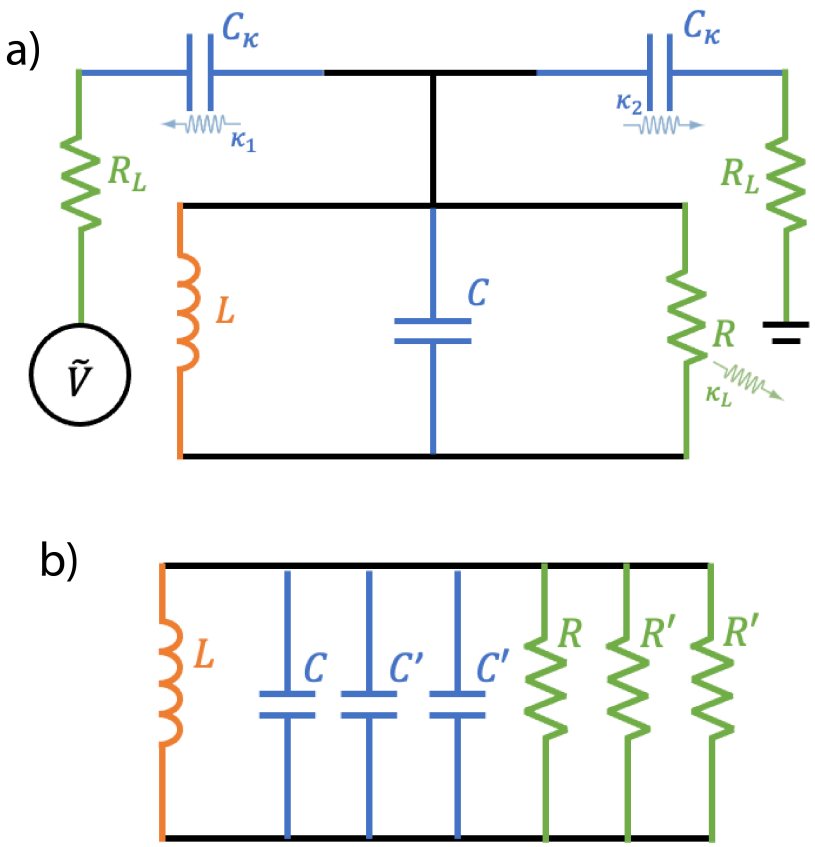

Figure 3.2: The realistic model of a resonant cavity. a) The lumped element equivalent of a lossy resonant cavity coupled to transmission lines. b) the Norton equivalent circuit.

3.1.3 Input-output theory and the S-matrix

Now that we have constructed our open quantum system, we can calculate the change of the intra-resonator field operator $\hat{a}$ (Eq. 3.9). In the Heisenberg picture, the evolution of the operator as a function of time can be found by invoking the Lindblad master equation [98],

$$\partial_t\left(\hat{a}(t)\right) = \frac{\left[\hat{a}, \hat{H}\right]}{i\hbar} - \frac{1}{2}\left(\kappa_1 + \kappa_2 + \kappa_{int}\right)\hat{a}(t) + \sqrt{\kappa_1}\hat{a}_{in,1}, \tag{3.22}$$

which for $\hat{a}(t)$, which has time-dependence of the form $a_0 e^{-i\omega t}$,

$$\partial_t\left(\hat{a}(t)\right) = -i\omega_0\hat{a}(t) - \frac{1}{2}\left(\kappa_1 + \kappa_2 + \kappa_{int}\right)\hat{a}(t) + \sqrt{\kappa_1}\hat{a}_{in,1}. \tag{3.23}$$

Where the first term represents the oscillation of the cavity field within the resonator, the second term the losses of the field to the internal resistance and ports 1 and 2, and the third term the input driving field. We represent the coherent driving field applied to port 1 by the expression $\hat{a}_{in}(t) = \alpha_{in,1}e^{-i\omega t}$, normalized such that the input power $P = \hbar\omega|\alpha_{in,1}|^2$, where $|\alpha_{in,1}|^2$ is the mean number of photons entering port 1 per second.

This input field obeys the conservation equations

$$\begin{aligned} \hat{a}_{in,1}(t) + \hat{a}_{out,1}(t) &= \sqrt{\kappa_1}\hat{a}(t), \\ \hat{a}_{in,1}(t) + \hat{a}_{out,2}(t) &= \sqrt{\kappa_2}\hat{a}(t). \end{aligned} \tag{3.24}$$

We can replace the $\hat{a}(t)$ operators in Eq. 3.23 with their expectation (classical) values

$$\langle \hat{a}(t) \rangle = \alpha(t), \tag{3.25}$$

which gives us the expression

$$\partial_t \left(\alpha(t)\right) = -i\omega_0\alpha(t) - \frac{1}{2}\left(\kappa_1 + \kappa_2 + \kappa_{int}\right)\alpha(t) + \sqrt{\kappa_1}\alpha_{in,1}(t). \tag{3.26}$$

In order to express these quantities in terms of frequency dependence, we perform a Fourier transform on $\alpha(t)$, resulting in the expression for the cavity field

$$\alpha(\omega) = \frac{2\sqrt{\kappa_1}}{\kappa_1 + \kappa_2 + \kappa_{int} - 2i(\omega - \omega_0)}\alpha_{in,1}(\omega). \tag{3.27}$$

From this we can calculate the number of photons in the cavity at a given time when driven by an microwave signal of frequency ω and power P_{in}, given by

$$\bar{n} = |\alpha(\omega)|^2 = \frac{4\kappa_1 P_{in}}{\hbar\omega[(\kappa_1 + \kappa_2 + \kappa_{int})^2 + 4(\omega - \omega_0)^2]}. \tag{3.28}$$

Finally, we can derive the scattering matrix, or S-matrix, which gives the complex ratio of the outgoing signal to the input. Although in our case it is assumed that port 1 provides the input signal, this formula can be written in the more general form of

$$S_{ij} = \frac{a_{out,i}}{a_{in,j}}. \tag{3.29}$$

Where ports 1 and 2 are represented in Fig. 3.3. Combining Eqs. 3.24 and 3.27, the expressions for reflection (S_{11}) and transmission (S_{12}) can be calculated. The behavior of these ratios is highly influenced by the relative strengths of the internal (κ_{int}) and external ($\kappa_1 + \kappa_2 = \kappa_{int}$) damping rates. There are three different regimes based on the ratio of these values, as discussed in the respective sections below.

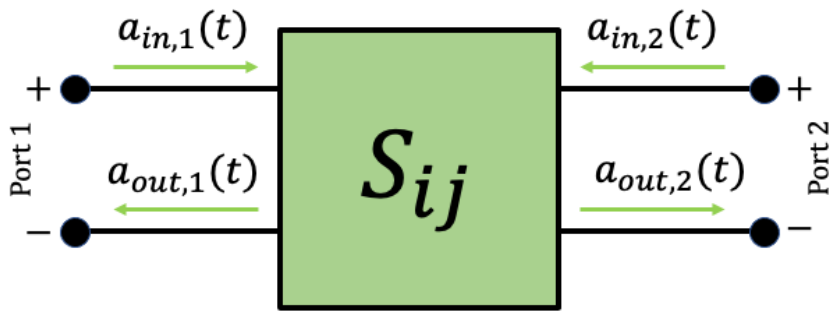

Figure 3.3: The S-matrix in terms of input and output fields.

Reflection measurement

The reflection coefficient is given by $S_{11} = \frac{a_{out,1}}{a_{in,1}}$, which equates to

$$S_{11} = \frac{2\kappa_{ext}}{\kappa_{ext} + \kappa_{int} - 2i(\omega - \omega_0)} - 1. \tag{3.30}$$

In the reflection measurements described in Chs. 4 and 5, we terminate and pull up the antenna pin on port 2 on the resonator enclosure and exclusively use port 1 for measurement, hence in Eq. 3.30 $\kappa_2 \approx 0$ in and κ_1 is replaced with κ_{ext}. The three regimes, pictured in Fig. 3.4, can thus be described as follows:

- The undercoupled regime, where $\kappa_{ext} < \kappa_{int}$ ($Q_{ext} > Q_{int}$). Near resonance the reflection is characterized by a broad dip in amplitude. The width of this amplitude dip is primarily determined by κ_{int}.
- The critically coupled regime, where $\kappa_{ext} = \kappa_{int}$ ($Q_{ext} = Q_{int}$). The reflected signal amplitude goes to zero on resonance.
- The overcoupled regime, where $\kappa_{ext} > \kappa_{int}$ ($Q_{ext} < Q_{int}$). For all frequencies the reflected amplitude $S_{11} \approx 1$, whereas the phase shifts by 360°.

Transmission measurement

Likewise, the transmission coefficient, $S_{21} = \frac{a_{out,2}}{a_{in,1}}$, is equivalent to

$$S_{21} = \frac{\kappa_{ext}}{\kappa_{ext} + \kappa_{int} - 2i(\omega - \omega_0)}. \tag{3.31}$$

In our transmission measurements described in subsequent chapters, we choose a configuration where $\kappa_1 = \kappa_2 = \kappa_{ext}/2$. This has been incorporated into Eq. 3.31. Similar to the reflection case, we can characterize the three different regimes:

- The undercoupled regime, where $\kappa_{ext} < \kappa_{int}$. The transmission amplitude through the cavity is scaled to the ratio of κ_{ext} and κ_{int} ($\approx \kappa_{ext}/\kappa_{int}$) and the width of the transmission peak is primarily determined by κ_{int}.
- The critically coupled regime, where $\kappa_{ext} = \kappa_{int}$. The transmitted signal reaches 1/2 at resonance and both κ_{ext} and κ_{int} contribute to the width of the transmission peak.
- The overcoupled regime, where $\kappa_{ext} > \kappa_{int}$. At resonance, the magnitude of the transmitted signal approaches 1 and the width is primarily controlled by κ_{ext}.

These regimes are plotted for transmission and reflection in Fig. 3.4.

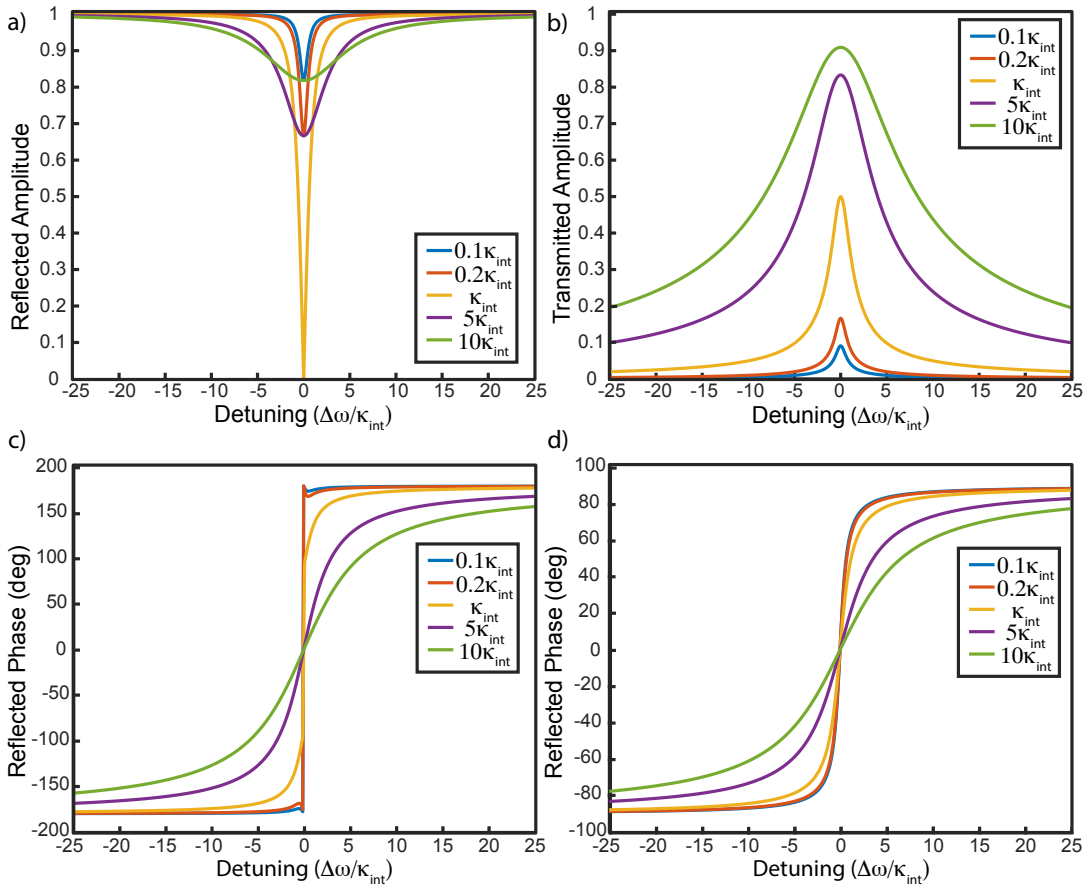

Figure 3.4: Transmission and reflection spectra for a hypothetical microwave resonator with internal quality factor $Q_{int} = \omega_0/\kappa_{int} = 600$. a) The reflection power amplitude for the case of $\kappa_2 = 0$ with varying values of κ_1 relative to k_{int}. b) The transmission power amplitude for the case of $\kappa_1 = \kappa_2 = \kappa_{ext}/2$, for varying values of κ_{ext}. c) Corresponding phase of the reflected signal under the same conditions. d) Corresponding phase of the transmitted signal.

3.2 Electron Spin Resonance

For a two-level, spin-1/2 system, applying a static magnetic field splits the degeneracy of the spin alignments (the Zeeman effect), with one alignment being lower energy than the other depending on the g-factor of the system. Adding a second, oscillating perpendicular B-field can drive the spins between these states, if the field has the same frequency as the corresponding frequency splitting between the spin levels. The process of using this effect for the characterization and manipulation of spins is known as electron spin resonance (ESR), alternatively electron paramagnetic resonance (EPR). ESR is a powerful technique that is used for many applications in a variety of different fields [99]. Although it is a well-developed theory with a plethora of available references, for instance Ref. [99] [100], I will briefly cover some of the basic concepts relevant to our experiments.

3.2.1 The Bloch Equations

An ensemble of N paramagnetic spins each have individual magnetic moments of $\vec{\mu_i}$, represented quantum mechanically by the operator $\hat{\mu} = g_s \frac{e}{2m} \hat{S}$, where g_s is the Lande's g-factor of the system (≈ 2 for a free electron), and e and m are the charge and mass, in this case of the electron. The quantity $\hat{S}$ is the spin angular momentum operator, assuming a spin-1/2 system. The spin operators $\hat{S} = \left\langle \hat{S}_x, \hat{S}_y, \hat{S}_z \right\rangle$ are operators on the spin states $|s, m_s\rangle$ with eigenvalues defined by s, the total spin quantum number, and m_s, the projection of the spin vector in the z-direction:

$$\begin{aligned} \hat{S}^2 |s, m_s\rangle &= s(s+1) |s, m_s\rangle , \\ \hat{S}_z |s, m_s\rangle &= m_s |s, m_s\rangle . \end{aligned} \tag{3.32}$$

The operators $\hat{S}_x, \hat{S}_y, \hat{S}_z$ satisfy the commutation relations $[\hat{S}_i, \hat{S}_j] = i\hbar\epsilon_{ijk}\hat{S}_k$, where ϵ_{ijk} is the Levi-Cevita symbol. This relationship will be helpful later. For now, we return to the definition of the magnetic moment operator, where we can lump the constant quantities together as

$$\gamma_e = g_s \frac{e}{2m}. \tag{3.33}$$

Defining γ_e as the free electron *gyromagnetic ratio*, which has a value of $|\gamma_e| = 28$ MHz/mT when converted into units appropriate the scale of our experiments. When placed in a B-field $B(t)$, the spin magnetic moment of the electron will couple to the magnetic field. The energy associated with the interaction between the field and the electron can be found through the system Hamiltonian

$$\hat{H} = -\hat{\mu} \cdot \vec{B}(t) = -\gamma \hat{S} \cdot \vec{B}(t). \tag{3.34}$$

Thus the time evolution of the magnetic moment under the applied B-field can be found through the Ehrenfest theorem,

$$\frac{d\left\langle \hat{S} \right\rangle}{dt} = \frac{i}{h} \left\langle \left[-\gamma \hat{S} \cdot \vec{B}(t), \hat{S} \right] \right\rangle . \tag{3.35}$$

Substituting in the spin operators introduced above, this makes the evaluation of the above equation straightforward,

$$\frac{d\left\langle \hat{S} \right\rangle}{dt} = -\gamma \left\langle \hat{S} \times \vec{B}(t) \right\rangle = -\gamma \left\langle \hat{S} \right\rangle \times \vec{B}(t). \tag{3.36}$$

Rewriting in terms of $\vec{\mu_i}$, which is the classical expectation value $\langle \hat{\mu} \rangle$ for the ith spin is

$$\frac{d\vec{\mu_i}}{dt} = -\gamma \vec{\mu_i} \times \vec{B}(t). \tag{3.37}$$

The net macroscopic magnetization of the spin ensemble can be written as $M = \sum_i \mu_i$, so that the time-evolution of M can be found by summing equation 3.37 over i,

$$\frac{d\vec{M}}{dt} = -\gamma \vec{M} \times \vec{B}(t). \tag{3.38}$$

In an ESR experiment, the direction of the static magnetic field is usually defined to be along z, meaning that the spins are polarized in the z-direction, given by $\vec{B}(t) = B_0\hat{z}$. In this case the components of the magnetization have the behavior

$$\begin{aligned} \dot{M}_x &= -\omega_0 M_y, \\ \dot{M}_y &= \omega_0 M_x, \\ \dot{M}_z &= 0. \end{aligned} \tag{3.39}$$

Where $\omega_0 = \gamma_e B_0$ is called the *Larmor frequency*. The magnetization vector $\vec{M}$ will precess about $\hat{z}$ at the Larmor frequency, while conserving its magnitude.

A useful model of visualizing the time evolution of spins was developed by Richard Feynman and is called the Bloch sphere [101]. Since the magnitude is conserved, the magnetization of the spins can always be represented by a point on the surface of the sphere. Fig. 3.5 details how to represent the direction of an arbitrary magnetization vector as defined by the two angles θ and ϕ.

The magnetization of the spins precesses about z when any static field is applied, and since this is a requirement for spin resonance experiments it is usually more convenient to transform into a rotating coordinate system of frequency ω, represented by

$$\vec{M} = M'_x\hat{x}' + M'_y\hat{y}' + M'_z\hat{z}'. \tag{3.40}$$

In order to drive the spins around the surface of the Bloch sphere, an oscillating magnetic field is applied in the $x-y$ plane. For the sake of convenience, we define the oscillating field to be applied along the x-direction with magnitude $B_1(t) = 2B_1\cos\omega t\hat{x}$. Note that we chose the frequency of the rotating frame to be the same as that of B_1. The oscillating field can then be decomposed into counter-rotating terms of frequencies ω and $-\omega$ with amplitudes equal to B_1. When transformed into a rotating frame, one of these terms will have zero frequency (i.e. a static field) and the other will have frequency 2ω, which can be ignored when the rotating wave approximation (RWA) is applied. The RWA allows us to ignore rapidly-oscillating terms in the Hamiltonian, and this approximation is valid under the condition $B_1 \ll B_0$ (i.e. B_1 is a perturbation of B_0). In this case, the time evolution of the magnetization must account for the rotating frame, such that

$$\frac{d\vec{M}'}{dt} = \frac{d\vec{M}}{dt} - \vec{M}\times\vec{\omega}. \tag{3.41}$$

Equating this with Eq. 3.38 we can obtain the following expression for the time evolution of the magnetization in the rotating frame, which is

$$\frac{d\vec{M}'}{dt} = -\gamma_e\vec{M}'\times\vec{B}_{eff}, \tag{3.42}$$

where $\vec{B}_{eff}$ represents the effective field experienced in the rotating frame, which can be represented as

$$B_{eff}(t) = \begin{pmatrix} B_1 \\ 0 \\ B_0 - \frac{\omega}{\gamma}. \end{pmatrix}. \tag{3.43}$$

This produces the equations for the components

$$\begin{aligned}\dot{M}'_x &= \Delta_0 M'_y \\ \dot{M}'_y &= -\Delta_0 M'_x - \omega_1 M'_z \\ \dot{M}'_z &= \omega_1 M'_y,\end{aligned} \tag{3.44}$$

where we have defined $\Delta_0 = \omega - \omega_0$ and $\omega_1 = \gamma_e B_1$. Similar to the case of a static field applied along $\hat{z}$, the oscillating field drives the net magnetization vector of the spins about x, with a frequency of ω_1 as seen in Fig. 3.5. The angle θ that the net magnetization makes with the z-axis is given by $\theta = \omega_1/\Delta_0$ and the rotation frequency $\Omega_R = \sqrt{\Delta_0^2 + \omega_1^2}$ is called the *Rabi frequency*.

Control of the duration and phase of a pulse of frequency ω and amplitude can drive the spins to any arbitrary angle θ and ϕ about any transverse axis. Pulses which rotate θ by $\pi/2$ or π are called $\pi/2$- and π-pulses, respectively, and the time required for such a pulse can easily be calculated by

$$\begin{aligned}t_{\pi/2} &= \frac{\pi}{2\omega_1} = \frac{\pi}{2\gamma_e B_1}, \\ t_\pi &= 2t_{\pi/2},\end{aligned} \tag{3.45}$$

whereas ϕ can be manipulated by setting the phase of the applied microwave pulse. A pulse with phase ϕ represented by $B_1(t) = 2B_1 \cos(\omega t + \phi)\hat{x}$, when transformed into a rotating frame at frequency ω, becomes $B'_1(t) = B_1 \cos(\phi)\hat{x}' + B_1 \sin(\phi)\hat{y}'$. This allows one to choose any rotation axis lying in the $x - y$ plane. This is an essential technique of pulse ESR, a field which has a similarly well developed theory [102], and was first proposed and developed by the Bloch [103, 104] and later Purcell [105] groups in the early 1950s.

As depicted in Fig. 3.5, the Bloch sphere can also be used to represent magnetization in the quantum regime, or more generally the state of a qubit. In this case the net magnetization of the ensemble can be replaced with the spin (or qubit) quantum states $|\downarrow\rangle$ and $|\uparrow\rangle$,

$$|\psi\rangle = \cos(\theta/2)\,|\uparrow\rangle + \sin(\theta/2)e^{-i\phi}\,|\downarrow\rangle\,. \tag{3.46}$$

The angle θ, known as the azimuthal angle, represents the weight of the superposition between the two states. For example, an azimuthal angle of 0 corresponds to the eigenstate $|\uparrow\rangle$, and an angle of $\pi/2$ corresponds to an equal superposition of states $|\downarrow\rangle$ and $|\uparrow\rangle$. The angle ϕ is known as the *phase angle*. We will use this picture when deriving results in later sections.

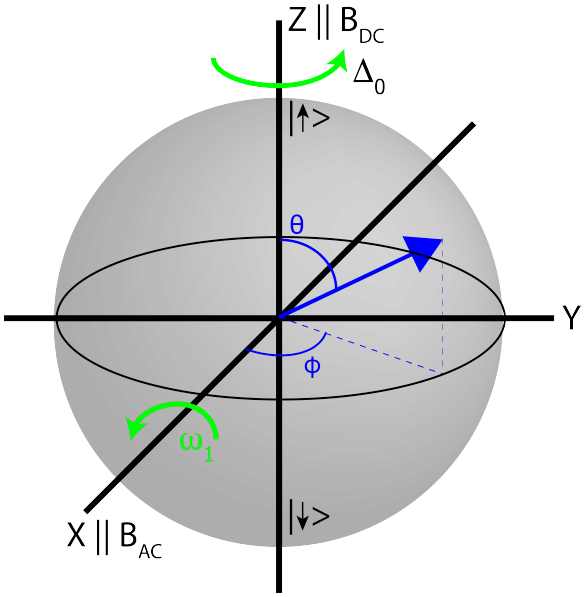

Figure 3.5: Representation of the Bloch sphere for a two-level quantum system. $|\downarrow\rangle$ and $|\uparrow\rangle$ represent the direction of the magnetization in the classical regime, or the spin state in the quantum regime. The static B-field applied along the $\hat{z}$ direction causes the system to precess at frequency ω_0, which when transforming into a rotating frame ω results in a frequency of rotation $\Delta_0 = \omega - \omega_0$ (green arrow). An oscillating field applied along $\hat{x}$ causes the magnetization vector to rotate about that axis (green arrow, ω_1). The state of the spin, as represented by the vector in blue, can be defined anywhere on the Bloch surface by two angles, θ and ϕ.

3.2.2 Relaxation and Decoherence

The magnetization of the spins is described by the vector sum of the three component vectors - one parallel to the direction of the applied static field (z-direction) and two in the perpendicular ($x-y$) plane. The parallel and perpendicular components are known as the longitudinal and transverse magnetization, respectively. In the absence of a driving pulse, the $z-$component of $\vec{M}$ will decay back to the thermal equilibrium state, $\vec{M}_{eq} = M_{eq}\hat{z}$. As given above, the total magnetization is $N\mu$ where N is the total number of spins. Due to thermal energy fluctuations at a given temperature T, the fraction of spins occupying the ground state is given by the Curie law,

$$M_{eq} = N\mu \tanh\left(\frac{\hbar\omega_0}{k_B T}\right), \tag{3.47}$$

which means that at low enough temperatures or high enough field nearly all the spins are aligned parallel to z, as is the case at 10 mK in our experiments. The process of returning to the thermal equilibrium state is known as *spin lattice relaxation* and is characterized by a time constant T_1. In most cases, spin relaxation is caused by interaction with the lattice vibrations (phonons), which is highly dependent on the temperature. Typical T_1 times at millikelvin temperatures can reach hours for NV centers but are reduced to $<$ 10ms at room temperature [20].

Meanwhile, the $x-$ and $y-$ components of $\vec{M}$ vanish in a process called spin decoherence. The processes that govern spin decoherence are complex and the time scale, represented by T_2, is usually much shorter than that of T_1. For example T_2 of NV center ensembles has been measured to be of order $\sim 10\,\mu$s at room temperature [20][106][107]. The relaxation of $\vec{M}$ can be incorporated into Eqs. 3.44,

$$\begin{aligned}
\dot{M}'_x &= \Delta_0 M'_y - \frac{M'_x}{T_2} \\
\dot{M}'_y &= -\Delta_0 M'_x - \omega_1 M'_z - \frac{M'_y}{T_2} \\
\dot{M}'_z &= \omega_1 M'_y - \frac{M'_z - M_{eq}}{T_1}.
\end{aligned} \tag{3.48}$$

From these coupled differential equations, the steady-state solution of these so-called *Bloch equations* can be found, and are

$$\begin{aligned}
M'_x, s &= \frac{T_2^2 \Delta_0 \omega_1}{1 + (T_2\Delta_0)^2 + T_1 T_2 \omega_1^2} M_{eq} \\
M'_y, s &= \frac{T_2 \omega_1}{1 + (T_2\Delta_0)^2 + T_1 T_2 \omega_1^2} M_{eq} \\
M'_z, s &= \frac{1 + T_2^2 \Delta_0^2}{1 + (T_2\Delta_0)^2 + T_1 T_2 \omega_1^2} M_{eq}.
\end{aligned} \tag{3.49}$$

As the drive power ω_1 is increased, the spins oscillate faster between states. When this oscillation (i.e. Rabi frequency) becomes much faster than the relaxation timescales, $\omega_1^2 \gg 1/T_1 T_2$, the net magnetization begins to approach zero. This is known as *saturation*, and in this state there are no more available spins to absorb microwave photons.

In quantum information science (QIS) experiments, T_1 essentially functions as the maximum possible timescale - once excited, any measurements or manipulations of the spins must be completed before the magnetization again reaches its thermal equilibrium state. In truth, though, QIS experiments are often governed by the decoherence time T_2, as it governs the qubit phase coherence. Thus, the ability to measure the quantity T_2 of a given qubit system accurately is critical. It is also desirable for one to try to extend this time as far as possible. However, an ensemble of spins contains a range of resonance frequencies due to local magnetic field inhomogeneity. The spin distribution is typically modeled as a Lorentzian function, with the spins centered around a central frequency ω_s as depicted in Fig. 3.6 below. The general form of a Lorentzian is characterized by its full-width at half-maximum (FWHM), which we represent by the symbol Γ.

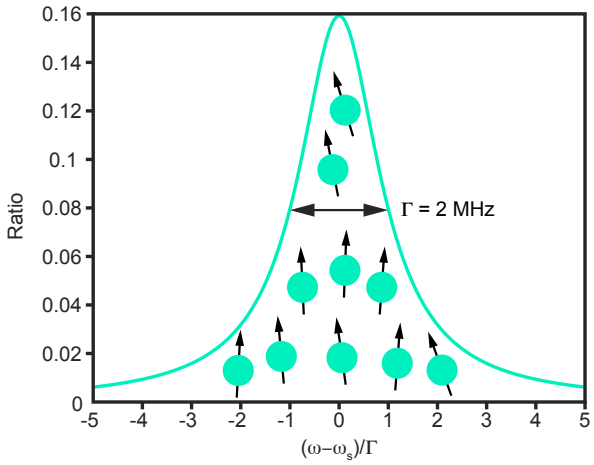

Figure 3.6: Simulated Lorentzian distribution of an ensemble of spins with a full-width half-maximum (FWHM) of 2 MHz.

This broadening of the resonance signal from effects such as inhomogeneity and spin diffusion leads to quicker decay of the transverse magnetization as given by the formula

$$\frac{1}{T_2^*} = \frac{1}{T_2} + \Delta\omega_{inhom}, \tag{3.50}$$

where $\Delta\omega_{inhom}$ is the range of the inhomogeneous broadening, which for a Lorentzian distribution is directly related to Γ, and T_2^* is the free induction decay time. For any amount of broadening, T_2^* will always be smaller than T_2.

3.2.3 Hahn Echo technique

A method for measuring T_2 was developed [108] and refined [105][109] into what is now known as the Hahn-echo or spin-echo technique. The technique compensates for the effects of static inhomogeneous broadening by using a π-pulse to rotate the spin magnetization by 180° about the y-axis, as seen in Fig. 3.7. By performing this rotation, the spins will eventually "rephase", meaning that the magnetization vectors realign and emit microwave photons, known as an "echo" signal. Varying the time τ before the π-pulse allows for the measurement of T_2.

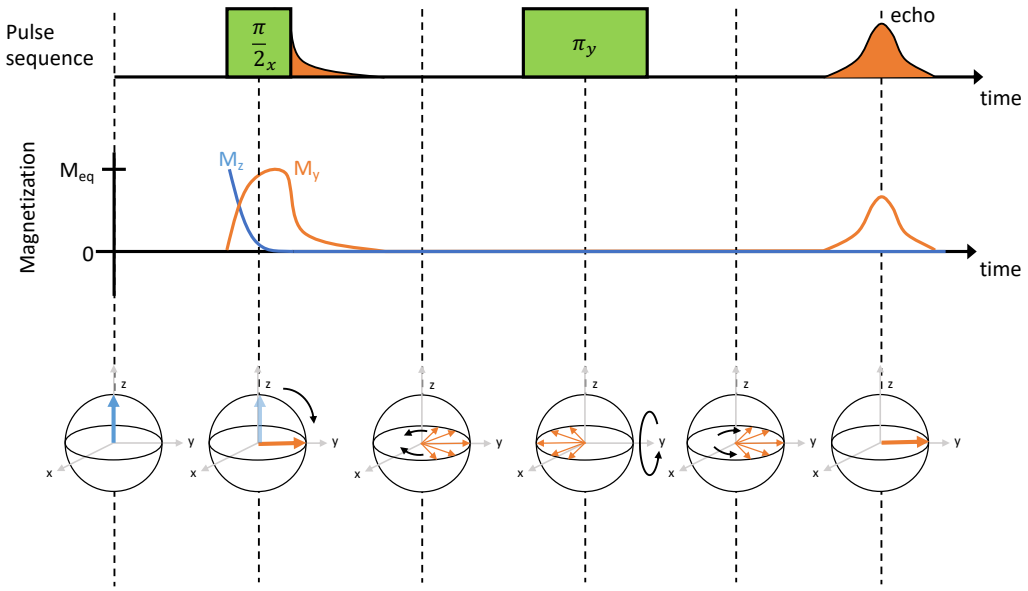

Figure 3.7: Standard Hahn echo pulse sequence. The sequence starts with a $\pi/2$ pulse to rotate the spin magnetization about x. Once the pulse ends, the spins begin to dephase due to local field inhomogeneities on a time scale T_2^*. This can be pictured as many spin vectors "spreading out" as they precess about $\hat{z}$ at different rates. This results in an apparent decay of M_y. After a time $t > T_2^*$, the spins are flipped by a π pulse about y. When the spins refocus, the magnetization along $\hat{y}$ is restored and an echo is emitted. [32].

3.3 Paramagnetic Spins in a Cavity

ESR experiments often make use of a resonant cavity to enhance the signal [110, 111]. When microwave photons are injected into a cavity, the photons circulate back and forth for a number of times corresponding to the cavity's quality factor Q, as defined in the previous section. The higher the quality factor, the more likely the photons are to interact with the spins under study. The study of this interaction between the photons in the cavity and the anharmonic quantum system is known as cavity quantum electrodynamics (CQED). CQED concepts play a central role in many QIS applications, so a brief summary of important topics will be discussed in the following sections.

3.3.1 System Hamiltonian

We will begin by deriving some of the key results of CQED. Beginning with a system consisting of a single electron of spin 1/2 (or other two-level system) contained within a cavity, the cavity EM mode is modeled as a quantum harmonic oscillator [112]. We can write the total system Hamiltonian as

$$\hat{H} = \hat{H}_{spin} + \hat{H}_{cavity} + \hat{H}_{int}. \tag{3.51}$$

Recalling Sec. 3.2.1, the Hamiltonian for a spin in a static magnetic field aligned along the lab frame $z-$axis is

$$H_{spin} = -\vec{\mu} \cdot \vec{B} = |\gamma_e| \vec{B} \cdot \vec{S}.$$

Here we introduce the Pauli matrices for a spin-1/2 system

$$\sigma_x = \begin{pmatrix} 0 & 1 \\ 1 & 0 \end{pmatrix}, \sigma_y = \begin{pmatrix} 0 & -i \\ i & 0 \end{pmatrix}, \sigma_z = \begin{pmatrix} 1 & 0 \\ 0 & -1 \end{pmatrix}, \tag{3.52}$$

which are related to the operators $\vec{S}$ by

$$S_i = \frac{\hbar}{2} \sigma_i. \tag{3.53}$$

Thus we can rewrite the spin Hamiltonian as:

$$H_{spin}/\hbar = \frac{1}{2} \omega_s \sigma_z. \tag{3.54}$$

For the resonator, the result was derived in the previous section and is

$$H_{cavity}/\hbar = \omega_c a^\dagger a, \tag{3.55}$$

where we have dropped the 1/2 since it is a constant energy offset. In these equations, ω_s and ω_r are the resonant frequencies of the spin and cavity, respectively, and $a^\dagger$ and a are the creation and annihilation operators on the cavity photon number $|n\rangle$, $|n+1\rangle$, etc. Similar to the electron and the B-field, the interaction between the cavity and the spin is governed by the strength of the electron's magnetic dipole moment and the magnetic vacuum (zero point) fluctuation of the resonator, and can be written in the Schrödinger (non-time dependent) picture as [32, 113]

$$H_{int}/\hbar = |\gamma_e| \vec{B}_1 \cdot \vec{S}. \tag{3.56}$$

In this case, the oscillating field $\vec{B}_1$ takes the quantized form $\delta\vec{B}_1(\hat{a}+\hat{a}^\dagger)$, as it is determined by the number of microwave photons present in the resonator (see Section 3.1.1 for details on deriving the current quanta). Thus the interaction term can be written

$$\begin{aligned} H_{int}/\hbar &= |\gamma_e| \delta B \sigma_x (a^\dagger + a) \\ &= g(\sigma_+ a^\dagger + \sigma_+ a + \sigma_- a^\dagger + \sigma_- a), \end{aligned} \tag{3.57}$$

where we have introduced the operators σ_+ and σ_- as the raising and lowering operators of the spin state, which transfer the system between excited and ground states $|e\rangle$ and $|g\rangle$. These operators are related to σ_x and σ_y by

$$\begin{aligned} \sigma_x &= \frac{1}{2}(\sigma_+ + \sigma_-), \\ \sigma_y &= \frac{1}{2i}(\sigma_+ - \sigma_-). \end{aligned} \tag{3.58}$$

We have also defined the coupling constant g as:

$$g = \langle 1|\hat{H}_{int}|0\rangle\,, \tag{3.59}$$

which for a oscillating B-field that is uniform in space can be simplified to

$$\begin{aligned} g &= \frac{|\gamma_e|\delta B}{2} \qquad \text{for spin-1/2} \\ &= \frac{|\gamma_e|\delta B}{\sqrt{2}} \qquad \text{for spin-1.} \end{aligned} \tag{3.60}$$

Note the factor $\sqrt{2}$ difference of the spin matrices for spin-1/2 and spin-1 systems that is reflected in the coupling constants above. Since our diamonds contain impurity centers with both $S = 1/2$ and $S = 1$, we will have to use both of these formulas when calculating the coupling constants.

In order to approximate the single-spin coupling in our system, we can assume that the vacuum field $\delta\vec{B}$ is roughly constant throughout the sample space. As will be explored later in Chapter 4, this is a reasonable approximation for a loop-gap resonator. For a resonator of ω_r in the quantum ground state ($n = 0$), the vacuum field has an energy of $\hbar\omega_r/2$, which is split between the electric and magnetic fields. The total magnetic field energy is given by

$$\frac{1}{2}\frac{\hbar\omega_r}{2} = \frac{1}{2\mu_0}\int_c^{\mathcal{V}} |\delta\vec{B}(\vec{r})|^2 dV. \tag{3.61}$$

Rearranging to solve for δB, we get

$$\delta B = \sqrt{\frac{\hbar\omega_r\mu_0}{2\mathcal{V}}}. \tag{3.62}$$

Where $\mathcal{V}_c$ is the total mode volume of the resonator. In our loop-gap resonator (see Ch. 4), the center mode has $\mathcal{V}_c = 11.5\text{mm}^3$ and $\omega_r = 6\,\text{GHz}$. Using Eqs. 3.62 and 3.60, this results in $\delta B = 16\text{pT}$ and $g = 0.23\text{Hz}$, 0.33Hz for spin-1/2 and spin-1 centers, respectively. We note that these coupling constants are both far less than the typical loss rates ($\sim 1 - 5$ MHz) and cavity resonance (~ 6 GHz), which allows us to approximate solution to the system Hamiltonian, as descibed below.

3.3.2 Jaynes-Cummings Hamiltonian

To simplify the Hamiltonian of Eq. 3.57, we can again invoke the rotating wave approximation to neglect the non-resonant terms proportional to $\sigma_+ a^\dagger$ and $\sigma_- a$. These terms represent non-energy conserving processes that oscillate quickly compared to the energy conserving processes $\sigma_+ a$ and $\sigma_- a^\dagger$. Since the individual coupling to the spin is much smaller than the resonant frequency and loss rates ($g \ll \kappa, \omega_r$), the quickly rotating terms can safely be dropped. This results in the well-known Jaynes-Cummings Hamiltonian [114],

$$\begin{aligned} \hat{H}_{JC} &= \hat{H}_{spin} + \hat{H}_{cavity} + \hat{H}_{int}, \\ H_{JC}/\hbar &= \frac{1}{2}\omega_s\sigma_z + \omega_c a^\dagger a + g(\sigma_+ a + \sigma_- a^\dagger), \end{aligned} \tag{3.63}$$

where $g = \gamma_e \delta B / 2\hbar$ is the coupling between the spin and the cavity. This Hamiltonian can be solved exactly with the following dressed states [112]:

$$|+, n\rangle = \cos(\theta_n/2)\,|e, n\rangle + i \sin(\theta_n/2)\,|g, n+1\rangle\,, \tag{3.64}$$

$$|-, n\rangle = \sin(\theta_n/2)\,|e, n\rangle - i \cos(\theta_n/2)\,|g, n+1\rangle\,, \tag{3.65}$$

where $\theta_n = \tan^{-1} \frac{\Omega_n}{\Delta_s}$ is called the mixing angle, $\Delta_s = \omega_s - \omega_r$ is the detuning between the spins and the cavity, and Ω_n is the n-photon quantum Rabi frequency given by:

$$\Omega_n = 2g\sqrt{n+1} \tag{3.66}$$

The corresponding eigenenergies to these dressed states are given by

$$E_{n,\pm} = (n + 1/2)\hbar\omega_r \pm \frac{\hbar}{2}\sqrt{\Delta_s^2 + \Omega_n^2} \tag{3.67}$$

In the quantum ground state ($n = 0$), then the Rabi frequency is related to the coupling by $\Omega_0 = 2g$. There are two regimes of Δ_s of interest, to be discussed below, illustrated in Fig. 3.8:

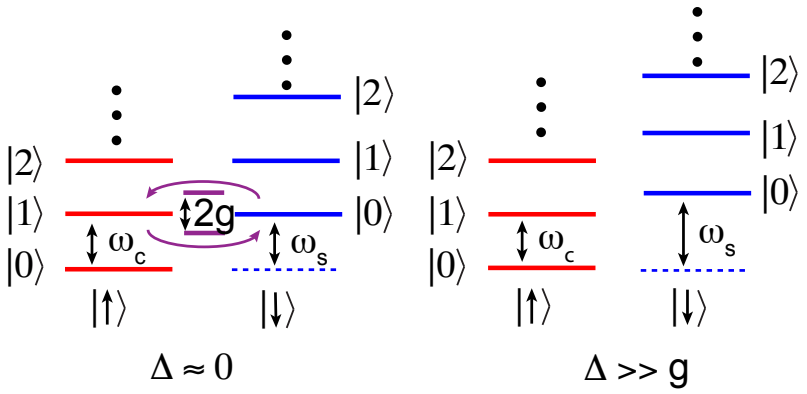

Figure 3.8: Coupling between a single spin and a resonant cavity. The cavity is modeled as a quantum harmonic oscillator with levels $|0\rangle$, $|1\rangle$, $|2\rangle$ ... separated by frequency ω_r, whereas the spin is a two level system with resonant frequency ω_s. The state of the spin affects the total energy of the system, represented by a shift in the cavity energy levels (shown in blue). When the spin is near-resonant with the cavity, a coupling with strength g is established between the states $|1, \downarrow\rangle$ and $|0, \uparrow\rangle$. When the spin is far detuned from the cavity, no energy is exchanged between the systems.

1. **The resonant regime**. When $\Delta_s \approx 0$, the mixing angle approaches $\pi/2$ and the dressed states are analogous to a classical pair of coupled oscillators [112]. The cavity and spins exchange energy reversibly at frequency Ω_n. When this rate of energy exchange is higher than any other loss or decay rates (such as cavity losses, spontaneous emission, or for a spin ensemble, inhomogeneous broadening), the cavity-spin system is said to be in the strong-coupling regime, manifested by two split peaks in the frequency spectrum. In the strong coupling regime quantum information can be coherently exchanged (swapped) between the two coupled systems before it decays, making the achievement of strong coupling necessary for many QIS experiments.

2. **The dispersive regime**. When $\Delta_s \gg g$, the mixing angle θ_n approaches zero. The eigenstate equations are thus reduced to the separate states $|e, n\rangle$ and $|g, n+1\rangle$ with only a tiny admixture between them. As a result, no energy is exchanged between the systems. However, both systems experience a small shift in their resonance frequencies depending on the state of the other.

3.3.3 Spin ensembles and the Tavis-Cummings Hamiltonian

In order to see new behavior that appears with ensembles of spins, we now turn to a situation where there is an ensemble of N identical spins instead of just one. The Hamiltonian of the system, known as the Tavis-Cummings Hamiltonian, can be written as follows [115]:

$$\hat{H}_{TC}/\hbar = \frac{1}{2}\omega_s \sum_i^N \hat{\sigma}_z^{(i)} + \omega_r \hat{a}^\dagger \hat{a} + g \sum_i^N (\hat{\sigma}_+^{(i)} \hat{a} + \hat{\sigma}_-^{(i)} \hat{a}^\dagger) \tag{3.68}$$

In this expression, we sum each spin operator i over the entire ensemble. In keeping with the previous section, we assume that the coupling constant is uniform over the sample. In reality this is not quite the case, but this will be discussed later. The total spin operators can be written as a sum of the individual operators over all N spins, given by

$$\hat{\mathcal{S}}_{x,y,z} = \sum_i^N \hat{\sigma}_{x,y,z}^{(i)}, \tag{3.69}$$

$$\hat{\mathcal{S}}_+ = \sum_i^N \hat{\sigma}_+^{(i)}, \tag{3.70}$$

$$\hat{\mathcal{S}}_- = \sum_i^N \hat{\sigma}_-^{(i)}. \tag{3.71}$$

Replacing the terms in Eq. 3.68 with their summations, we get the Hamiltonian

$$\hat{H}_{TC}/\hbar = \frac{1}{2}\omega_s \hat{\mathcal{S}}_z + \omega_c \hat{a}^\dagger \hat{a} + g(\hat{\mathcal{S}}_+ \hat{a} + \hat{\mathcal{S}}_- \hat{a}^\dagger). \tag{3.72}$$

In this case, we note that the total spin operator $\hat{\mathcal{S}}^2$, as well as $\hat{\mathcal{S}}_z$, commute with $\hat{H}_{TC}$ and thus their eigenvalues represent good quantum numbers. We establish the following basis for quantifying the collective system:

$$\begin{aligned} \hat{\mathcal{S}}^2 |\mathcal{S}, M\rangle &= \mathcal{S}(\mathcal{S}+1) |\mathcal{S}, M\rangle , \\ \hat{\mathcal{S}}_z |\mathcal{S}, M\rangle &= M |\mathcal{S}, M\rangle . \end{aligned} \tag{3.73}$$

The value M, representing the total z-spin of the system, can take any integer value from $-\mathcal{S}$ to $\mathcal{S}$ (i.e. $-N/2$ to $N/2$). The value $\mathcal{S}$ is known as the cooperation number and its value describes the state of the ensemble. For example, a state of only two spins will have $\mathcal{S} = 0, 1$, corresponding to the singlet state and triplet state, respectively [116]. For

large N, the number of possible values for the state $|\mathcal{S}, M\rangle$ ($\mathcal{O}(N^2)$)is much smaller than the total number of spin states, (2^N). Therefore, for a given cooperation state $\mathcal{S}$ there are a high number of degenerate states with the same value of M. This can be seen in Fig. 3.9. The exception is the highest $\mathcal{S}$ state, $\mathcal{S} = N/2$, for which there is one single ground state given by $M = -N/2$. This state can be written as a product of the individual spin states as

$$|G\rangle = |N/2, -N/2\rangle = |g_1, g_2, ..., g_N\rangle \,. \tag{3.74}$$

If we were to apply the raising operator $\mathcal{S}_+$ to the ground state, we preserve the cooperation number $N/2$ and obtain an expression for the collective first excited state

$$|E\rangle = |N/2, -N/2+1\rangle = \frac{1}{\sqrt{N}}(|e_1, g_2, ..., g_N\rangle + |g_1, e_2, ..., g_N\rangle + ... + |g_1, g_2, ..., e_N\rangle). \tag{3.75}$$

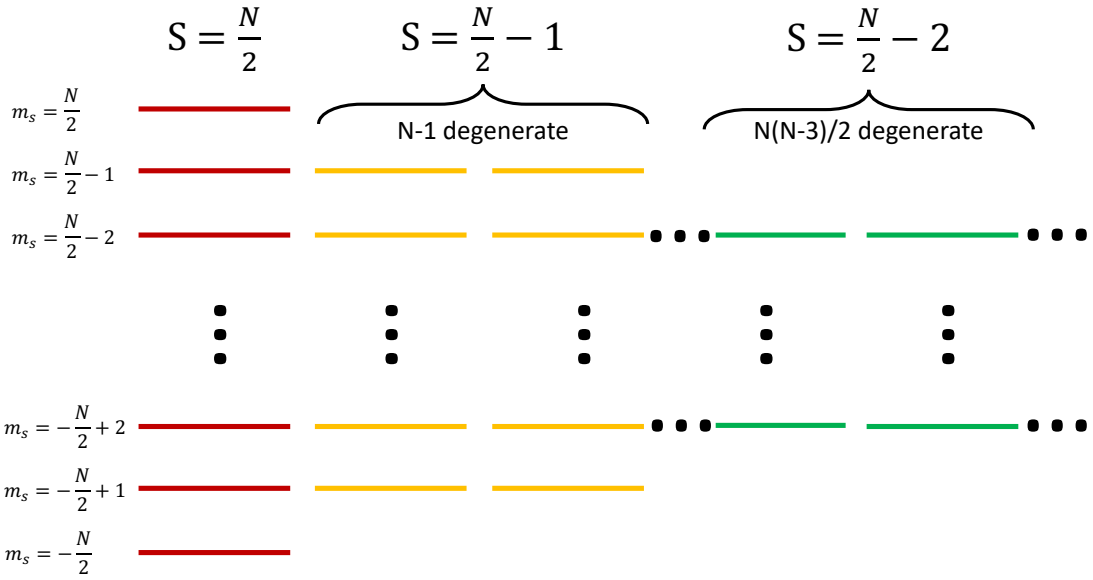

Figure 3.9: Energy level diagram of an ensemble of NV centers. The ground state is given by the eigenvalues $|N/2, -N/2\rangle$, which is nondegenerate. There are N different ways to add a single excitation to the system, with 1 state given by $|N/2, -N/2+1\rangle$ and $N-1$ states with $|N/2-1, -N/2+1\rangle$. Lower values of $\mathcal{S}$ have higher degeneracy.

We then see that a single excitation is spread throughout all N spins, requiring a factor of $\frac{1}{\sqrt{N}}$ for normalization. If a single microwave photon exists in the cavity ($|1\rangle$), then by Eq. 3.72 the combined cavity-spin state $|G, 1\rangle$ and $|E, 0\rangle$ are coupled as

$$\langle E, 0| \hat{H}_{TC} |G, 1\rangle = g\sqrt{N}. \tag{3.76}$$

The collective coupling between the cavity and N spins is equal to the single-spin coupling enhanced by a factor of $\sqrt{N}$, assuming that each spin coupling g_i is identical.

However, we can show that even if an inhomogeneity in the coupling constant for each spin is introduced, the result does not change [117][118].

Let us now envision our system under typical experimental conditions. As we have noted, when the condition $k_B T \ll \hbar\omega_s$ is met, then the collective spin system almost entirely occupies the ground state $|N/2, -N/2\rangle$. This is the case for spins with resonant frequency 6 GHz at 10 mK. We also assume that the number of excitations $\bar{n}$ is much less than the number of spins, also met in our experiments since $N \sim 10^{14}$ and $\bar{n} \lesssim 10^5$.

With this in mind, a useful mathematical trick is to envision the N spins as a single oscillator whose transitions are described with the bosonic ladder operators $b^\dagger$ and b, which replace the Paui spin operators. Each "step" corresponds to flipping a single spin and moving the total spin between minimum and maximum values $-N/2$ and $N/2$. Mapping the Pauli spin operators to bosonic operators, we can rewrite them as follows [118]:

$$\begin{aligned} \hat{\sigma}_z^i &\equiv -\frac{1}{2} + \hat{b_i}^\dagger \hat{b_i}, \\ \hat{\sigma}_-^i &\equiv \hat{b_i}\sqrt{1 - \hat{b_i}^\dagger \hat{b_i}}, \\ \hat{\sigma}_+^i &\equiv \hat{b_i}^\dagger \sqrt{1 - \hat{b_i}^\dagger \hat{b_i}}. \end{aligned} \tag{3.77}$$

These operators create and annihilate spin excitations, such that the sum $\sum_i^N \hat{b_i}^\dagger \hat{b_i}$ gives the total number of excitations in the system. The normalization term in $\sqrt{1 - \hat{b_i}^\dagger \hat{b_i}}$ ensure that each spin may only have one excitation, and thus preserve the two-state nature of the spins [116]. However, in the low-excitation limit, these operators can be simplified further by applying the Holstein-Primakoff approximation [119]. If we assume that the number of photons in the cavity $\bar{n}$ is much less than N, then the probability that two excitations act on a single spin is negligible and the square root terms in the above operators can be ignored. They can then be written as

$$\begin{aligned} \hat{\sigma}_-^i &\approx \hat{b_i}, \\ \hat{\sigma}_+^i &\approx \hat{b_i}^\dagger. \end{aligned} \tag{3.78}$$

Using the Holstein-Primakoff approximation and combining the bosonic operators with Eq. 3.68, the Hamiltonian obtained is

$$H_{TC-HP}/\hbar = \omega_c a^\dagger a + \frac{1}{2}\omega_s \sum_i^N b_i^\dagger b_i + \sum_i^N g_i (b_i^\dagger a + b_i a^\dagger). \tag{3.79}$$

Note that g has been swapped with g_i and placed inside the sum to represent the inhomogeneous coupling. Like above, we can define a collective bosonic operator, but one that also incorporates g_i such that

$$b^\dagger = \frac{1}{g_{ens}} \sum_i^N g_i b_i^\dagger, \tag{3.80}$$

where $g_{ens} = \sqrt{\sum_i^N g_i}$. This is the total ensemble coupling of the spins, and we see that if all $g_i = g$ then the sum reduces to the expression $g_{ens} = g\sqrt{N}$. Finally, putting this expression into the Tavis-Cummings Hamiltonian, we arrive at the final form that we will use in the next section to derive the coupled dynamics of the system,

$$\hat{H}_{TC}/\hbar = \omega_c a^\dagger a + \frac{1}{2}\omega_s \sum_i^N b_i^\dagger b_i + g_{ens}(b^\dagger a + b a^\dagger). \tag{3.81}$$

Compared with the Jaynes-Cummings Hamiltonian presented earlier, this Hamiltonian can be solved in exactly the same way, with the same form of the solution, as Eq. 3.63, the only change being that g is replaced with g_{ens}. The net result are the appearance of two polaritonic modes as the result of the coupling; their frequencies are given by

$$\omega_\pm = \omega_r \pm \frac{1}{2}\sqrt{4g_{ens}^2 + \Delta_s^2}, \tag{3.82}$$

where Δ_s is the detuning between the spins and cavity. As shown in Fig 3.10, these modes follow the behavior of ω_r and ω_s at large detunings, but near $\Delta_s = 0$ an avoided level crossing appears with a width given by $2g_{ens}$. The experimental observation of such behavior between our loop-gap microwave resonator and both NV and P1 centers in diamond is detailed in Chapter 4.

3.3.4 Coupling to an inhomogeneously broadened spin ensemble

One note must be made about the spin ensemble. In the case of a realistic sample, the resonant frequencies of N spins will not all be at exactly ω_s. Rather, due to local magnetic field inhomogeneities, a distribution of resonance frequencies (ω_i) spread around the central frequency ω_s, as discussed in Sec. 3.2.2 and shown in Fig. 3.6. When the distribution is modeled as a well-behaved function (i.e. Gaussian or Lorentzian), the effects of this broadening can be calculated directly [117, 120]. The key result is that the first collective excited state of the system $|E\rangle$, known as the *bright mode*, now couples to the $N-1$ *dark modes* of $\mathcal{S} = N/2 - 1$ as shown in Fig. 3.9. Energy is transferred to these modes at a rate of $T_2^* = 2/\Gamma$, where Γ is the characteristic width of the distribution function (the inhomogeneous broadening) of ω_i [32]. Although the broadening can be useful for certain applications, such as spin quantum memories [32][31] [121] [122], in other applications (such as a quantum emitter) it is desirable to keep the inhomogeneous broadening as low as possible.

3.3.5 Coopertivity and coupling regimes

We define the collective behavior of the system in a quantity known as the coopertivity, which depends on the relative values of g_{ens}, κ, and Γ. This dimensionless quantity is expressed as

$$C = \frac{2g_{ens}^2}{\kappa\Gamma}. \tag{3.83}$$

This leads to two broad categories of behavior:

- If $C \gg 1$, alternatively $g_{ens} \gg \kappa, \Gamma$, then the system is in the *strong coupling regime*, which manifests as an avoided crossing between the polaritonic modes as seen in Fig. 3.10. Qualitatively, a system in this regime is exchanging energy between the spins and cavity at a faster rate than the energy is being lost through either transfer to dark modes, or leakage out of the cavity. The ability to reach this regime is critical for efficient and coherent transfer of quantum information from a cavity to the spin ensemble, as in the case of quantum memory [122][121][31] or quantum transduction [13].

- If $\Gamma > g_{ens} > \kappa$ or $\Gamma > \kappa > g_{ens}$ (i.e. $C \gtrsim 1$), the system is described as being in the *high-coopertivity regime*. In this regime, avoided-crossing like behavior is seen near the $\Delta_s = 0$ point as a result of the spin-cavity coupling, but two distinct polaritonic modes cannot be resolved. There is also no coherent exchange of energy in this regime [123].

- If $C \ll 1$ or $g_{ens} \ll \kappa, \Gamma$, the system is in the *weak coupling regime*. In this case the cavity and spin system do not strongly interact; it is not possible to coherently transfer energy between the two systems. This regime is desirable for ESR measurements, where the spins are the key item of interest. The signal can still be enhanced by the presence of the resonator, but it does not distort the absorption spectrum of the spins.

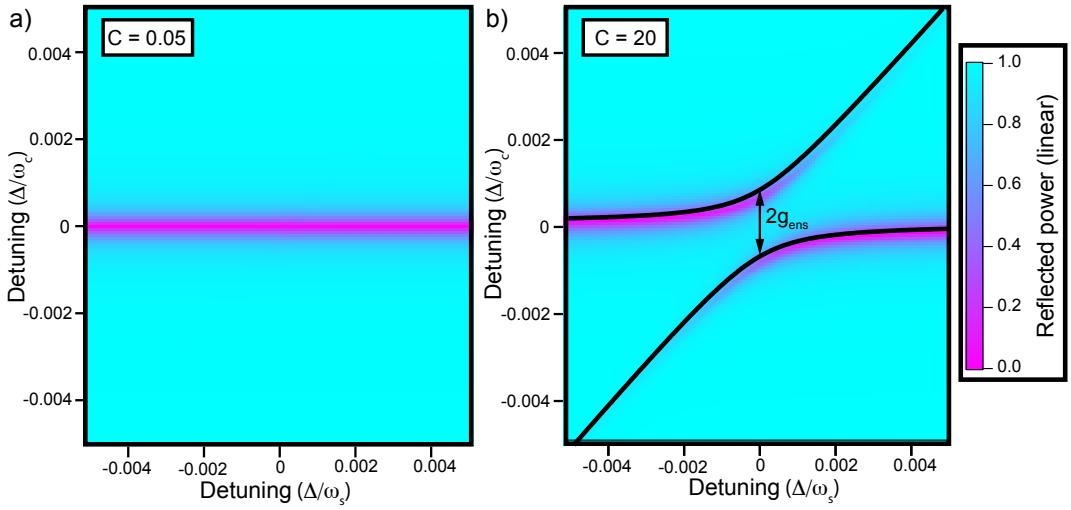

Figure 3.10: Weak versus strong coupling. Simulated reflection amplitude as a function of cavity probe detuning (y-axis) and spin detuning (x-axis). a) A coopertivity of C=0.05 means that the system is in the weak coupling regime. In this regime only the cavity resonance is visible and the spins do not exchange energy with the cavity. b) A coopertivity of C=20 puts the system in the strong coupling regime. The cavity and spin modes couple together into two hybridized polaritonic modes given by Eqs 3.82, with a clear avoided crossing between the modes.

3.3.6 Input-output theory of a cavity with spins

We will now establish the dynamics of the coupled spin-cavity system. We reintroduce the quantities $\kappa_1, \kappa_2, \kappa_{int}$ to represent the rates of the loss of energy through the input and output ports of the cavity as well as the internal losses of the resonator itself. We once again use Γ to represent the inhomogeneous broadening of the ensemble. The spontaneous emission rate of photons by the spins, represented by γ_{rad}, is low enough that it is ignored throughout this work. However, we will include it in the derivation below for the sake of completeness. In order to represent the probing of the spins with a low-power signal, we take the Holstein-Primakoff Hamiltonian obtained above and add a term to represent a coherent driving field at port 1, like the previous case of the bare resonator. We represent the probe signal by $\beta(t) = \beta_0 \exp^{-i\omega t}$, with β_0^2 representing the number of photons entering the cavity per second (i.e. input power). The Hamiltonian (see Eq. 3.68 for reference) is thus

$$\hat{H}/\hbar = \omega_c \hat{a}^\dagger \hat{a} + \frac{1}{2}\omega_s \sum_i^N \hat{b}_i^\dagger \hat{b}_i + g_{ens}(\hat{b}^\dagger \hat{a} + \hat{b}\hat{a}^\dagger) + i\sqrt{\kappa_1}\left(\beta \hat{a}^\dagger - \beta^* \hat{a}\right). \tag{3.84}$$

Following the procedure outlined in Ref. [32] and similar to the bare resonator case, the above Hamiltonian can be solved using the Lindblad master equation. The system of differential equations for the mean cavity- and spin-operator values are

$$\begin{aligned} \partial_t\left(\hat{a}(t)\right) &= -\left(i\omega_r + \frac{(\kappa_1 + \kappa_2 + \kappa_{int})}{2}\right)\hat{a}(t) - i\sum_i^N g_i \hat{b}_i + \sqrt{\kappa_1}\hat{a}_{in,1}, \\ \partial_t\left(\hat{b}_i(t)\right) &= -\left(\frac{\gamma_{rad}}{2} + i\omega_i\right)\hat{b}_i - i g_i \hat{a}. \end{aligned} \tag{3.85}$$

Like in the previous case, we replace the operators $\hat{a}$ and $\hat{b}_i$ with the mean-field values $\langle \hat{a} \rangle$ and $\left\langle \hat{b}_i \right\rangle$, with a steady-state ansatz of $\langle \hat{a} \rangle (t) = a_0 e^{-i\omega t}$ and $\left\langle \hat{b}_i \right\rangle (t) = b_{0,i} e^{-i\omega t}$. The differential equations above can then be solved as

$$\begin{aligned} b_{0,i} &= -\frac{i g_i}{\gamma/2 + i(\omega_j - \omega)} a_0, \\ a_0 &= \frac{i\sqrt{\kappa_1}}{\omega - \omega_r + i(\kappa_1 + \kappa_2 + \kappa_{ext})/2 - K(\omega)} a_{in}. \end{aligned} \tag{3.86}$$

Where we have kept the notation from Ref. [32] and introduced the function $K(\omega)$ that contains all of the information about the spin ensemble, written as

$$K(\omega) = \sum_i \frac{|g_i|^2}{\omega - \omega_i + i\frac{\gamma}{2}}. \tag{3.87}$$

This is the general, discrete form of $K(\omega)$, but a smooth function can also be obtained, assuming that the spins are distributed according to a well-behaved function. In this

work we will assume a Lorentzian distribution for the resonance frequencies of all spin ensembles. With this, the spin density function takes the form

$$\rho(\omega) = \frac{g_{ens}^2}{\pi} \frac{\Gamma}{(\omega - \omega_s)^2 + \Gamma^2}, \tag{3.88}$$

where Γ is the full-width half-max (FWHM) linewidth of the spin ensemble, which is also the characteristic linewidth of the ensemble that determines T_2^*. We also define $\omega_s = \int_{-\infty}^{\infty} \rho(\omega)\omega d\omega / g_{ens}^2$ to be the average spin frequency around which the distribution is centered. Note that, given our definition of the distribution in Eq. 3.88, integrating $\rho(\omega)$ over all frequencies returns g_{ens}^2. We can replace the discrete sum in the expression for $K(\omega)$ with the Lorentzian distribution function and one can show that

$$\begin{aligned} K(\omega) &= \int_{-\infty}^{\infty} \frac{\rho(\omega')d\omega'}{\omega - \omega' + i\gamma/2} \\ &= \frac{g_{ens}^2}{\omega - \omega_s + i\Gamma}. \end{aligned} \tag{3.89}$$

In the above equation we have ignored the spontaneous emission γ_{rad} since $\Gamma \gg \gamma_{rad}$. This finally allows us to determine the transmission spectrum in terms of the cavity spin ensemble,

$$t(\omega) = \frac{i\sqrt{\kappa_1 \kappa_2}}{\omega - \omega_r + i\frac{\kappa_1 + \kappa_2 + \kappa_{ext}}{2} - K(\omega)}, \tag{3.90}$$

and reflection spectrum

$$r(\omega) = \frac{i\kappa_1}{\omega - \omega_r + i\frac{\kappa_1 + \kappa_2 + \kappa_{ext}}{2} - K(\omega)} - 1. \tag{3.91}$$

Many of the experiments in Ch. 4 will measure the transmission through a cavity, so it is important to note that Eq. 3.90 cannot by itself distinguish between the loss rates κ_1 and κ_2. For this reason they will often be referred to as the combined loss rate $\kappa_{ext} = \kappa_1 + \kappa_2$. In the reflection spectrum measurements in Chs. 5 and 6, port 2 is terminated and heavily undercoupled so that $\kappa_2 \approx 0$ and thus $\kappa_{ext} = \kappa_1$. One final note on the expression $K(\omega)$ is that it can be generalized to other cases, including a bare cavity ($K(\omega) = 0$), which returns the same values for $t(\omega)$ and $r(\omega)$ as derived earlier. A $K(\omega)$ comprised of multiple superimposed Lorentzians can represent hyperfine splitting, such as in the case of ^{14}N nuclei in our spin ensemble. However, in order to resolve the different peaks it is required that the value of the hyperfine splitting is larger than the linewidth of the ensemble.

3.3.7 Spin susceptibility

An alternate way to derive equations 3.90 and 3.91 involves relating the function $K(\omega)$ to the magnetic spin susceptibility $\chi(\omega)$. We begin by deriving the real and imaginary

terms for the susceptibility for the spin ensemble. In SI units, the total B-field inside the spin sample is given by

$$\vec{B} = \mu_0 \left(\vec{H} + \vec{M} \right). \tag{3.92}$$

The definition of the spin susceptibility is the ratio of the magnetization $\vec{M}$ induced by the applied H-field $\vec{H}$, $M/H = \chi$, so that the expression for $\vec{B}$ becomes

$$\vec{B} = \mu_0 \left(1 + \chi\right) \vec{H}. \tag{3.93}$$

Following the usual notation for ESR calculations, for a given spin ensemble the oscillating microwave field is applied along the lab frame x-axis, $H_x(t) = 2H_1 \cos(\omega t)$. Earlier in section 3.2.1, we derived the behavior of $M'_x(t)$ and $M'_y(t)$, the magnetization vector in the rotating frame (Eqs. 3.49). We rewrite these equations here in slightly different form [124], given by

$$\begin{aligned} M'_x &= \chi_0 \omega_0 T_2 \frac{T_2 \Delta_0}{1 + (T_2 \Delta_0)^2} H_1, \\ M'_y &= \chi_0 \omega_0 T_2 \frac{1}{1 + (T_2 \Delta_0)^2} H_1. \end{aligned} \tag{3.94}$$

Compared to Eqs. 3.49, we assume a light driving power (i.e. $T_1 T_2 \omega_1^2 \ll 1$), which allows us to eliminate the term in the denominator. We have also replaced M_{eq} with $\chi_0 H_0$, the product of the static susceptibility and static H-field. Lastly, we have defined the quantities $\omega_1 = \mu_0 \gamma_e H_1$ and $\omega_0 = \mu_0 \gamma_e H_0$ and made the appropriate substitutions.

Transforming from the frame M'_x, M'_y, rotating at an arbitrary frequency ω, back into the lab frame M_x, we obtain the expression

$$M_x = M'_x \cos(\omega t) + M'_y \sin(\omega t). \tag{3.95}$$

Combining Eqs. 3.94 with the above, we get

$$M_x = 2H_1 \left(\chi'(\omega) \cos(\omega t) + \chi''(\omega) \sin(\omega t) \right), \tag{3.96}$$

where we have substituted the definitions

$$\chi'(\omega) \equiv \frac{\chi_0 \omega_0 T_2}{2} \frac{T_2 \Delta_0}{1 + (T_2 \Delta_0)^2}, \tag{3.97}$$

$$\chi''(\omega) \equiv \frac{\chi_0 \omega_0 T_2}{2} \frac{1}{1 + (T_2 \Delta_0)^2}. \tag{3.98}$$

For the sake of completeness, we allow the magnetization and applied H-field to be complex values $\tilde{M}_x$ and $\tilde{H}_x$, with M_x and $2H_1$ defined as the corresponding real parts. Then, we can define the complex susceptibility as $\chi(\omega) = \chi'(\omega) - i\chi''(\omega)$. This allows us to make the definition

$$\tilde{M}_x = \chi \tilde{H}_x. \tag{3.99}$$

Taking the real part of the left and right hand sides above, we return the relation 3.96.

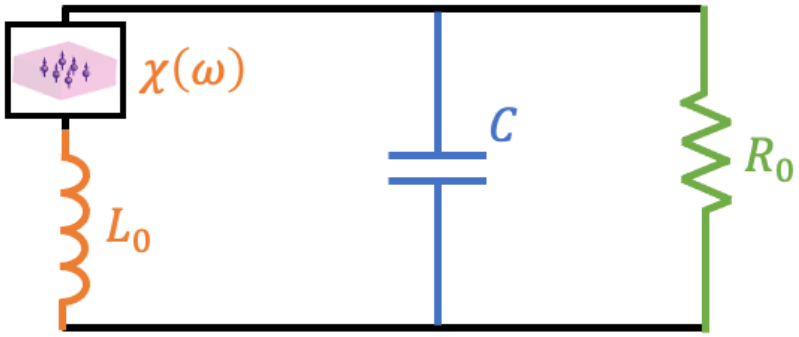

Figure 3.11: The lumped-element representation of the spin-cavity system, with a spin ensemble having susceptibility $\chi(\omega)$. The real and imaginary parts of the spin susceptibility will modify the total impedance of the system and contribute an additional loss term, respectively. This relationship allows the spin susceptibility to be determined via microwave transmission and reflection measurements.

If the resonator can be imagined as a lumped-element LRC circuit, then the spin system can be incorporated as a modification to the inductance L. An RLC circuit with the added spins can be seen in Fig. 3.11. A coil of inductance L_0 that is filled with a paramagnetic system has the total magnetic field inside the coil increased by the polarization of the spins, analogous to the enhancement of the electric field inside a capacitor by a dielectric material. The new inductance is given (in SI units) by $L(\omega) = L_0(1+\chi(\omega))$, which introduces a frequency dependence as well as an imaginary component. It is easy to see that $\mathrm{Re}\{\chi(\omega)\}$ modifies the resonator inductance, whereas $\mathrm{Im}\{\chi(\omega)\}$ adds another series resistance. The impedance of the capacitive component is unchanged. Calculating the inductor and resistor impedances of the circuit, we get

$$\begin{aligned} Z_L &= i\omega L_0 \left(1 + \chi'(\omega)\right), \\ Z_R &= R_0 + \omega L_0 \chi''(\omega). \end{aligned} \tag{3.100}$$

We must also introduce the so-called *filling factor*, η. In reality a paramagnetic sample will not fill the entirety of the inductive coil, so η compensates for this by reducing the magnetic susceptibility of the sample accordingly. For a coil inductor, as in Ref. [124], where the B-field is uniform over the volume of the coil, this ratio can be calculated by simply taking the ratio of the sample volume to the coil volume $\eta = V_s/V_c$. However, in cases where the AC field is not uniform over the sample or the LRC resonator, it is necessary to take an integral of the magnetic energy over the corresponding volume,

$$\eta = \frac{\int^{V_s} |\delta B(\vec{r})|^2 d\vec{r}}{\int^{V_c} |\delta B(\vec{r})|^2 d\vec{r}}. \tag{3.101}$$

Inserting the filling factor into the equation for Z_R, we then calculate the total resistance for $\omega \approx \omega_r$,

$$R_{tot} = R_0 + \omega_r \eta L_0 \chi''(\omega_r). \tag{3.102}$$

If we divide both sides by $\omega_r L_0$ and use the definition of the quality factor for a series, $Q = \omega L/R$, then we obtain an expression for the total Q of the system,

$$\frac{1}{Q_{tot}} = \frac{1}{Q_{int}} + \frac{1}{Q_{mag}}, \tag{3.103}$$

where we have defined

$$Q_{mag}^{-1} \equiv \frac{\kappa_{mag}}{\omega_r} = \eta\chi''(\omega_r). \tag{3.104}$$

From this expression follows the definition of the magnetic loss rate,

$$\kappa_{mag} = \eta\omega_r\chi''(\omega_r). \tag{3.105}$$

These equations define a quantity used in typical maser literature of the 1950s and 1960s (e.g. [66]), known as the *magnetic Q-factor*. This quantity represents the power absorbed, or in the case of a maser, emitted by the spins and is dependent only on the imaginary portion of the spin susceptibility and the filling factor. There is no reason that χ cannot be negative (as is the case in dimagnetic materials), and we can see clearly that the a positive (absorbing) susceptibility and a negative (emitting) susceptibility will result in different signs of Q_{mag}. Siegman, working primarily in a maser context, defines Q_{mag} so that it is negative when the spin is absorbing and positive when it is emitting, which I will continue to use in this work for the sake of continuity [66].

Returning to Eq. 3.100, we see that the inductance, and thus the resonance of the circuit is also shifted by the addition of the spins. This shift has magnitude

$$\omega_r' = \frac{1}{\sqrt{L'C}} = \frac{1}{\sqrt{L_0C(1+\eta\chi'(\omega_r))}}. \tag{3.106}$$

Assuming $\chi'(\omega_r) \ll 1$, as is the case for the vast majority of paramagnetic materials, this can be approximated as

$$\omega_r' \approx \omega_r\left(1 - \frac{\eta}{2}\chi'(\omega)\right). \tag{3.107}$$

In section 3.1.2 we derived the equation for transmission of a microwave signal through a bare cavity. Now taking the spins into account, we add the additional loss term κ_{mag} and replace ω_0 with the shifted resonance frequency ω_0', obtaining

$$S_{21} = \frac{i\sqrt{\kappa_1\kappa_2}}{\omega - \omega_0 + \frac{i}{2}(\kappa_1+\kappa_2+\kappa_{ext}) - \frac{1}{2}\omega_0\eta\chi'(\omega) + \frac{i}{2}\omega_0\eta\chi''(\omega)}. \tag{3.108}$$

Comparing the above with Eq. 3.90 derived earlier, we see that a relation between $K(\omega)$ and $\chi(\omega)$ can be established:

$$\chi(\omega) = -\frac{2}{\omega_0\eta}\overline{K}(\omega). \tag{3.109}$$

Assuming the spins and cavity are resonant ($\omega = \omega_s = \omega_r$), the value κ_{mag} can be derived in terms of the spin properties from the above equation and Eq. 3.105, which results in

$$\kappa_{mag}(\omega_s) = \frac{2g_{ens}^2}{\Gamma}. \tag{3.110}$$

Having established a link between quantum input-output theory and the classical spin picture, in the next section we examine the effect of inverting the spin ensemble.

3.4 The cavity maser

The equations derived in the previous section, while derived in the context of an absorbing cavity-spin system, can easily account for an inverted spin ensemble with minimal modification (i.e. a cavity maser). Here we derive some key parameters of a reflection cavity maser in a CQED context, using the quantities introduced in the previous section.

3.4.1 Population inversion

As noted in the previous section, the spin susceptibility of a system of paramagnetic spins may be negative. We describe the spins as being in a state of *population inversion*, meaning that for a 2-level system more spins inhabit the upper, excited levels than the lower (ground) state. Mathematically, the population difference $\Delta N = N_g - N_e$ between the lower and upper states becomes negative. In this work we will characterize the population inversion as the ratio between ΔN and the total number of spins N, or

$$p_{inv} = \frac{\Delta N}{N}. \tag{3.111}$$

A visual representation of an inverted and non-inverted spin transition, along with the corresponding values of p_{inv}, can be seen in Fig. 3.12.

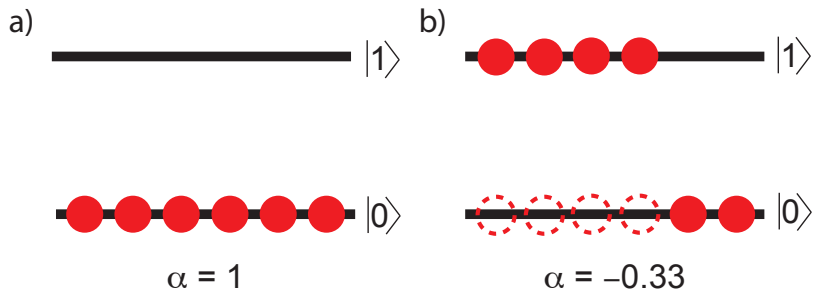

Figure 3.12: Inverted vs. non-inverted spin population. a) Spin transition at equilibrium, with all of the spins occupying the ground state. This is represented by a value of $p_{inv} = 1$. b) Partially inverted spin transition. Only $\frac{1}{3}$ of the spins are occupying the ground, corresponding to an inversion ratio of $p_{inv} = -0.33$.

Recalling the expression for $K(\omega)$ from the preceding section, we note that inverting the spin ensemble has the effect of changing the sign of $K(\omega)$, given that the term ΔN is contained within it. Thus, we can modify the formula for $K(\omega)$ slightly to take this into account. We assume that instead of the fully polarized state, the spin system is in a state with a population difference ΔN. The total coupling g_{ens} must be replaced with a (reduced) effective coupling representing the fact that fewer spins are available for

coupling to the cavity. $K(\omega)$ becomes

$$\begin{aligned} K(\omega) &= \frac{g_{ens,eff}^2}{\omega - \omega_s + i\Gamma} \\ &= \frac{g_{single}^2 \Delta N}{\omega - \omega_s + i\Gamma} \\ &= \frac{g_{single}^2 N p_{inv}}{\omega - \omega_s + i\Gamma} \\ &= \frac{p_{inv} g_{ens}^2}{\omega - \omega_s + i\Gamma}. \end{aligned} \tag{3.112}$$

A simple addition of the factor p_{inv} allows the function $K(\omega)$, and thus the expressions for $t(\omega)$ and $r(\omega)$, to be used in both cases where the spins inside the cavity are inverted or in their equilibrium state. Knowing the number of spins N and the full ensemble coupling g_{ens}, as well as the parameters of the cavity, allow the determination of the population inversion ratio from transmission or reflection data.

3.4.2 Gain-bandwidth product

When the spins inside the cavity are inverted, the system will emit microwave photons, amplifying the probe tone. If the degree of inversion is sufficiently high, the system will enter the free oscillating, or free-running maser, state. The degree of inversion is related to the magnetic quality factor introduced in Eq. 3.104 in the last section. When the system is amplifying,

$$Q_{mag} < 0, \quad \kappa_{mag} < 0. \tag{3.113}$$

With this, the total quality factor of the spin-resonator system can be written

$$Q_{tot}^{-1} = Q_{ext}^{-1} + Q_{ext}^{-1} + Q_{mag}^{-1}. \tag{3.114}$$

We will now derive the expression for the gain of the amplifier in terms of Q_{mag}. We recall the expression for reflected power from a spin-cavity ensemble that was derived in the previous section (Eq. 3.91). Assuming $\kappa_2 = 0$ and $\kappa_1 = \kappa_{ext}$,

$$r(\omega) = \frac{i\kappa_{ext}}{\omega - \omega_r + i\frac{\kappa_{ext}+\kappa_{int}}{2} - K(\omega)} - 1. \tag{3.115}$$

Now we redefine the function, substituting $K(\omega)$ for its definition in terms of spin susceptibility,

$$r(\omega) = \frac{i\kappa_{ext}}{\omega - \omega_r + \frac{i}{2}(\kappa_{ext} + \kappa_{int}) - \frac{1}{2}\omega_r \eta \chi'(\omega) + \frac{i}{2}\omega_r \eta \chi''(\omega)}. \tag{3.116}$$

Assuming we are working on resonance, $\omega = \omega_r + \frac{1}{2}\omega_r \eta \chi'(\omega)$, and using the definition of κ_{mag} established in the previous section, we obtain

$$r(\omega) = \frac{\kappa_{ext}}{\frac{1}{2}(\kappa_{ext} + \kappa_{int}) + \frac{1}{2}\omega_0 \eta \chi''(\omega)} - 1,$$

rewritten as

$$r(\omega) = \frac{2\kappa_{ext}}{\kappa_{ext} + \kappa_{int} + \kappa_{mag}} - 1.$$

Thus the ratio of reflected power to input power, i.e. the amplifier gain, is defined by the square of the above function,

$$G \equiv |r(\omega)|^2 = \left(\frac{\kappa_{int} + \kappa_{mag} - \kappa_{ext}}{\kappa_{int} + \kappa_{mag} + \kappa_{ext}} \right)^2. \tag{3.117}$$

The bandwidth of the amplifier is simply the sum of all the linewidths,

$$B = \omega_0 Q_{tot}^{-1} = \kappa_{ext} + \kappa_{int} - |\kappa_{mag}|. \tag{3.118}$$

We see then that if the linewidth of the cavity is very large relative to the other values of κ (i.e. the under-coupled regime), then no gain occurs. However, for a case where the linewidth is sufficiently small (i.e. the critical- or over-coupled regime), gain can occur under certain conditions of κ_{mag}. For a low-bandwidth cavity, κ_{int} can be ignored relative to the other two linewidths, and Eqs. 3.117 and 3.118 simplify to

$$G = \left(\frac{\kappa_{ext} + |\kappa_{mag}|}{\kappa_{ext} - |\kappa_{mag}|} \right)^2, \tag{3.119}$$

and

$$B = \kappa_{ext} - |\kappa_{mag}|. \tag{3.120}$$

Thus we define the gain-bandwidth product as

$$B\sqrt{G} = \kappa_{ext} + |\kappa_{mag}|. \tag{3.121}$$

We see that for the overcoupled case, the maximum gain-bandwidth product occurs when $\kappa_{ext} = |\kappa_{mag}|$, resulting in

$$B\sqrt{G} = 2\kappa_{ext}. \tag{3.122}$$

In the case of this work, we typically operate in the critically or near-critically coupled regime $\kappa_{int} \approx \kappa_{ext}$. In this case we can re-derive the results above in an identical manner, and obtain

$$B\sqrt{G} = |\kappa_{mag}|. \tag{3.123}$$

For a critically-coupled system, the gain-bandwidth product is dependent only on the properties of the spin system and the collective coupling to the cavity.

3.4.3 The maser threshold and the self-oscillating regime

Spontaneous emission

In his 1917 paper on quantum radiation, Einstein related the probabilities of spontaneous and stimulated emission to the frequency mode density. These values, represented by

coefficients A and B respectively, obey the relation [54]

$$\begin{aligned} \frac{A}{B} &= \frac{\hbar\omega^2}{\pi^2 c^3} d\omega, \\ \frac{A}{B} &= \frac{\hbar\omega^3}{3\pi^2 c^3}. \end{aligned} \tag{3.124}$$

The coefficient A, representing the spontaneous emission rate, will be replaced in this work by the value γ_{rad} in order to be consistent with other CQED literature. The spontaneous emission rate of a free electron at a given frequency ω can be calculated via the formula [66]

$$\gamma_{rad} = \frac{\mu_0 |\mu|^2 \omega^3}{3\pi\hbar c^3}, \tag{3.125}$$

where $\mu = -9.284 \times 10^{-24}\,\mathrm{J/T}$ is the electron magnetic moment. The ω^3 term in the numerator of Eq. 3.125 results in a very strong frequency dependence, such that the spontaneous emission rate can be safely ignored at microwave frequencies but becomes very high in the optical frequency range. For a typical operation frequency of $\omega = 2\pi \times 6\,\mathrm{GHz}$ we find that the value of γ_{rad} is of order $\sim 10^{-12}\,\mathrm{Hz}$, corresponding to a time period of about 60000 years. Compared to other losses in the system, γ_{rad} is negligible, and was treated as such during the derivation of the input-output equations for the coupled cavity-spin system.

The Purcell Effect

It is possible to enhance the spontaneous emission rate via coupling to a cavity, known as the Purcell effect [125]. This effect has been used to accelerate the relaxation of solid-state spins [126]. Operating on resonance with the cavity, the Purcell rate is given by

$$\Gamma_p = \frac{4 g_{single}^2}{\kappa_{tot}}. \tag{3.126}$$

For our system, where the single spin couplings are $g_{P1} = 0.19\,\mathrm{Hz}$ and $g_{NV} = 0.29\,\mathrm{Hz}$, and the total linewidth is $\kappa_{tot} \approx 6\,\mathrm{MHz}$, we calculate the Purcell rate to be $\Gamma_p \sim 10^{-7}$, corresponding to about a few months' time. Although greatly enhanced compared to the spontaneous emission, the time constant is still very long and is negligible compared to the other rates within the system.

The stimulated emission rate

We have determined the stimulated emission rate, B, in terms of the spontaneous emission rate γ_{rad}, which in turn can be used to determine the output power of an inverted spin ensemble. The power output P_m can be calculated as

$$P_m = \Delta N W \hbar\omega. \tag{3.127}$$

Where ΔN is the number of inverted spins, ω is the central frequency of emission, and W is the *transition probability amplitude* (units of Hz), which is defined as the Einstein

coefficient B times the electromagnetic energy density per Hertz of the stimulating radiation [66]. The energy density can be estimated as the total magnetic energy E_{tot} divided by the mode volume $\mathcal{V}_c$, and the bandwidth $\Delta\omega$ (i.e. the spin linewidth) is introduced as the frequency band of interest.

When the power output of the inverted ensemble surpasses the power dissipated in the cavity, it enters the *self-oscillating* or *free-running maser* regime where the maser can freely emit microwave photons into the cavity without the need for an applied probe tone. The condition is known as the masing threshold, and the inversion ratio needed to achieve this can be calculated through combining the previous equation with the definition of the cavity quality factor, obtaining the expression

$$P_{loss} = \frac{\omega E_{tot}}{Q_{tot}}, \tag{3.128}$$

where E_{tot} is again the total magnetic energy contained in the oscillating B-field inside the cavity. Setting Eqs. 3.127 and 3.128 equal to each other, we get

$$\Delta N_{th} W \hbar\omega = \frac{\omega E_{tot}}{Q_{tot}}, \tag{3.129}$$

where we have introduced ΔN_{th} as the inversion threshold needed to enter the free maser regime. Using the relationship between B and W,

$$\begin{aligned} \frac{\Delta N_{th} B E_{tot} \hbar\omega}{\mathcal{V}_c} &= \frac{\omega E_{tot}}{Q_{tot}}, \\ \Delta N_{th} &= \frac{\mathcal{V}_c \Delta\omega}{\hbar B Q_{tot}}, \end{aligned} \tag{3.130}$$

Now we want to replace B in the above equation with γ_{rad} and fundamental constants. We do this by inserting Eqs. 3.124 into the above equation, replacing B and A in turn. Putting these equations all together, we arrive at the result

$$\Delta N_{th} = \frac{\omega^3 \mathcal{V}_c \Delta\omega}{\pi^2 c^3 \gamma_{rad} Q_{tot}}. \tag{3.131}$$

Looking at the above equation, we see that in order to generate the lowest possible masing threshold for a given system, the spins and cavity should meet the following criteria:

- small mode volume $\mathcal{V}_c$
- small spin linewidth $\Delta\omega$
- large radiative decay γ_{rad}
- large cavity quality factor Q_{tot}

Some of these criteria are also listed in Ref. [127] in the context of an optical laser. We will use Eq. 3.131 in Chapters 5 and 6 to determine the maser threshold for our diamond samples. If the threshold is low enough it may be possible to generate a self-oscillating maser within the cavity that we develop in Ch. 4.

3.5 Summary

We have established some of the key concepts and derived important parameters of cavity resonators, spin resonance, CQED, and maser physics. These concepts will be used throughout the next three chapters for analysis of the various measurements performed on spin defects in diamond.

Chapter 4

A loop-gap resonator for hybrid quantum systems

4.1 Introduction

In this chapter, I will detail the design, construction, and characterization of the loop-gap resonator used in all subsequent experiments. I will also present evidence of strong coupling between the resonator and the ensembles of NV and P1 centers in our diamond samples. Results on this phenomenon have been published in Ref. [128]; the analysis presented here is intended to supplement said work. In addition, time-domain data will be presented, showing the accelerated lattice relaxation of NV-P1 samples when compared with commercial nitrogen diamond samples that have not been subjected to the electron bombardment and annealing processes. Details about the impurity concentrations and growth methods of the diamond samples can be found in Appendix A. More information on the experimental setup is included in Appendix B.

4.2 The Loop-gap Resonator

4.2.1 Microwave resonator design

The first stage of the experimental setup involves a microwave loop-gap resonator for coupling to the spin ensembles. Given that the resonator was engineered with future use as a quantum transducer in mind, there were several important parameters that needed to be met in the design and construction. Firstly, the resonator had to be optically accessible and able to withstand magnetic fields on the order of 200-300 mT. It was established in Ch. 1 that a number of impurity centers with $g \approx 2$ have spin transitions separated by 5-6 GHz in this regime. The combination of these two conditions eliminates several popular resonator designs used in microwave quantum technology experiments. Many previously-researched hybrid quantum devices (HQDs), for example in Ref. [121], use niobium stripline resonators, but this design is unfeasible for our experiments. The niobium is superconducting at millikelvin temperatures, but both the magnitude of the applied magnetic fields and photons in the visible light spectrum will break the superconductivity. Matching the optical and microwave modes is also much more difficult with a

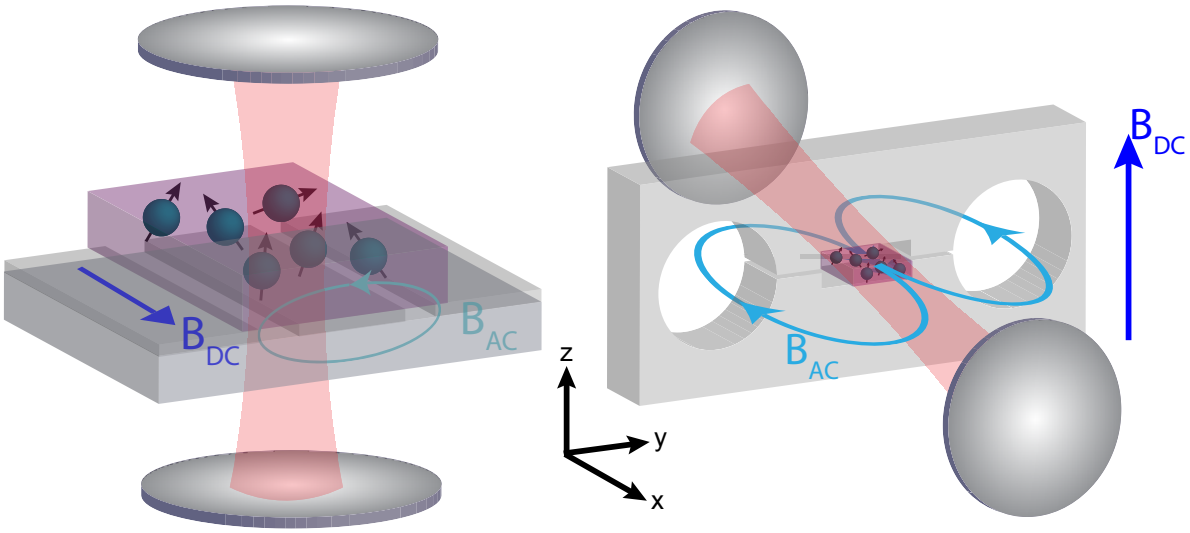

Figure 4.1: Microwave resonator geometry. Left: 2-D stripline resonators, while enabling single-spin coupling an order of magnitude higher than 3-D designs at similar frequencies, also suffer from an inhomogeneous AC field that renders them incompatible with an optical beam. Right: A 3-D loop-gap design allow for a more homogeneous AC field in the center sample mode, higher filling factors, and optical compatibility, at the cost of weaker coupling to individual spins. Since most of the magnetic energy is concentrated in the center mode, better mode overlap with the applied optical beam is possible.

2-D geometry, as seen in Fig. 4.1.

For this reason, we choose a 3-D loop-gap resonator (LGR) design as seen in Fig. 4.1. An LGR consists of a center mode where the sample resides, flanked by two narrow slits to provide the capacitance. The inductance is provided by the material itself in the area of the resonator around the center mode. The electric field fluctuates between the capacitance gap (in the $\hat{z}$-direction) while the magnetic field oscillates in the $x-y$ plane, as defined in Fig. 4.1. Two large openings at the ends of the capacitance gaps provide space for the AC magnetic field, which oscillates in two flux "loops" that both flow through the center mode, similar to a TE_{102} mode in a waveguide. The advantages offered by a 3-D LGR include a more homogeneous AC magnetic field throughout the sample, meaning that many more spins can be equally accessed by the microwave field. This allows the ensemble coupling constant g_{ens} to remain relatively high despite weaker individual spin coupling ($g_{single,2D} \sim 1-10\,\mathrm{Hz}$ vs. $g_{single,3D} \sim 0.2\,\mathrm{Hz}$). This allows for the best mode overlap between the optical and microwave fields while maintaining the ability to tune the spin transition via a static magnetic field. The disadvantages of such a geometry are the lower resonator quality factor due to the lossier material (copper vs. superconducting aluminum/niobium), which is required due to the static B-field, and the inability to tune the resonator frequency *in situ*. We hope to eventually achieve a quality factor of around $Q_{int} = 5000$ for implementation of the quantum transducer, but a lower quality factor will still suffice for ESR measurements.

Having chosen a microwave resonator with loop-gap geometry and made out of copper

to use in our experiments, the designs were then evaluated and tested using COMSOL Multiphysics. The resonator was engineered to have a fundamental frequency around 5-6 GHz, as well as a small sample space around $10\,\mathrm{mm}^3$. The extremely narrow ($\sim 100\,\mu\mathrm{m}$) gap size necessitated that the resonator be built in two identical halves and bolted together. The seam from this junction is indicated by the black dotted line in Fig. 4.2a. An enclosure for the resonator was also designed to minimize radiative losses, and SMA coaxial pins embedded into the enclosure provide the input and output signals. The finalized design and specifications can be seen in Fig. 4.2. Based on the dimensions of the diamond samples we used in this work, the center mode volume was set at 11.5 mm^3, the dimensions of which are seen in Fig. 4.2c.

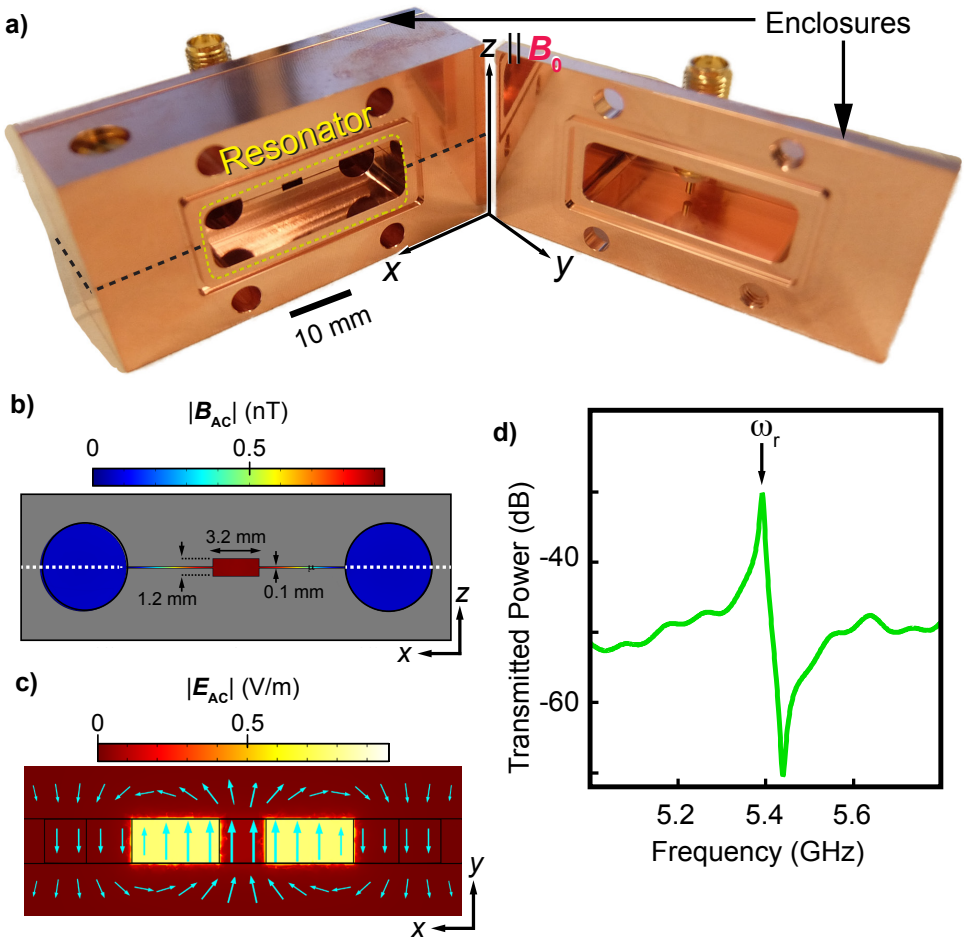

Figure 4.2: Finalized design of the loop-gap resonator. a) Photograph of the resonator and enclosure. The two halves of the resonator meet at the junction indicated by the black dotted line. The yellow dotted line indicates the boundaries of the loop-gap resonator, which is sealed on either end by two enclosure pieces, labeled with black arrows. The enclosure piece on the right is open in order to show the location of the SMA coupling pin. The orientation of the resonator is labeled as well. The static B-field (B_0) is applied in the z-direction and the AC field oscillates along the y-axis in the sample space. b) Front view of the AC magnetic field profile of the main loop-gap mode, calculated using the COMSOL model. The center mode has a high field homogeneity due to the field lines being tightly squeezed through the gap. c) Top view of the inside of the enclosure, with the boundaries of the resonator indicated with solid black lines. The color plot shows the electric field strength as a function of position inside the enclosure. Most of the electric field energy is confined between the narrow capacitive gaps on either side of the sample mode. Direction and relative strength of the AC B-field are also indicated by the cyan arrows. d) Resonance test at room temperature, showing the main loop-gap resonance frequency, which during this measurement was 5.4 GHz.

The resonant microwave magnetic field in the loop-gap resonator is tightly focused

through the sample space and results in a high homogeneity (Fig. 4.2b-d), which can be verified through simulation. The spatial profile of the AC magnetic field throughout the sample was simulated using COMSOL and can be seen in more detail in Fig. 4.3.

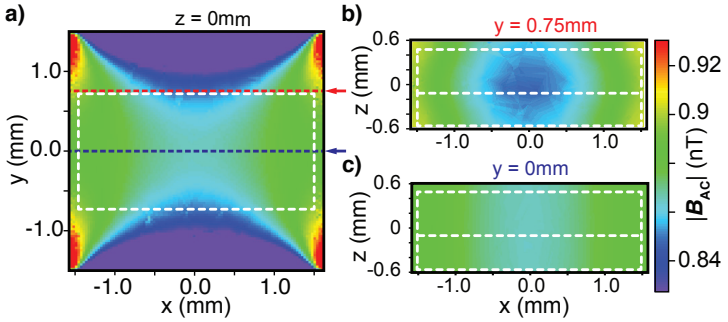

Figure 4.3: Electromagnetic simulation in COMSOL showing the AC magnetic field strength as a function of position inside the sample space. a) X-Y plane at z=0, with the dimensions of the diamond sample shown with the dotted white lines. The field has 93% field homogeneity over the area enclosed by the sample. Cuts used in b) and c) are indicated with the red and blue dotted lines, respectively. b) Cut at $y = 0.75$ mm in the X-Z plane. Dimensions of the diamond samples ($h = 0.5$ mm and $h = 1$ mm) are outlined with the dotted white lines. c) Cut at $y = 0$ mm in the X-Z plane, showing a near-totally homogeneous field near the center of the LG mode.

Using COMSOL it is calculated that the AC field over the sample dimensions is homogeneous to about 93%. Using Eq. 3.61, the vacuum field can be estimated using the relationship

$$\frac{1}{2\mu_0}\int^{\mathcal{V}_c} |\delta B_0(\mathbf{r})|^2 dV = \frac{1}{2}\hbar\omega_r \times \frac{1}{2}, \tag{4.1}$$

where $\mathcal{V}_c = 11.5$ mm^3 is the volume of the sample mode and $\omega_r = 2\pi \times 6$ GHz is the fundamental resonance frequency. Assuming that the field is nearly homogeneous throughout the sample space, the need for an integral is eliminated and we get

$$\delta B_0 = \sqrt{\frac{\mu_0 \hbar \omega_r}{2\mathcal{V}}}. \tag{4.2}$$

Using the numbers above results in $\delta B_0 = 14$ pT. From this, we can estimate the single spin coupling g. We calculate the values for both an NV center and a P1 center in diamond, as we will use these centers to calibrate the resonator. The coupling constants are

$$\begin{aligned} g_{single,NV} &= \frac{1}{\hbar}\langle +1|\hat{H}_{int}|0\rangle = \frac{\gamma_e}{\sqrt{2}}\delta B_0, \\ g_{single,P1} &= \frac{1}{\hbar}\langle +1/2|\hat{H}_{int}|-1/2\rangle = \frac{\gamma_e}{2}\delta B_0. \end{aligned} \tag{4.3}$$

From this we calculate $g = 0.29$ Hz for NV and $g = 0.19$ Hz for P1. Although these values are around two orders of magnitude lower than values of g for 2-D resonator

designs [129][130], this will be sufficient for achieving strong coupling provided that there are enough spins inside the cavity mode, as discussed in Ch. 3.

4.2.2 Resonator characterization

Having fabricated the resonator, we tested the unloaded (without samples inside) cavity at room temperature to verify the resonance frequency ω_r and internal (external) quality factors $Q_{int}(Q_{ext})$. The enclosure is bolted together, using indium to help provide good contact between the surfaces. Two SMA pins are inserted into the enclosure to provide the capacitave coupling between the microwave line and the sample space. The length of the pins extending into the cavity are the primary determiners of the external loss rates κ_1 and κ_2, which we will refer to jointly as κ_{ext}. We examined the coupling between the resonator and the input and output pins for differing values of the height to extract the range of possible quality factors. The equation for transmission through the resonator cavity, derived in Ch. 3 as Eq. 3.31, was written as

$$|t(\omega)|^2 = \left| \frac{i\sqrt{\kappa_1 \kappa_2}}{\omega - \omega_r + i\frac{\kappa + \kappa_{int}}{2}} \right|^2, \tag{4.4}$$

where ω_r is the main resonance frequency, κ_{int} is the loss rate of the resonator, and κ_1 and κ_2 are the loss rates of the input and output pins, respectively. The rates κ_1 and κ_2 are controlled by the distance between the resonator and the pins. This distance is adjusted by stacking washers between the rim of the SMA pin and the enclosure. The results can be seen in Fig. 4.4. Since the transmission formula by itself cannot differentiate between κ_1 and κ_2, and since the height of the washer stack was kept the same on both pins, for simplicity we assume $\kappa_1 = \kappa_2 = \kappa_{ext}/2$, where κ_{ext} is the total external loss rate. The ratio $\frac{\kappa_{ext}}{\kappa_{int}}$ determines the coupling regime: over- (> 1), critical (≈ 1)-, or under-coupled (< 1), see the corresponding section in Ch. 3.

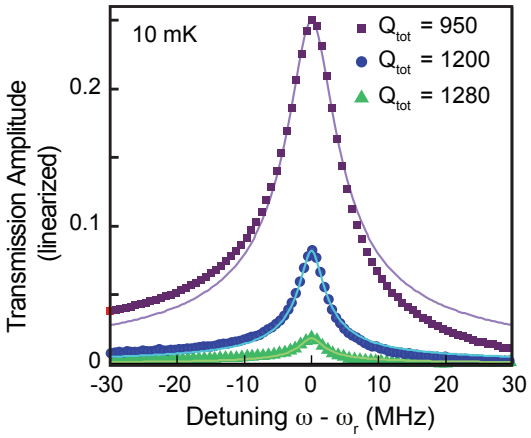

Figure 4.4: Cavity transmission as a function of frequency at 10 mK, along with fitting lines, for different coupling strengths. For this test, $Q_{int} \approx 1300$. External coupling was controlled by stacking washers between the SMA pin and the enclosure surface. Q_{ext} was extracted using the cavity transmission formula, with Q_{int} and ω_r also used as free parameters.

We also use Eq. 3.28 to calculate the mean number of photons in the cavity

$$\bar{n} = \frac{2k_{ext}}{\hbar\omega_r(\kappa_{ext} + \kappa_{int})^2} P_{in}, \tag{4.5}$$

where P_{in} is the microwave probe power at the input port of the resonator. As can be seen from the above equation, the maximum photon injection efficiency for a given microwave power occurs when the system is in the critically coupled regime. This should be easily achievable at low temperature, where $Q_{int} \approx 1300$.

Before continuing further, special attention was paid to other modes of the resonator. The center loop-gap mode must be well-isolated in frequency space from any other "parasitic" modes in order to be able to couple strongly to the spin ensemble. Such parasitic modes are endemic to the LGR itself; others can be generated from the enclosure geometry as well as the SMA pins that are inserted into the cavity. We attempt to prevent this interference with the LG mode by performing a broad frequency scan through the LGR in COMSOL, which will then be verified via experiment. Eigenmodes for the resonator, cavity, and pin system were found using COMSOL, and the results can be seen in Fig. 4.5.

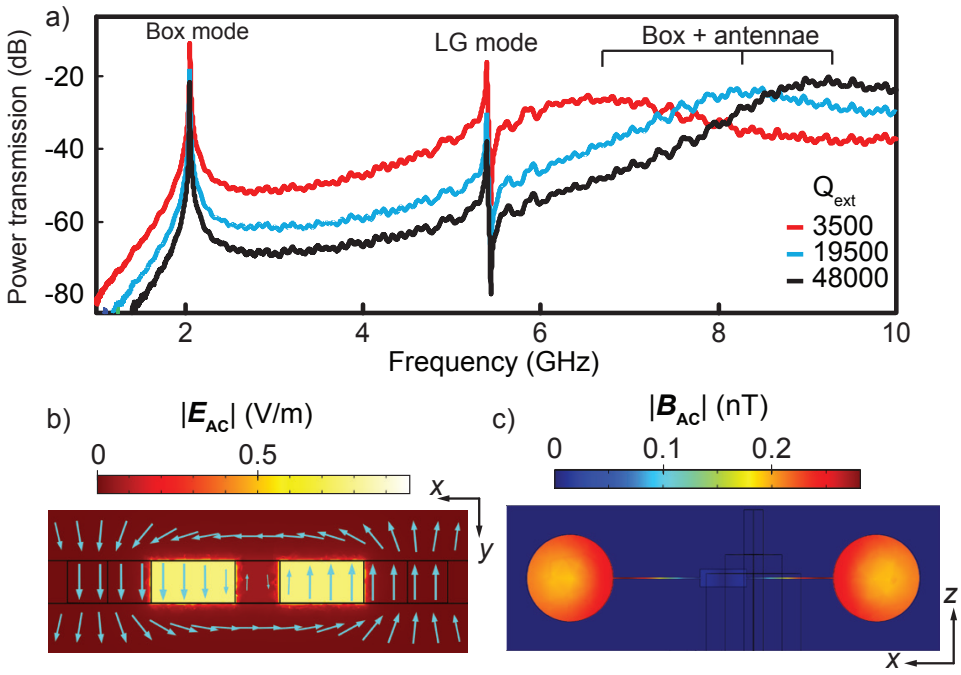

Figure 4.5: Broadband microwave transmission spectroscopy. a) Transmitted power of the unloaded resonator at room temperature, showing box modes as well as the LG and parasitic modes. Different pin heights and lengths affect the position of the parasitic resonance, demonstrating coupling between the pins and cavity. b) Electric field strength as a function of position for the fundamental "box" mode indicated in a). Like the LG mode, the electric field is contained between the capacitive plates but the AC magnetic field oscillates around the center mode (cyan arrows), producing no substantial field in the sample space. c) Front profile of the resonator for the "box" mode, showing the the AC B-field modulus as a function of position in the X-Z plane. Note the absence of field in the center of the resonator, meaning that this mode cannot be used for coupling to the spin ensemble.

These modes were examined using a vector network analyzer (VNA) and an unloaded resonator and enclosure at room temperature. A broadband frequency sweep (100 MHz-14 GHz) revealed the positions of the three main resonances (Fig. 4.5). The lowest frequency peak corresponds to the fundamental mode of the LGR, which we call the "box" mode, where the magnetic field circulates in a single loop through the two large openings and the field in the sample space is near zero, as seen in Fig. 4.5a. In our design this frequency occurs around 2 GHz and thus the separation between it and the "main" LG mode is sufficient. The second such resonance is the main mode, labeled as "LG," and occurring near where it is expected. The final mode is a large, broad parasitic mode occurring near 7 GHz, with the exact location varying based on the external coupling. We determine that these modes are coupled box-pin modes and that the length of the pins extending into the cavity not only alters the external Q-factor but the position of these parasitic modes. As seen in Fig. 4.5, for low quality factors the broad parasitic mode overlaps slightly with the LG mode, resulting in an asymmetric lineshape.

4.3 Experiments on NV/P1 centers

4.3.1 CW measurements

With the resonator fully characterized, proof-of-concept demonstrations of coupling were then performed with ensembles of nitrogen-vacancy (NV) and substitutional nitrogen (P1) centers in diamond. The resonator and ensemble were placed in a dilution refrigerator and cooled down to 20 mK so that the resonator and spins are fully polarized to the ground state. Transmission of the microwave signal through the sample was monitored as described in the previous section and in Appendix B. Note that some transmission measurements in this section have been converted from decibel scale to a linear scale in order to extract the resonator parameters. For these experiments the parameters were fixed at $\omega_r = 5.275\,\text{GHz}$, $Q_{ext} \gtrsim 8\times10^5$, $Q_{int} = 1300$. The first ensemble used is the [110]-aligned diamond, which has an NV concentration of $\sim$ 10ppm and a P1 concentration of 40 ppm (labeled Sample #1 in Appendix A). The energy level schematic for this orientation is illustrated in Fig. 4.6.

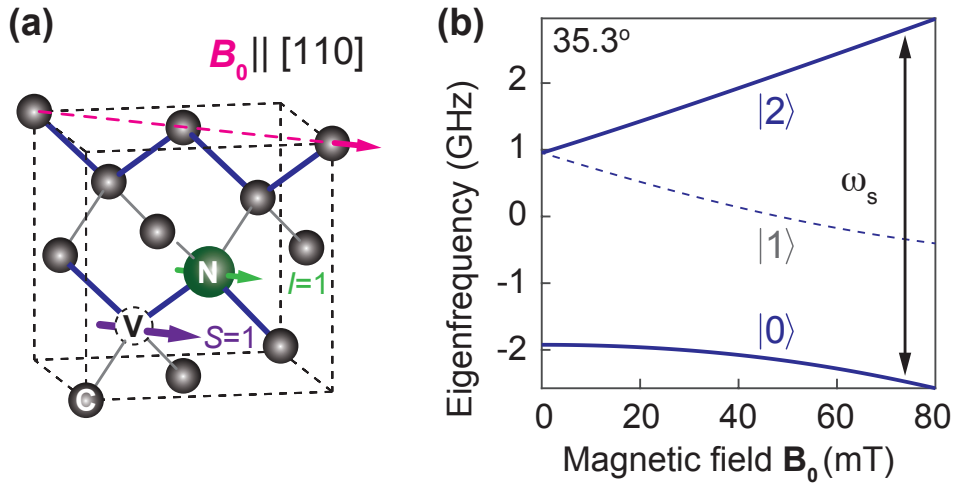

Figure 4.6: The [110]-oriented NV center. a) Structure of the NV center in the [110] B-field orientation. Two species of NV centers are present within this orientation: the orthogonal centers (grey lines), which do not have a detectable transition in this region, and the non-orthogonal centers (blue lines), which make an angle of 35.3° with B_0 One such example of an NV center in this orientation is pictured. b) Energy levels of the $|0\rangle$, $|1\rangle$, and $|2\rangle$ states in NV centers in the [110] orientation of the magnetic field. The point where the $|0\rangle \rightarrow |2\rangle$ transition reaches 5.275 GHz is labeled with a black arrow line.

As seen in Fig. 4.6, our choice of axis for sample 1 results in two distinct spin species over all four possible NV site orientations, those orthogonal to B_0 and those that are non-orthogonal (i.e. have a component along B_0 at approximately 35.3°). The orthogonal transition is not detectable in this mid-field region due to spin selection rules. The non-orthogonal spin species has a resonance frequency of approximately 5.3 GHz at $\approx$ 74 mT, corresponding to the spin transition $|0\rangle \rightarrow |2\rangle$ as indicated in Fig. 4.6b. We use the

annotations $|0\rangle, |1\rangle, |2\rangle$ to describe the spin sublevels in this region due to the mixing of the two lowest levels - meaning that m_s is not a good quantum number. At higher fields the states will again be well described by m_s and the transition between the lowest and highest levels will be forbidden.

Fig. 4.7 shows the results of the spectroscopy test. A probe signal was applied using a vector network analyzer, sweeping the frequency across the cavity resonance at each B-field step. The applied power reaching the resonator was approximately -106 dBm, which corresponds to $\bar{n} = 10000$. This number of photons $\bar{n}$ is many orders of magnitude lower than the number of spins in the sample, assuring that the collective approximation is valid.

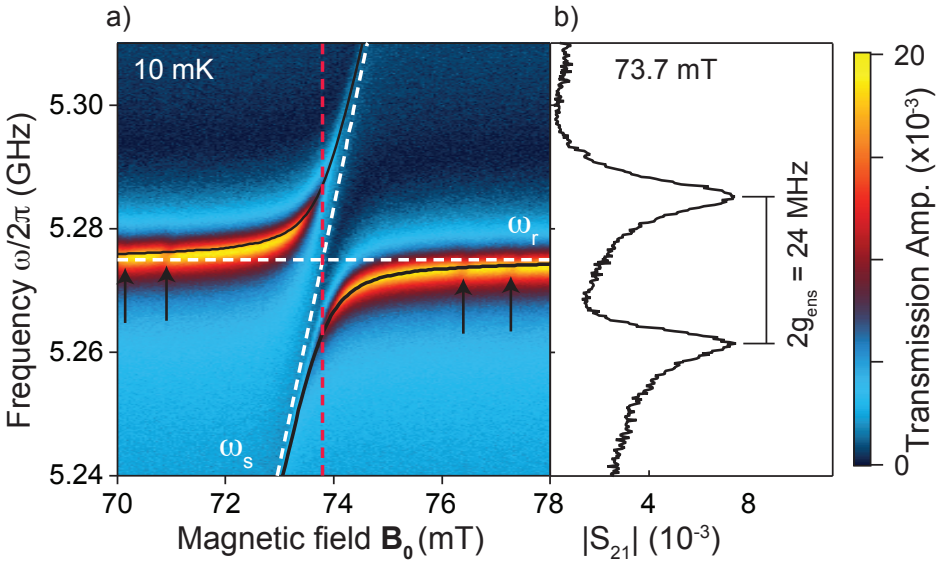

Figure 4.7: Results of the transmission measurements on sample #1. a) Transmission spectrum as a function of magnetic field and frequency for sample #1 at 10 mK. The main mode of the resonator $\omega_r = 5.275\,\text{GHz}$ is labeled with a horizontal dashed line. The $|0\rangle \rightarrow |2\rangle$ spin transition, labeled ω_{NV}, is also indicated with a white dotted line. The two lines intersect at approximately 73.7 mT (red arrows), with the data clearly showing an avoided crossing around that point. The two hybridized levels that arise as a result of spin-resonator coupling are shown with solid black lines. Fine structure due to nearest-neighbor carbon-13 atoms is indicated with black arrows. b) The splitting in frequency space between the two modes at 73.7 mT. The ensemble coupling can be extracted from the distance between the two peaks, giving $g_{ens} \approx 12\,\text{MHz}$.

.

While the experimental value of g_{ens} can be extracted by simply looking at the frequency difference between the polaritonic modes at 73.7 mT, we will determine this value using a more precise method. We fit the transmission spectra data to the coupled Hamiltonian. The frequencies of the polaritonic modes can be found by diagonalizing the following matrix

$$\begin{bmatrix} 0 & g_{ens} \\ g_{ens} & \omega_{NV} - \omega_r \end{bmatrix}, \tag{4.6}$$

which has the eigenvalues

$$\omega_{\pm} = \omega_r + \frac{1}{2}(\omega_{NV} - \omega_r) \pm \sqrt{g_{ens}^2 + \frac{(\omega_{NV} - \omega_r)^2}{4}}. \tag{4.7}$$

Between the region of 70-80 mT (see Fig 4.6b), we approximate ω_{NV} as a quadratic function of B_0, $\omega_{NV}(B_0) = K_0 + K_1 B_0 + K_2 B_0^2$. This expression was inserted into Eq. 4.7 and the values K_0, K_1, K_2, ω_r, and g_{ens} were used as fitting parameters. From this, $g_{ens} = 11.5\,\text{MHz}$ and$\omega_r = 5.2746\,\text{GHz}$ were obtained. The linewidth of the spin ensemble is estimated to be $\Gamma \approx 3\,\text{MHz}$, obtained via deconvolution of the spins and resonator (see Sec. 4.3.4 for details). We can see that the condition $C \gg 1$ is indeed met in this case, and the spin-resonator system is in the strong coupling regime.

We can compare the experimentally-obtained coupling value of $g_{ens} \approx 12\,\text{MHz}$ with the estimated coupling based on resonator geometry and spin concentration, given by the formula

$$g_{ens} = g_{single} \times \sqrt{\rho_{NV} \mathcal{V}_s}, \tag{4.8}$$

where g_{single} is the single-spin coupling previously determined, ρ_{NV} is the NV center concentration of the sample, and $\mathcal{V}_s$ is the sample volume, respectively. Earlier, we estimated g_{single} for NV centers to be 0.29 Hz. In appendix A the concentration of NV centers is listed as 10 ppm, which in diamond corresponds to a concentration of $1.8 \times 10^{18}\text{cm}^{-3}$. However, we must remember that only half of the spin centers are being activated in this configuration. All of these can finally be put together in the formula

$$g_{ens} = 0.29\text{Hz} \times \sqrt{(1.8 \times 10^{18}\text{cm}^{-3})(0.3 \times 0.15 \times 0.11\text{cm}^3)\left(\frac{1}{2}\right)} = 19\,\text{MHz}. \tag{4.9}$$

The difference between the experimental and theoretical values is attributed to the spin transition strength in this regime, which also must be taken into account. As discussed earlier, the system lies in the mixed mid-field regime, where the matrix element for the $|0\rangle \rightarrow |2\rangle$ transition is < 1. By diagonalizing the spin Hamiltonian at the resonance field $B_0 = 73.7\,\text{mT}$ we obtain a matrix element value of 0.75, which when incorporated into the calculation of the coupling gives $g_{ens} = 14\,\text{MHz}$. This agrees more closely with our value obtained via experiments. Nonetheless, we have clearly demonstrated strong coupling between the spins and the loop-gap resonator.

For the second test, a Sample #2 was used, which has a lower concentrations ([NV]=2 ppm, [P1]=16 ppm). Although the lower concentration does make achieving strong coupling more difficult for NV, the alignment of Sample #2 ($\parallel$ [001]) means that all of the spins within the sample have the same projection along the B-field. This avoids the situations where two spin species are created, such as with the NV centers in Sample #1, see the previous section. It was found through investigation of NV centers in Sample #2 that the crystal [001] axis is not perfectly parallel to the applied B-field. These results will be discussed later in this section; for now, P1 centers were chosen as the system for coupling to the resonator. P1 centers are relatively insensitive to a small misalignment of the static B-field. The energy level structure for these centers is shown in Fig 4.8.

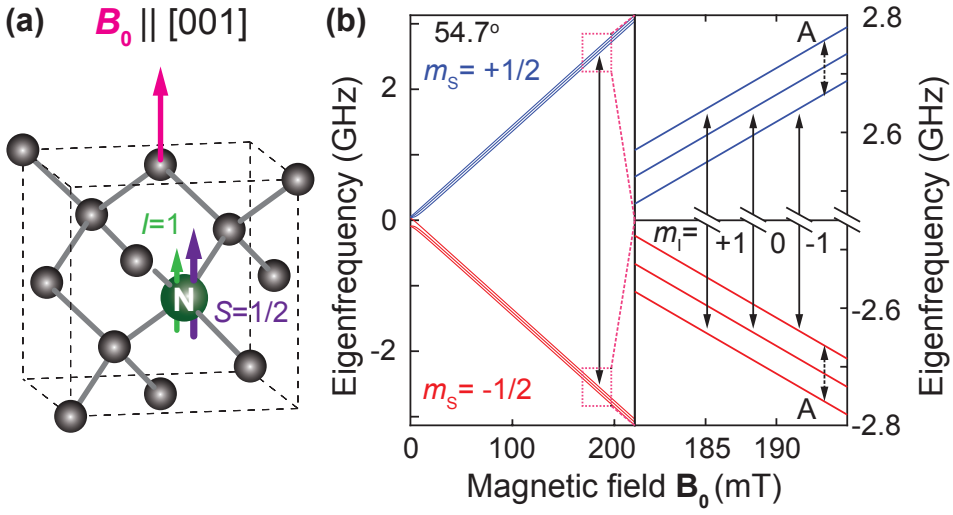

Figure 4.8: The P1 center in the [001] B-field orientation. a) The P1 centers are uniformly aligned to an angle of 54.7° along the static field, meaning that it is possible to drive all spins together with an AC microwave field. b) Energy levels of the $m_s = -1/2, 1/2$ spin sublevels of P1 for the [001] B-field orientation. Zooming in on the region around 185 mT reveals three hyperfine transitions ($m_i = -1$, 0, and +1), which are well-resolved due to the relatively large hyperfine tensor ($|A| \approx 94$ MHz. The point where each of the three hyperfine transitions reaches 5.295 GHz is labeled with a black arrowed line.

The same experimental conditions were used as with the NV centers in Sample #1, however in this case the resonator frequency ω_r has shifted to around 5.293 GHz [1]. The results are illustrated in Fig. 4.9, with three clear avoided crossings due to the nuclear sublevels of the P1 centers. We label these centers P1A, P1B, and P1C for the sake of convenience, and these names will be used throughout the rest of the work.

[1]It should be noted that the thermal expansion and contraction of the resonator during each measurement cycle, along with the indium placed in the seams of the resonator, causes the loop-gap mode to shift in frequency. These shifts can be seen in experiments throughout Chapters 4 and 5.

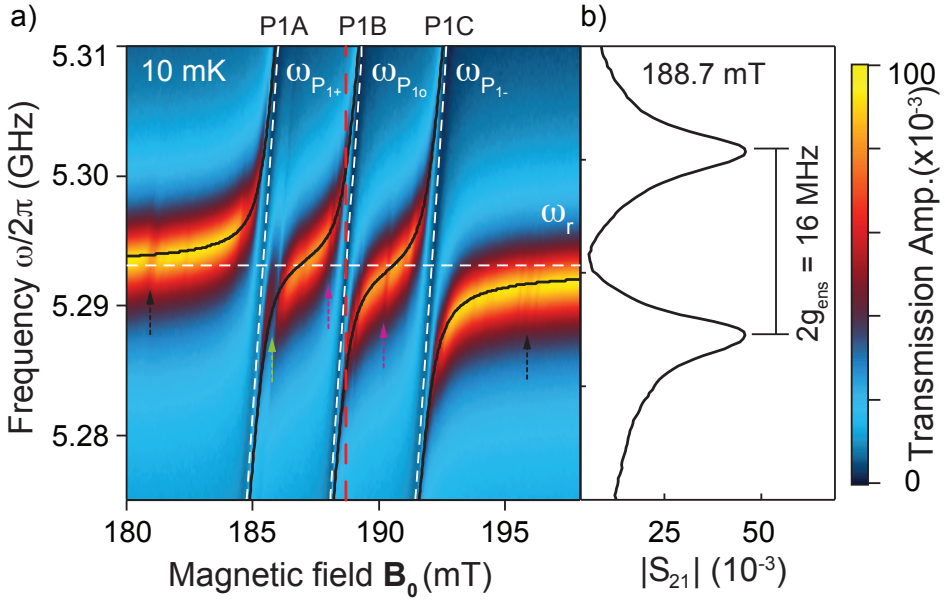

Figure 4.9: P1 transmission data from Sample #2. a) Transmission spectrum as a function of magnetic field and frequency for sample #2 at 10 mK in the region near 185 mT. The main mode of the resonator $\omega_r = 5.293\,\text{GHz}$ is labeled with a horizontal dotted line. The three spin transitions corresponding to the nuclear spin sublevels, labeled $\omega_{P1,+}$, $\omega_{P1,0}$, $\omega_{P1,-}$ respectively are also indicated with a white dotted lines. We name these three transitions P1A, P1B, and P1C. The hybridized levels that arise as a result of spin-resonator coupling are shown with solid black curves, which are found through matrix diagonalization. Fine structure due to nearest-neighbor carbon-13 atoms is indicated with black arrows. An NV transition near $\omega_{P1,+}$ is labeled with a green arrow, and two "unknown" spin centers, later determined to be R4, are indicated with pink arrows. b) The splitting in frequency space between the two modes at 188.7 mT. The coupling can be extracted from the distance between the two peaks, giving $g_{ens,0} \approx 8\,\text{MHz}$.

Due to the increased complexity of the spin system, i.e. three modes coupled to the resonator instead of just one, a closed-form solution for the polaritonic modes (c.f. Eq. 4.7) cannot be derived. The model for obtaining the four polaritonic modes can, however, be obtained through numerical diagonalization of the 4×4 interaction matrix. For the P1 centers, the eigenenergy matrix can be written

$$\begin{bmatrix} 0 & g_{ens,-} & g_{ens,0} & g_{ens,+} \\ g_{ens,-} & \omega_{P1,-} - \omega_r & 0 & 0 \\ g_{ens,0} & 0 & \omega_{P1,0} - \omega_r & 0 \\ g_{ens,+} & 0 & 0 & \omega_{P1,+} - \omega_r \end{bmatrix}, \tag{4.10}$$

where $\omega_{P1,j}$ refers to the resonance frequencies of the three P1 hyperfine transitions ($j = -1, 0, +1$) at a given magnetic field. These values were found via EasySpin [131] and then numerically diagonalized with $g_{ens,-}, g_{ens,0}, g_{ens,+}$, and ω_r as the fitting parameters. As a result, the values 7.8 MHz, 7.9 MHz, and 8.8 MHz were obtained for the three coupling values, and 5.2929 GHz for the resonator frequency. The linewidth is calculated

to be 1.3 MHz. The pythagorean sum of these values gives the total coupling to all three P1 transitions

$$\begin{aligned} g_{ens}^2 N_{total} &= g_{ens,-}^2 + g_{ens,0}^2 + g_{ens,+}^2 \\ , g_{ens} &= \sqrt{(7.8\,\mathrm{MHz})^2 + (7.9\,\mathrm{MHz})^2 + (8.8\,\mathrm{MHz})^2} = 14.1\mathrm{MHz}. \end{aligned} \tag{4.11}$$

Once again comparing the above experimentally-obtained coupling value with the estimated coupling based on spin concentration,

$$g_{ens} = g_{single} \times \sqrt{\rho_{P1} \mathcal{V}_s}, \tag{4.12}$$

where g_{single} is the single-spin coupling to P1, approximately 0.19 Hz. In Sample #2 the concentration of P1 centers is 16 ppm ($2.9 \times 10^{18}\mathrm{cm}^{-3}$), however the physical size of the sampler is smaller than Sample #1. Putting these values in the formula, we obtain

$$g_{ens} = 0.19\mathrm{Hz} \times \sqrt{(2.9 \times 10^{18}\mathrm{cm}^{-3})(0.3 \times 0.15 \times 0.05\mathrm{cm}^3)} = 15.3\,\mathrm{MHz}. \tag{4.13}$$

Which agrees reasonably well with our calculated value. We have thus demonstrated strong coupling between the resonator and two different ensembles of spin centers in diamond. Our loop-gap resonator is thus viable for further experiments in spin-based hybrid quantum systems, such as for spin quantum memories or a quantum transducer. However, in this work we will continue to examine interesting features of the low-temperature ESR data, which will eventually reveal the mechanism of a spin-based cryogenic maser amplifier.

4.3.2 Identification of spin centers

In addition to the strong coupling to the P1, a number of interesting secondary features in Fig. 4.9 jump out, notably the presence of spin transitions in the same region that are not either the P1 or NV main transition. Several of these transitions are in fact carbon-13 satellites that are easily distinguished by using the well-known hyperfine tensor [132], shown with dashed lines in Fig. 4.10. The second is a relatively strong transition near $\omega_{P1,+}$ (P1A) that was found to be due to an NV center. Normally well-separated in frequency space from the P1 center, this particular NV resonance was pushed to higher field due to misalignment between the crystal [001] axis and the lab frame $z-$axis. To determine the misalignment angle, a program was created in Matlab, making use in part of the EasySpin software package [131]. This allowed us to calculate transition frequencies as a function of field and overlay them onto the 2-D transmission data, adjusting the misalignment angles as appropriate. Fig. 4.10 shows the results of the attempt to identify all of the spin centers by simulating P1, NV, and associated ^{13}C centers. This, however, does not identify all of the spin transitions that can be seen in the plot. Therefore, we turn to other spin centers such as the vacancy clusters introduced and discussed in Ch. 1. Using the parameters listed in Ch. 1 we also overlay spin transitions of the R4/W6 (divacancy) and O6 and R7 (quadruple-and quintuple-vacancy) spin defects onto Fig. 4.10. As discussed in subsequent sections, it is likely that R5 centers are also present in the sample, however none of the transitions fall within the magnetic field and frequency range of Fig. 4.10.

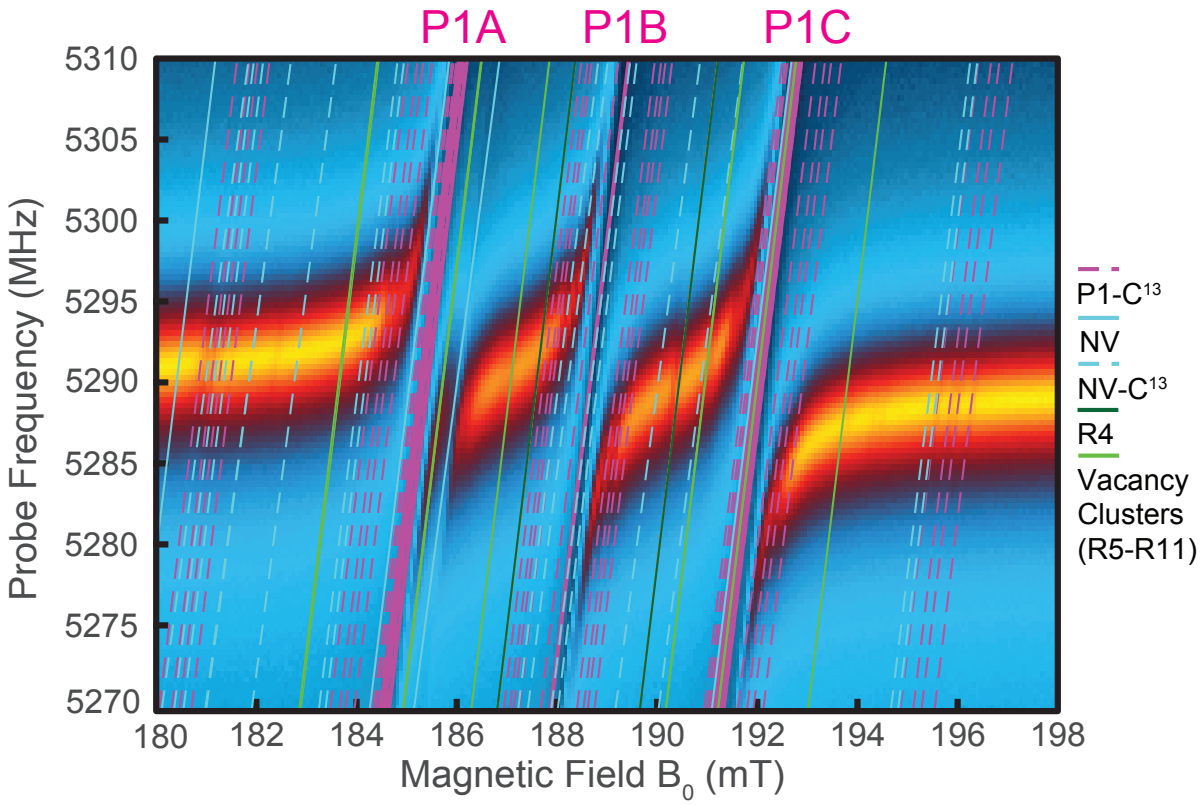

Figure 4.10: Full transmission spectrum as a function of magnetic field and frequency for sample #2 at 10 mK. The main color plot is overlaid with lines indicating the spin transition frequencies as a function of magnetic field. In addition to the three main P1 transitions, an NV transition is present near $\omega_{P1,+}$ due to the misalignment of the B-field relative to the [001] crystal axis.

4.3.3 The nitrogen-dense sample

For the sake of comparison, it is helpful to look at a sample that only contains nitrogen centers and has not been subjected to the process of electron bombardment used to create the nitrogen vacancies and thus the other impurity centers. We obtained a HPHT Ib diamond sample grown at Sumitomo Electric Industries which we refer to from now on as "Sample #3" (see Appendix A). The nitrogen concentration, although not precisely known, is significantly higher than in Sample #2, so we expect to achieve strong coupling to the P1 centers in Sample #3. Like Sample #2, Sample # 3 is grown in such a way that the [001] axis aligns with the lab z-axis, i.e. the direction of the static magnetic field. The P1 ESR spectrum in the regime of 185-210 mT should thus look very similar to Fig. 4.10. As mentioned above, the sample should not have an appreciable quantity of nitrogen vacancies and thus we only expect to see the three main P1 transitions. Sample #3 was placed in our resonator and subject to the same cw-microwave experimental procedure of Samples #1 and #2. Fig. 4.11 shows the results of the coupling test of Sample #3. The transmission data is dominated by the large coupling to each of the P1 transitions, and other than some faint lines due to 13C there are no other notable transitions in this

regime.

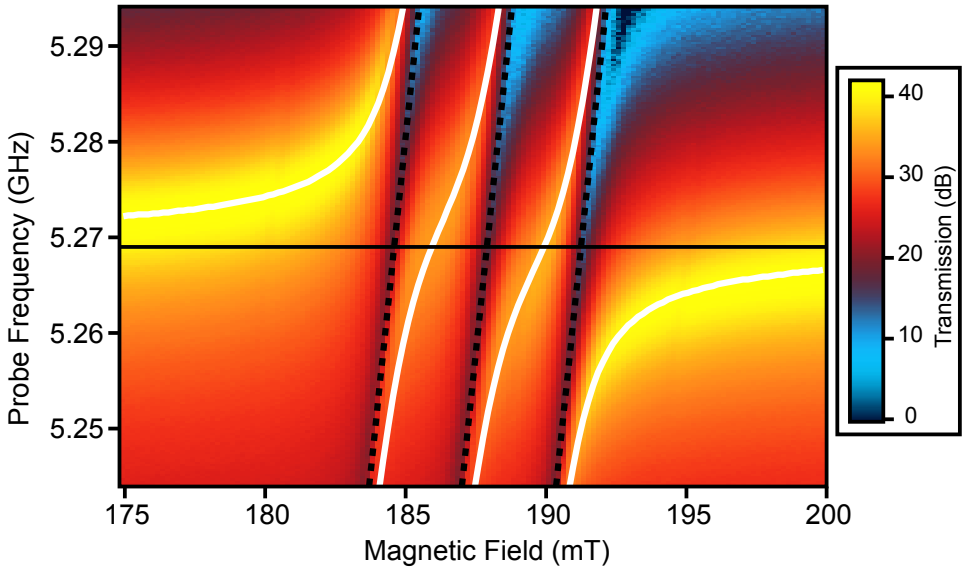

Figure 4.11: Transmission spectrum as a function of magnetic field and frequency for sample #3 at 10 mK. The main color plot is overlaid with lines indicating the spin transition frequencies as a function of magnetic field (black dotted lines) and lines indicating the polaritonic modes (solid white lines). From these the coupling values $g_{ens,-}$ $g_{ens,0}$ $g_{ens,+}$ are obtained. No other notable transitions are present, indicating a lack of vacancy clusters or NV centers.

Following the same procedure as with Sample #2 we extract $\omega_r = 5.269\,\text{GHz}$ for the resonator frequency, $Q_{tot} = 700$ for the total quality factor, and $g_{ens(-,0,+)} = 18, 18.48, 16.84\,\text{MHz}$ as the ensemble coupling constants, respectively. Although the precise concentration of the sample is not known, we estimate [P1] = 50 ppm based on the total ensemble coupling and the size of Sample #3.

From the results of Sample #3 shown in Fig. 4.11, it can be deduced that the extra transitions present in Sample #2 are due to vacancy centers created during the process of electron bombardment. In the next section, we will perform time-domain measurements to examine the effects of the vacancy centers on the system relaxation rates.

4.3.4 Time-domain experiments

It has been demonstrated in literature that while centers such as P1s and NVs have incredibly long lattice relaxation times at low temperature [25], vacancy clusters such as R4/W6 and R5 centers have much shorter relaxation times [133]. Now that we have established the presence of R4/W6 and R5 centers in our sample, it is interesting to look at the effect of these "fast" centers when their transition frequencies nearly overlap those of the "slow" centers.

We look at Sample #3 first to establish the timescale of T_1 in P1 centers at 10 mK. The fact that each of the P1 transitions is strongly coupled to the resonator makes measuring T_1 on resonance (e.g. by saturation recovery) more complicated. It can be done, however,

through measuring the *dispersive shift* in a manner similar to one employed in cavity- and circuit-QED experiments such as in Ref. [134]. The process can be seen in Fig. 4.12a. Sample #3 is cooled to ≤ 20 mK and the spectrum is measured using the VNA. For both P1A and P1C the field is fixed to the point where the resonance frequency of the transition is detuned from the main cavity resonance by 70 MHz, which is several times the ensemble coupling strength (satisfying $\Delta_s \gg g_{ens}$). A microwave pump tone is applied using a signal generator to saturate the spins off-resonantly. After the spins are fully saturated, the VNA monitors the shift of the resonance frequency of the cavity over time. From Chapter 3, we established that when the resonator and spins are detuned by a value greater than the coupling g between them, then the systems cannot exchange energy directly. However, the frequencies of each system are "pulled" slightly depending on the state of the other. This allows us to remove the effect of the resonator coupling to the spins and also monitor the spins indirectly through the resonator. As the spins ($\sim N$) recover from saturating, the ensemble coupling g_{ens} increases and thus the shift of the cavity resonance from its "natural" frequency ω_r also increases. A sample data set it seen in Fig. 4.12b. The microwave probe tone is swept across the cavity resonance at each time interval, and the resonator frequency and quality factor at each step can be extracted by fitting the phase using the function derived from the angle of 3.31,

$$\phi(\omega) = \phi_0 - \Delta \arctan\left(\frac{2(\omega - \omega_r)}{\kappa_{int} + \kappa_{ext}}\right). \tag{4.14}$$

Where ϕ_0 and Δ are fitting parameters representing the phase offset and span. Two example phase fits are pictured in Fig. 4.12b. The evolution of $\omega - \omega_r$ over time behaves as an exponential function from which the lattice relaxation times T_1, A and T_1, B can be determined. The two different relaxation times are attributed to the diamond forming facets during growth, meaning that different regions of the diamond can have varying concentration of nitrogen. The dispersive measurement experiment was performed on both the P1A and P1C transitions at 10 and 100 mK, and the results are seen in Fig. 4.12c-d.

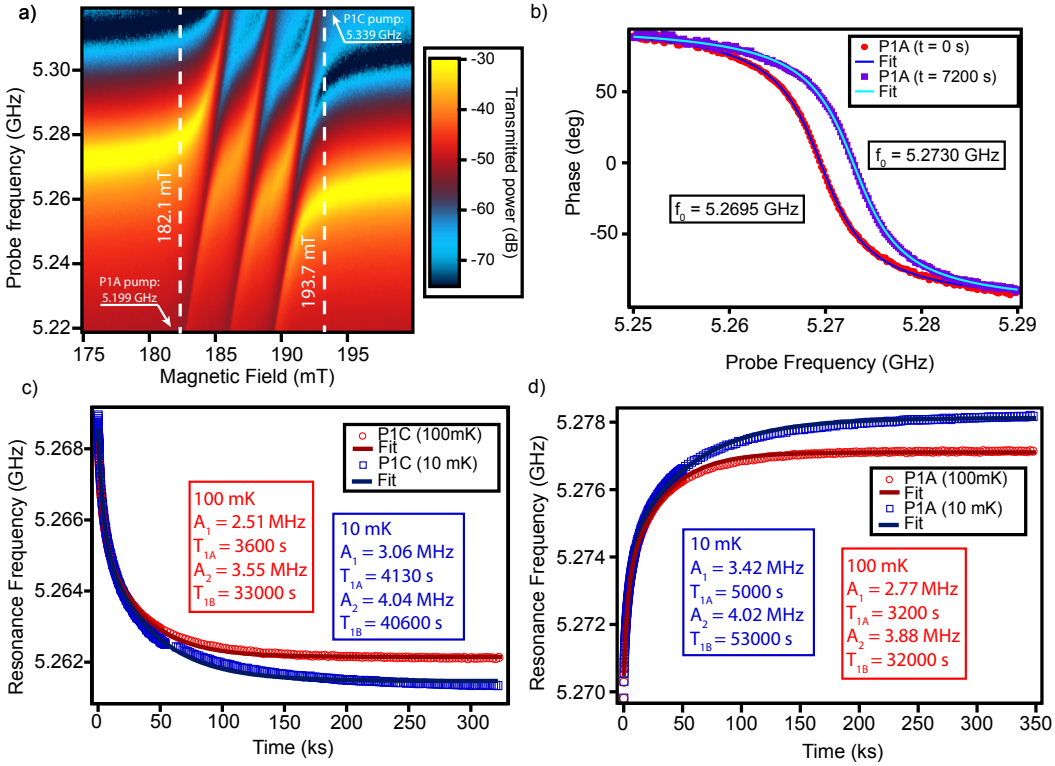

Figure 4.12: Results of dispersive measurements of T_1 for the P1A and P1C transitions of Sample #3. a) VNA map of transmission power in the region near the P1 transitions. The VNA is centered on the resonator frequency (5.293 GHz). For dispersive measurement of P1A (P1C), B_0 is fixed at 182.1 mT (193.7 mT) and the saturation frequency is applied at 5.199 GHz (5.339 GHz). The resonator and spin transition frequencies are thus separated by about 70 MHz. b) Sample phase traces taken during the P1A saturation recovery. The shift in the resonator frequency can be extracted by fitting the data. c) Frequencies of maximum transmission power as a function of time for P1C. The measurements were performed at 10 mK and 100 mK and the data was fitted with a double-exponential function. d) The same dispersive measurements performed on P1A at 10 and 100 mK, with the double-exponential time constants indicated on the plot.

As can be seen from the data depicted in Fig. 4.12, the spin-lattice relaxation T_1 times of the P1 centers, absent any other spin defect centers in the sample, are extremely long, with the fits to the data returning two time constants of $\sim$ 1 hr and $\sim$ 10 hrs. Next, we will probe the lattice relaxation times of the defect-rich Sample #2 to determine the effect of the added vacancies.

We use the following measurement technique for measuring the T_1 of the P1 centers in sample #2. Note that beginning with these experiments, we have switched from measuring the transition to the reflection spectrum. See Appendix B for information on the exact changes made in this setup. This allows us to more-easily compensate for the background signal of the spectra due to the measurement lines and electronics. First, to determine the parameters of the resonator we take a frequency profile when it is far detuned from

any spin resonance. This profile and the extracted resonator parameters are illustrated in Fig. 4.13a, with extracted values of $\omega_r = 6.263\,\text{GHz}$ and $Q_{tot} = 550$. Following this, we determine the magnetic field where the P1 centers transitions are resonant with the LG resonator. We set the field modulus at this value and then saturate the P1 centers on-resonance with a signal generator. Saturating on-resonance ensures that the entire bandwidth of the spin ensemble is pumped by the PSG tone. As the spins relax from saturation, resonator spectroscopy is performed using the VNA. These traces as a function of time are shown in Fig. 4.13 and show relaxation from the bare resonator profile to the polaritonic-mode behavior characteristic of strong coupling. The relaxation time is clearly much quicker than in the previous measurement. However, as noted in the previous section, the effect of the resonator must be removed in order to accurately determine the characteristic time T_1 of the spins. We thus perform the following procedure to deconvolute the resonator and the spins. The background is subtracted from the raw magnitude data so that the off-resonance reflected power is ≈ 0 dB. The magnitude data is then linearized and combined with the phase data,

$$R(\omega) = |R(\omega)|^{i\phi(\omega)}. \tag{4.15}$$

We then reintroduce the spin function $K(\omega)$ introduced in Ch. 4. We can easily rearrange the expression to calculate $K(\omega)$ in terms of $R(\omega)$,

$$K(\omega) = \omega - \omega_c + \frac{i}{2}\left(\kappa_L + \kappa_1 \frac{R(\omega)-1}{R(\omega)+1}\right), \tag{4.16}$$

where ω_c, κ_L, and κ_1 are the resonator parameters which we have determined in Fig. 4.13. This removes the effect of the strong coupling to the resonator from the spins. The imaginary part of $K(\omega)$ is directly proportional to the spin density, which we will now calculate. We assume that the distribution of the spin defect frequencies constitutes a Lorentzian function given by

$$\rho(\omega) = g_{ens}^2 \frac{\Gamma/\pi}{\omega - \omega_s}, \tag{4.17}$$

where ω_s and Γ are the spin resonance and linewidth, respectively. This function is normalized as

$$\begin{aligned} \int \rho(\omega) d\omega &= g_{ens}^2 \int \frac{\Gamma/\pi}{(\omega-\omega_s)^2 + \Gamma^2} d\omega \\ \int \rho(\omega) d\omega &= g_{ens}^2 \\ \frac{1}{g^2}\int \rho(\omega) d\omega &= N. \end{aligned} \tag{4.18}$$

Note that in the last line we have substituted $g_{ens} = g\sqrt{N}$, where g is the single-spin coupling. To determine the number of spins from our data we can use the relationship between $\rho(\omega)$ and the imaginary portion of $K(\omega)$ [32],

$$\rho(\omega) = -\frac{1}{\pi}\text{Im}[K(\omega)]. \tag{4.19}$$

Combining this with Eq. 4.18,

$$N = -\frac{1}{\pi g^2} \int \mathrm{Im}[K(\omega)] d\omega. \tag{4.20}$$

This can be expressed more generally as a spin density as a function of frequency $n(\omega)$,

$$n(\omega) = -\frac{1}{\pi g^2} \mathrm{Im}[K(\omega)]. \tag{4.21}$$

Having established the expression for n, we can now calculate the total number of spins in any given bandwidth. The function $n(\omega)$ is plotted in Fig. 4.13c and shows a steady increase in time as the spins relax. Note that the negative sign in n means that the function is positive for absorbing spins and will become negative for an inverted spin ensemble (see Ch. 5). From the profiles of n vs. time the lattice relaxation times $T_{1,AB}$ can be determined (Fig. 4.13d). It is clear that the P1 relaxation times are greatly accelerated in this sample, by a factor of ~ 10. We attributed this acceleration to the presence of nearby vacancies formed through electron irradiation and annealing of the sample, specifically via direct flip-flops between the P1 centers and vacancy clusters. An explanation of this mechanism, as well as an estimate of the flip rate Γ_{flip} based on experimental data, is included in Ch. 6. Note that, like Sample #3, the two relaxation rates are attributed to the diamond containing different facets with varying concentrations of both P1 centers and vacancy clusters. These facets can clearly be seen with the naked eye upon inspection.

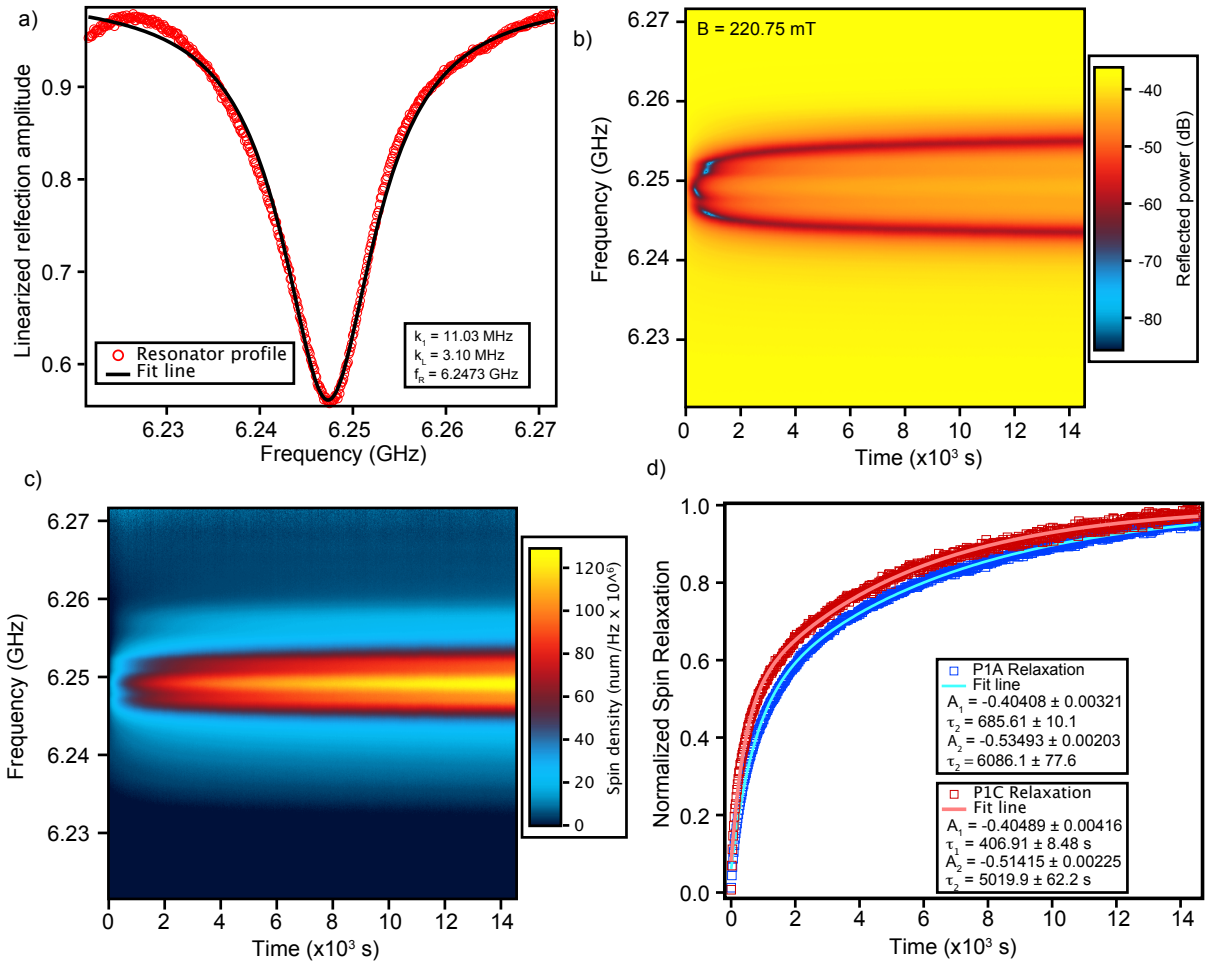

Figure 4.13: Results of saturation recovery measurements of T_1 for the P1A and P1C transitions of Sample #2. a) Linearized reflection profile of the resonator at a magnetic field off-resonant from the spin ensemble. The resonator parameters extracted from the fit are shown in the box. b) Time evolution of the P1A transition near the resonator frequency following the saturation. When the spins are saturated, the sprectrum is characterized by a single dip in the reflected power. As the spins relax, the spectrum once against returns to the double reflection dips that is the result of the strong coupling between the P1 centers and and the resonator. The splitting grows wider as the spins return to their equilibrium state. c) The time-evolution of the spin profile as a function of frequency when the resonator and spins are deconvoluted. The spins clearly show recovery from saturation as time increases. Note that the misalignment of the B-field results in broadening of the spin profile. d) Normalized spin recovery as a function of time, obtained by integrating the traces in (c). The data sets are fitted with a double-exponential model and the extracted T_1 values are shown on the plot. Notice that they are greatly accelerated when compared to Fig. 4.12.

4.4 Locating the R5 center

Having shown the acceleration of the P1 centers, we now attempt to locate evidence of the R5 center within the sample. We anticipate the concentration of R5 is very small (1 ppb), and thus difficult to detect using cw-microwave spectroscopy. For this reason, we switch to a time-domain setup, using homodyne-detected Hahn echo method to detect R5. The same sample and magnetic field orientation is used for these experiments. The pulse envelopes are generated using an arbitrary waveform generator (AWG) and mixed with a microwave signal generator (MSG) at a frequency resonant with the microwave cavity ($\omega_r = 5.961$ GHz). After being transmitted to the cavity, the reflected signal is amplified at 4K, demodulated using the local oscillator signal from the MSG and amplified again at room temperature, and measured using a PC fast acquisition card. Further details of the setup are described in Appendix B. The pulse sequence itself is a standard Hahn echo sequence as illustrated in Fig. 4.14a. In this case we use two pulses of the same length but the amplitude of the second pulse is increased by twice that of the first. Moreover, since the R5 center lies among many other spin transitions in this orientation, we will "silence" the other transitions by applying a 1 second, frequency-modulated saturation pulse prior to the echo sequence. By allowing only 1 second between the pulse and the echo sequence, we ensure that only the spin transitions with the shortest values of T_1 will be detectable. The detected spin echo as a function of B-field can be seen in Fig. 4.14. The R5 transition, which should lie between 220-225 mT, could not be directly detected. The reason for this is still unclear, but it may be related to the very broad background resonance visible between 215-230 mT in Fig. 4.14b. The origin of this broad signal is also unclear, but may be a stray paramagnetic resonance due to water or oxygen condensation on the resonator. Such resonances have been observed previously in the context of superconducting resonators [135].

What is clear from Fig. 4.14, though, is that the relaxation of the high-field (P1C) transition is accelerated when compared to the other P1 transitions, indicated by the large echo signal present even after thoroughly saturating the spins. This asymmetry in T_1 between P1 satellites will be used in Ch. 6 to generate inversion on the lower-field satellite via cross-relaxation.

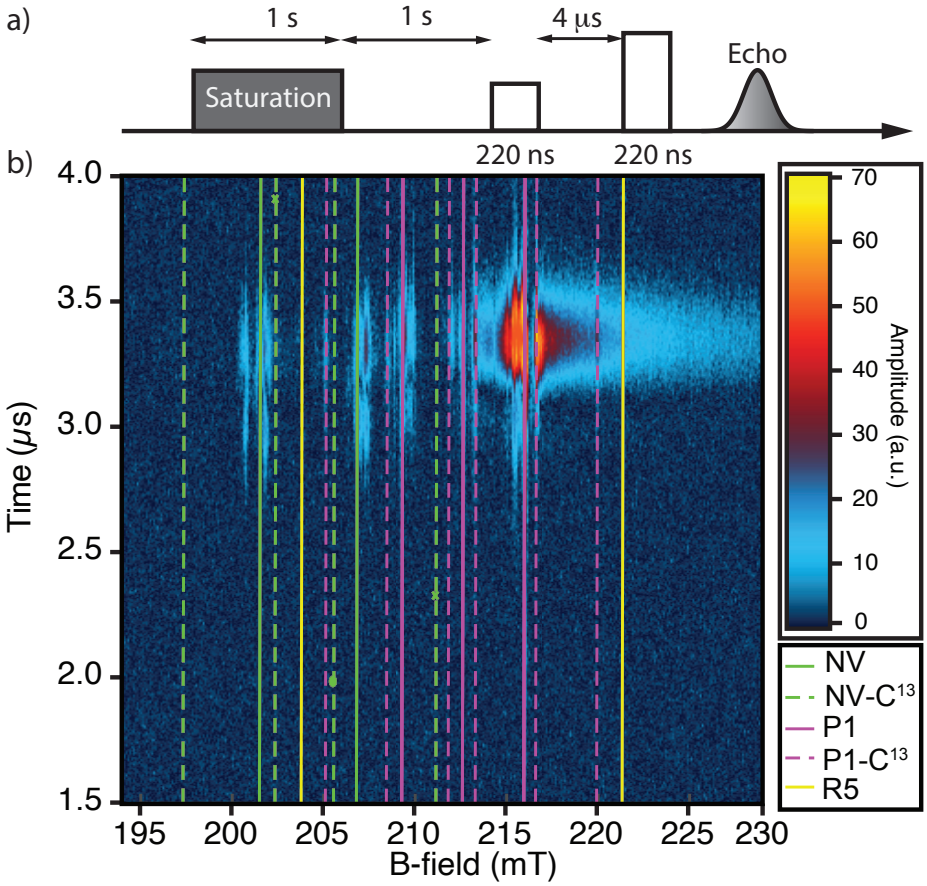

Figure 4.14: Hahn echo intensity vs. B-field. a) The saturation and pulse sequence used for the measurement. A 1 s, frequency-modulated saturation pulse is applied to the spins, followed by a 1 s-long delay time. This allows for the detection of spins with short T_1. After the 1 sec delay, a standard Hahn-echo sequence with 4 μs delay between the two pulses is employed. b) Echo amplitude versus B-field magnitude. Several NV (solid green lines) and P1 (solid purple lines) transitions are visible, as well as accompanying paired ^{13}C centers (green/purple dashed lines). The location of the R5 center is indicated with a solid yellow lines, however the R5 transition is not visible within the echo data, possibly due to the large, broad background signal present between 215-230 mT. It is clear, however, that the relaxation of high-field P1 satellite is greatly accelerated relative to the low-field satellite.

Having been unsuccessful at detecting R5 in this orientation, we tilt the B-field 90°, from the [001] crystallographic axis to the [110] direction and once again perform cw-microwave spectroscopy on our sample. Shifting the field to this direction removes all NV transitions from the region of interested, as they are all pushed to higher or lower frequencies, as seen in the region near 160 mT in Fig. 4.15. Some of the NV centers are now oriented perpendicularly to the applied B-field, resulting in extremely weak transition amplitudes. For this reason, not all main NV transitions can be detected. Regardless, in the region of interest (200-220 mT), we clearly see five P1 transitions as a result of the new alignment. Two transitions also appear at ≈205 mT and ≈ 221 mT. These spin

transitions, indicated by the yellow lines, were at first thought to be ^{13}C-P1 satellites, but upon further investigation it was found that they are too far separated in frequency space from the main P1 transitions for this to be the case. These transitions were ultimately determined to be manifestations of R5. By overlaying the calculated spin transition frequencies onto the data, as in Fig. 4.15, we determined the R5 D-tensor to be about 0.82 of the value reported at low temperature in Ref. [19], with a value of $D_{zz} = -328\,\text{MHz}$. The perpendicular components were in the range of $D_{xx}, D_{yy} = 200 - 233\,\text{MHz}$, but it should be noted that the exact orientation of D relative to B_0 could not be determined by the current data. By demonstrating that R5 is present in our sample and determining the most accurate spin parameters, we can optimize the performance of our maser amplifiers which are based on the R5 spin-flip mechanism. At the time of writing we have not been able to perform time-domain spectroscopy on these detected R5 centers, but this is the logical next step.

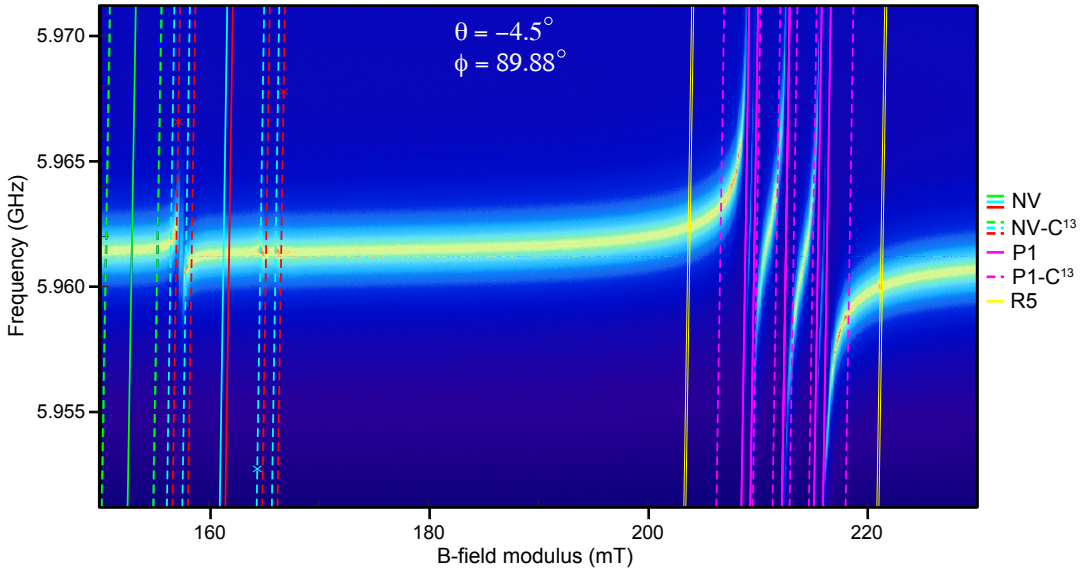

Figure 4.15: Wide-field VNA scan showing evidence of the R5 center. The field is tilted into the [110]-plane (lab $y - z$ plane) while maintaining a slight ($< 5°$) offset about the x-axis. The splitting of P1 and NV into subspecies can clearly be observed. The main NV resonances (solid green/cyan/red lines) near 160 mT are not detected either due to weak transition matrix elements or negligible spin population. Transitions involving paired NV-^{13}C centers (dotted green/cyan/red lines) are seen on either side of the main NV transition. Of the three main P1 transitions (solid pink lines), the two outer satellites are also split into two subspecies that are both clearly detectable. In this orientation the R5 center (yellow clearly manifests outside the P1-^{13}C center satellite transitions. The $-1 \rightarrow 0$ transition is located at higher field (≈ 220.5 mT), and shows a correspondingly higher absorption than the $0 \rightarrow 1$ transition. From this data we can estimate the D-tensor of R5.

4.5 Conclusion

We have designed a microwave loop-gap resonator for applications in quantum technology and demonstrated strong coupling to an ensemble of NV and P1 centers. During this process we have shown that the lattice relaxation times of the ensemble P1 centers can be accelerated by the presence of other vacancy clusters (particularly R5 centers), which are also present in our sample. In the next chapter we will attempt to engineer this acceleration of T_1 to our advantage by using it to implement a thermal maser.

Chapter 5

A thermal maser in diamond

5.1 Theoretical model

5.1.1 Engineering Spin flip-flops

We have seen in a number of maser and laser systems explored in Chapter 2, particularly thermal masers and gasdynamics lasers, that a way to achieve population inversion within a long-lived spin system is to pair it with a faster-relaxing system, or the other way around. If the energy gaps between levels of the slow and fast systems are well-matched, the relaxation of the slow system can be accelerated. If the system begins in a high-temperature Boltzmann state ($k_B T \gg \hbar\omega$) and is cooled to low temperature quickly, it may be possible to achieve a temporary population inversion. Of course, without an active pump this inversion will only last for a finite amount of time before the entire system relaxes to thermal equilibrium, i.e. the lowest energy spin state at millikelvin temperature. Nonetheless, such a maser has the potential to be much longer-lived than other experimental realizations of the thermal maser, as discussed in Ch. 2.

We can use two spin species present within our [001]-aligned Sample #2 to establish such a coupled system necessary for a thermal maser. The long-lived system will consist of NV centers, which at 10 mK has a lifetime of nearly 10 hours. The fast system will consist of vacancy clusters that are present as a result of the electron irradiating process. The spin Hamiltonians and parameters of both of these spin systems were discussed in Chapter 4. By engineering the direction and magnitude of the applied magnetic field, the conditions required for spin flip-flops between R5 and NV centers can be created. When the B-field is aligned precisely to the diamond's [001] axis, the four possible NV center orientations will all experience the same B-field projection, as seen in Fig. 5.1. This results in one single detected absorption band each for the $|-1\rangle \rightarrow |0\rangle$ and $|0\rangle \rightarrow |1\rangle$ transitions, see Fig 5.2. However, due to the relatively large and anisotropic D-tensor of NV ($D_{zz} \approx 2.8$GHz, $D_{xx}, D_{yy} \approx 0$), the degeneracy of the transition frequencies is quickly lifted by applying a small misalignment angle to the sample. This essentially creates four separate NV center species, labeled NV1-NV4, whose transitions frequencies can be spread out over a range of >1 GHz for angle differences of only ($< 5°$). The misalignment is defined by two angles, θ and ϕ, each of which is associated with one pair of NV species. This configuration is depicted in Fig. 5.1.

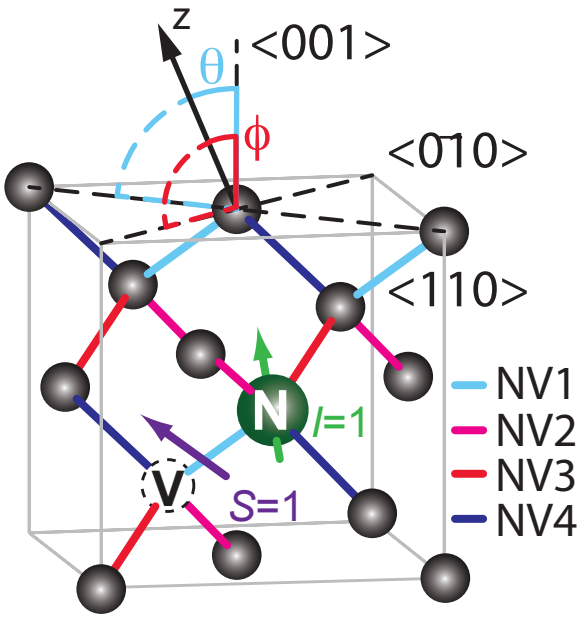

Figure 5.1: Diamond lattice misalignment. The lab frame $z-$axis is indicated with the black solid arrow. The orientation of the diamond corresponds to that of Sample #2, with the corresponding crystal frame axes labeled with dotted lines. The crystal $\langle 001 \rangle$ axis is misaligned from the lab frame z-axis (and thus the static B-field). This misalignment is defined by two angles, θ and ϕ, which correspond to the tilts of the magnetic field along the $\langle 110 \rangle$ and $\langle 0\bar{1}0 \rangle$ axes, respectively.

Like NV centers, R5 centers are also spin-1 and have an anisotropic zero-field splitting. However, the degree of anisotropy is much less severe than that of NVs and thus the R5s are less sensitive to a small misalignment of the B-field. For the typical angles that are used for misalignment ($\theta < 5^\circ$), the R5 transitions only shift by $\sim 1 - 5$ MHz. In the [001] orientation it can also be calculated that the lower $|-1\rangle \rightarrow |0\rangle$ transition has a smaller energy than that of the $|0\rangle \rightarrow |1\rangle$ transition for a given B-field value. By applying a specific misalignment of the B-field, we can engineer the system so that the upper transition of one particular NV species overlaps their frequencies with the lower transition of R5. The systems can then exchange energy through spin flip-flops, increasing the number of relaxation channels available for the NV center relaxation and thus rapidly accelerating the relaxation time. Given that the decay of the NVs to the ground state is on the order of several hours, this means that spins accumulate in the $m_s = 0$ state and population inversion is achieved.

5.1.2 B-field tilt and spin transitions

We first conduct a test with a cw-microwave probe similar to the experiments performed in Ch. 4. In contrast to early experiments, this time we make use of a vector magnet which allows for control of the B-field along all three axes. This will allow us to align the field relative to the crystal axis at any angle of our choosing. As seen in the previous chapter, the diamond [001] axis was misaligned with respect to the z-axis of the lab frame

B-field by about 4.5 deg, causing the NV ESR transition of Sample #2 to be split into four distinct lines, one of which overlapped with P1B (refer to Fig. 1.9). As a test of our vector magnet, we will compensate for this misalignment by adjusting the B-field values along $x-$ and $y-$, which should align all of the NV centers into one single transition. The reflected power data can be seen in Fig. 5.2.

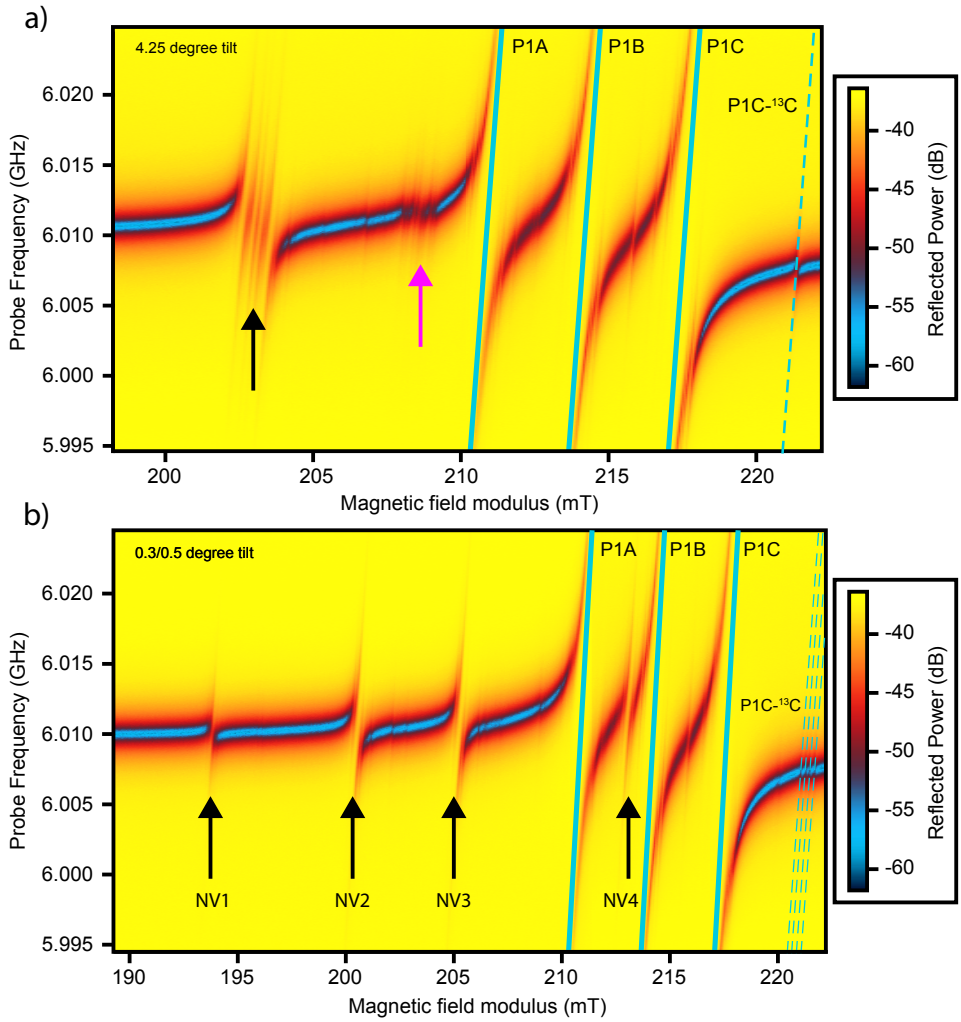

Figure 5.2: Reflected power spectrum of sample #2 at 10mK under B-field tilt. a) Spectrum with B_0 tilted at an angle of 4.25° about the lab frame y-axis. The P1 centers can be seen in cyan lines, with one ^{13}C satellite near 223 mT (dashed cyan line). This tilt nearly compensates for the natural misalignment of the NV centers, whose lower transition ($m_s = -1 \rightarrow 0$) is seen around 203 mT (black arrow). The corresponding upper transitions ($m_s = 0 \rightarrow 1$) can still be detected at 209 mT (pink arrow), indicating that some population remains in the $m_s = 0$ state at the time of measurement. b) Spectrum with much smaller compensation angles of 0.3° and 0.5° along the x and y axis. Four distinct NV transitions are seen (black arrows), including one that crosses over P1A. The P1 centers have remained at the same field values, although the tilting effect can also be seen on ^{13}C satellite at 221.5 mT (dashed cyan lines). The upper transitions of the NV centers are no longer detected in this configuration, because the measurement was performed sufficiently long time after the cool down to 10 mK.

From Fig 5.2 it can be clearly seen that the NV centers are incredibly responsive to even small shifts of the magnetic field, making it easy to tune the transitions where they are needed. Using the information about the R5 tensor obtained in Ch. 4, we construct a

theoretical model of the transition frequencies as a function of magnetic field in order to determine the approximate frequency difference between the transitions of R5 and NV. Using the known spin parameters of NV and R5, we generate the transition spectrum seen in Fig. 5.3.

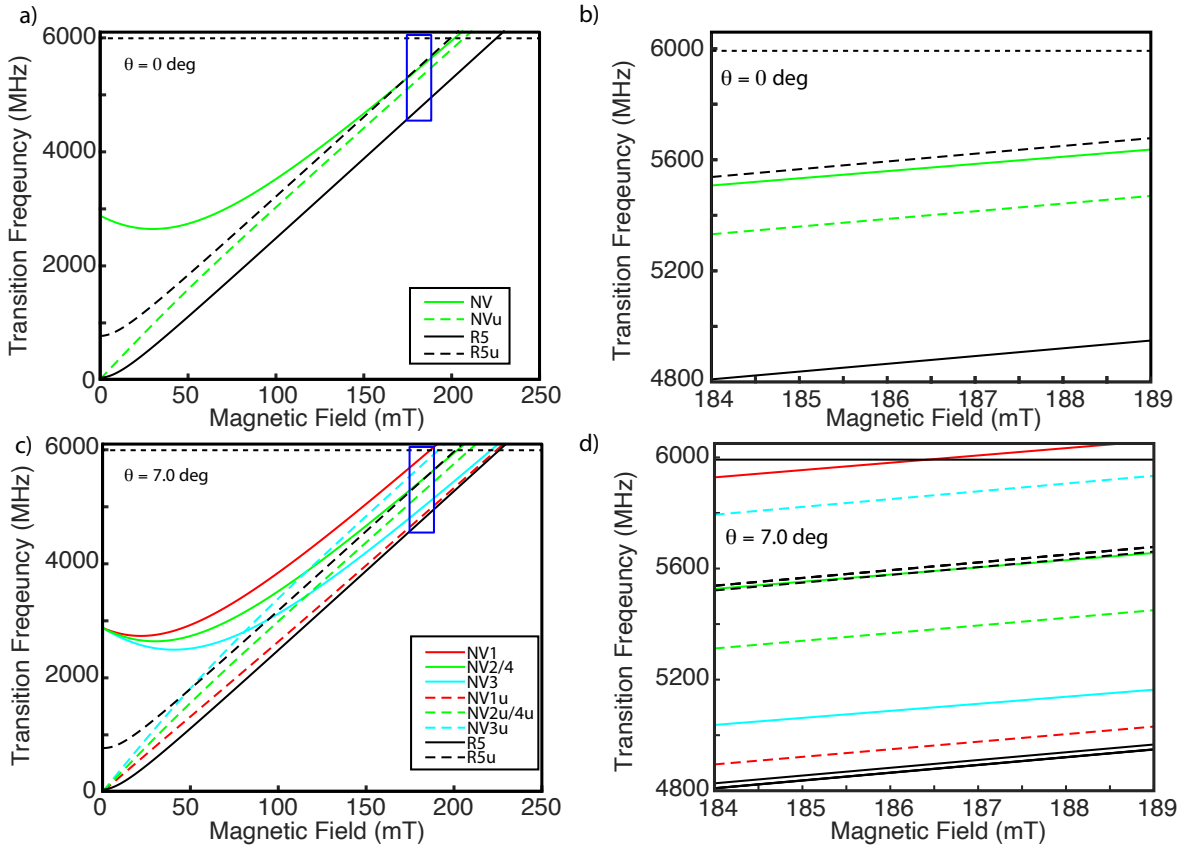

Figure 5.3: Control of the transition frequencies of R5 and NV. a) Transition frequencies of NV and R5 when there is no misalignment. In this case the upper NV transition (NVu) and lower R5 transition (R5) are far detuned from each other. b). Zoom in on the transition frequency map. R5 and NVu are separated by almost 1 GHz, as such any interaction between the two spin species is likely to be extremely weak. c) Transition frequencies for a misalignment angle of $\theta = 7°$. The green lines represent the pair of NV alignments (NV2/NV4) whose axes are orthogonal to the tilt angle and thus do not shift from the values depicted in a). The red (NV1) and cyan (NV3) lines represent the pair of NV alignments whose degeneracy is broken by the misalignment, which results in one being shifted to higher frequency (NV1) and one to lower frequency (NV3). d) Zoom in on the blue region indicated in c). The R5 centers have negligibly shifted, and the upper transition (NV1u) has become nearly resonant with the lower R5 transition. The quick relaxation time of the R5 centers can act as an extra decay channel for nearby NV transitions, accelerating their relaxation.

5.1.3 The diffusion model

Since the number of R5s is a few orders of magnitude lower than the NVs, they do not constitute a thermal bath in the traditional sense. Thus, we have developed the following model for diffusion of the spin flip-flops throughout the system.

The primitive cell of diamond, consisting of 8 atoms, has a volume of 45.37 Å^3. This corresponds to 10^4 carbon atoms per 56.7 nm^3. Impurity concentrations are usually given in terms of parts-per-million (ppm), which is the ratio of the number of impurity atoms to the number of carbon atoms. The concentration of NV centers in our sample is roughly 2 ppm, which corresponds to one NV center per 5670 nm^3. Likewise, we estimate the concentration of R5 centers in our sample to be 1 part-per-billion (ppb), corresponding to one R5 center per 5.67×10^6 nm^3. Thus we can imagine the average NV and R5 centers occupying spheres of radii 11 nm and 110 nm, respectively, to represent the average separation between atoms of the same type, as seen in Fig. 5.4.

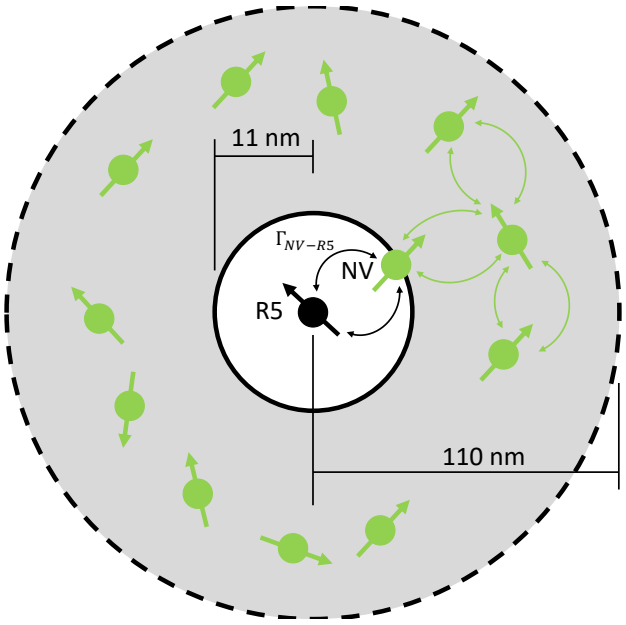

Figure 5.4: A phenomenological model of the NV-R5 interaction within the diamond lattice. Each R5 center occupies a "bubble" of radius 110 nm in which no other R5s reside. Approximately 1000 NV centers are located within this same bubble, based on the known concentration of NV centers. An R5 center, however, will primarily interact via spin flip-flops with its nearest-neighbor NV center, located ∼11 nm from it. These interactions will then diffuse throughout the rest of the bubble via NV-NV interactions. Despite being much lower in concentration, the R5 centers can still act as a spin bath in this way. This is taken into account by the effective spin flip-flop rate Γ_{flip}.

Within each R5 sphere there are roughly 1000 NV centers, however the R5 center cannot interact with all of these centers efficiently as the spin-spin interaction decreases with distance, $\Gamma_{flip} \propto 1/r^3$. At a distance of 11 nm a given the spin-spin interaction rate will decrease to 1/1000 at 110 nm. Given this picture, we make the following assumptions

about our sample:

- The interaction between the R5 centers, separated by an average distance of 110 nm, can be ignored.
- On average, an R5 center will have one NV center within an 11-nm "bubble" surrounding it, and these two spins will interact the most efficiently
- The NV centers, separated by an average distance of 11 nm, will interact with each other at a rate roughly equal to the R5-NV rate.
- Energy transferred from R5 diffuses to further NV centers via resonant NV-NV flip-flops.
- Thus, the interaction of R5 with further NV centers can be represented by an "effective" spin flip-flop rate. We initially estimate this rate at 10 Hz.

With this information we can construct the interaction model for the R5/NV centers. We first establish 6 energy levels corresponding the energy levels of R5 and NV at a given field modulus and angle, whose populations will be monitored as a function of time. These spin energy levels, the interactions between them, and the lattice relaxations are represented by the diagram in Fig. 5.5.

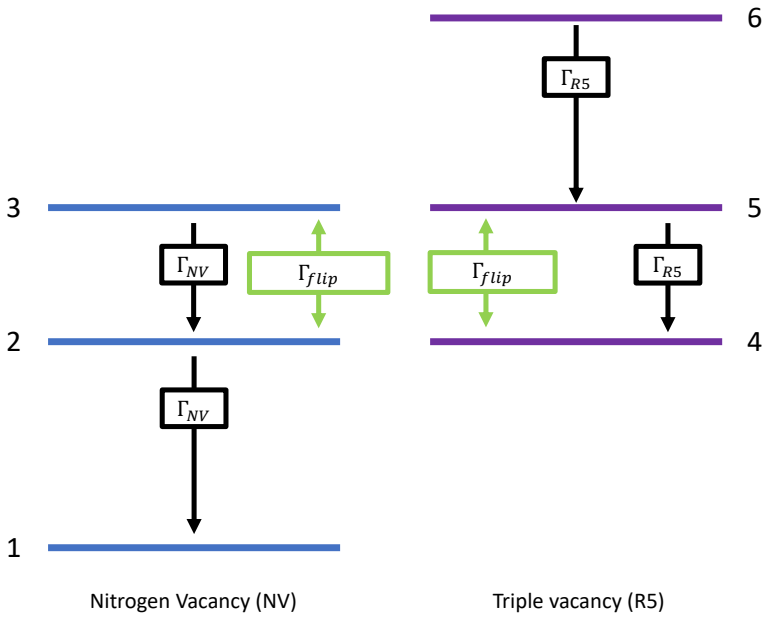

Figure 5.5: The spin flip-flop interaction model for NV/R5. The three spin states of NV (R5) are labeled 1-3 (4-6). The B-field has been tuned in such a way that the transition NV_{2-3} is resonant with the transition $R5_{4-5}$. Energy is exchanged between these four levels at the rate Γ_{flip}. In addition, spins in each upper level relax to the lower levels at the rates Γ_{NV} and Γ_{R5}, respectively. If there is a large asymmetry in the relaxation rates, a population inversion should manifest on the transition NV_{1-2}.

5.1.4 Rate Equations

Using the interaction model, we now wish to establish a model for describing the time evolution of the system after it is quickly brought from 4 K to 10 mK. We assume the B-field is fixed at $B_0 = 186.5\text{mT}$, which in our case is where the $-1 \rightarrow 0$ spin transition of NV1 is equal to the resonator frequency in the orientation ($\theta = 4.5°$), see Fig 5.3d. We construct a system of differential equations to model the complex relations between the levels of R5 and the NVs. The equations are written

$$\begin{aligned}
\frac{dn_1}{dt} &= n_2\Gamma_{NV}, \\
\frac{dn_2}{dt} &= -n_2\Gamma_{NV} + n_3\Gamma_{NV} - (n_2n_5 - n_3n_4)\Gamma_{flip}, \\
\frac{dn_3}{dt} &= -n_3\Gamma_{NV} + (n_2n_5 - n_3n_4)\Gamma_{flip}, \\
\frac{dn_4}{dt} &= n_5\Gamma_{R5} + (n_2n_5 - n_3n_4)\Gamma_{flip}, \\
\frac{dn_5}{dt} &= -n_5\Gamma_{R5} + n_6\Gamma_{R5} - (n_2n_5 - n_3n_4)\Gamma_{,} \\
\frac{dn_6}{dt} &= -n_6\Gamma_{R5}.
\end{aligned} \tag{5.1}$$

In order to predict the behavior of the system, timescales for spin interactions and relaxation are needed, as well as initial conditions. We assume that the spin system is initially at 4 K, which functions as the hot bath by distributing the spins across the three energy levels according to the Boltzmann distribution. We assume 6 GHz for the Zeeman splitting of the energy levels, which is the resonator frequency for these experiments. This gives the initial conditions as

$$\begin{aligned}
n_{1,i} = n_{4,i} &= 0.358, \\
n_{2,i} = n_{5,i} &= 0.333, \\
n_{3,i} = n_{6,i} &= 0.309.
\end{aligned}$$

At 10 mK, the cold bath temperature, the spins are overwhelmingly populating the ground state, $n_{1,i} = n_{4,i} \approx 0.358$. There is no active pump in this arrangement so no such terms need to be added to the rate equations. The rates used for the relaxation and spin flip-flops are

$$\begin{aligned}
\Gamma_{NV} &\approx 3 \times 10^{-5}\,\text{Hz}, \\
\Gamma_{R5} &\approx 50\,\text{Hz}, \\
\Gamma_{flip} &\approx 10\,\text{Hz}.
\end{aligned}$$

The results are plotted in Figure 5.6, showing the behavior of each of the subsystems as a function of time. The initial value of Γ_{NV} is based on measurements in Ch. 4. The actual values Γ_{R5} and Γ_{flip} are not well known and are initially guessed based on the conditions required for the thermal maser to populate, according to our current best

understanding. They will be refined when compared to the data. The effect is primarily due to the asymmetric effect of the spin flip-flops; the R5s relax much faster than the NVs and thus overwhelmingly populate the ground state. When an R5 center undergoes a flip-flop with NV it is excited to level 5. Because of the fast relaxation of R5, the centers can occasionally relax back to 4 again before another flip-flop interaction can take place. It is this fast relaxation of R5s and the efficient transfer of energy between the R5s and NVs that makes the inversion possible. Therefore, the conditions required for the effect to take place are 1) $\Gamma_{R5}, \Gamma_{flip} \gg \Gamma_{NV}$, and $\Gamma_{flip} \gtrsim \Gamma_{R5}$. If the flip-flop rate is too weak or the relaxation of R5s too long, the entire system relaxes to the ground state before any inversion can be generated. We notice in Fig. 5.6c, representing the behavior of the NV centers, that level 2 ($m_s = 0$) exceeds the population in level 1 ($m_s = -1$), meaning that the system achieves population inversion. The total lifetime of the inversion is governed by the relaxation of the NV centers from the middle to the ground state. No more spin flip-flops are possible from the $m_s = -1$ state of the NV centers and once the spins reach this state they must be "woken up" by warming the system to 4 K once again.

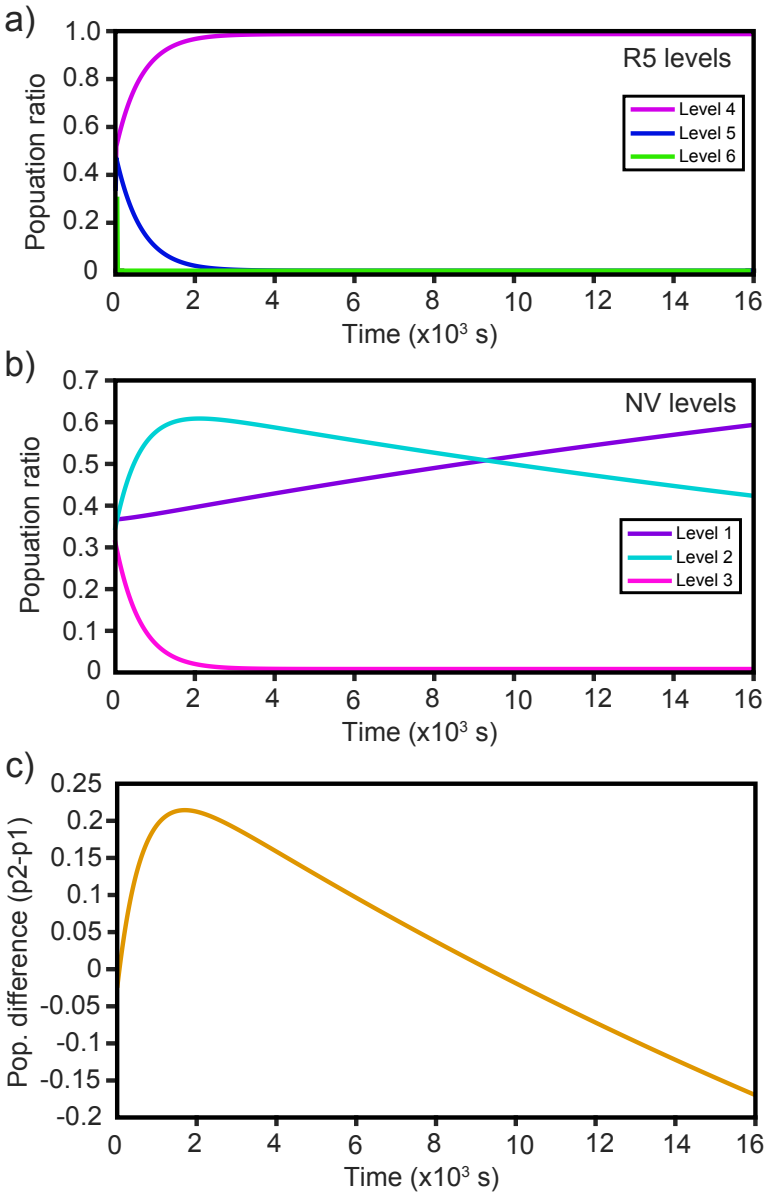

Figure 5.6: Rate equation simulation results for NV-R5. a) Projection of the populations of the R5 energy levels as a function of time. The levels 4-6 correspond to $m_s = -1$, 0, 1 spin states, respectively. The top level (6) depopulates almost immediately, whereas the middle level (5) relaxes more slowly, allowing the population in NV centers to build up via spin flip-flops. Eventually the spins all accumulate in the ground state (4) and the system remains there. b) Projection of the populations of the NV energy levels as a function of time. The levels 1-3 correspond to $m_s = -1$, 0, 1 spin states. The spins in the top level (3) relaxes to the middle NV level (2) at a much faster rate than those in (2) to the ground state (1). This means that the population in level (2) grows in time, reaching a peak around 2000 seconds before beginning to relax into the ground state. c) The population difference between NV levels 2 and 1 as a function of time. The population difference becomes positive shortly after initialization, indicating that the system has reached an inverted state. The population difference slowly becomes negative again after a long time, as the system slowly relaxes back to equilibrium.

5.2 Experimental detection of a thermal maser

5.2.1 Initial lifetime measurement

Using the theoretical results of the thermal maser we can implement an experimental procedure for detecting and measuring the population inversion. The diamond (Sample #2) is once again placed inside the resonator cavity and then inside the dilution fridge and cooled to <20 mK. In order to be able to extract the spin parameters from the reflection data, the cavity parameters were first determined at $B_0 = 0$ using a VNA reflection trace. The next step was to locate the resonance of the lowest-field NV transition ("NV1" in Fig. 5.3), which serves as point where the measurement takes place. Keeping the B-field magnitude and angle fixed, the mixing chamber (MXC) heater of the dilution fridge was supplied with current to raise the temperature of the spins to 4.5 K. At this temperature, the T_1 of the spins is much faster, around 1 min. The heater was kept on for 15 minutes to ensure that all of the spins are in thermal equilibrium (i.e. the Boltzmann distribution). After this waiting time the heater was shut off and the MXC temperature returned to <20 mK within one hour. For more technical details, see B. At this point a probe frequency was applied to the cavity from the VNA, which monitored the behavior of the reflected power in time. Results of this procedure are shown in Fig. 5.7a. The behavior of the system closely follows the general pattern predicted by the model in Fig. 5.6. A short time after beginning the measurement, the reflected power from the resonator is amplified and eventually surpasses the background of the resonator. By using the known cavity parameters we can deconvolute the spins and cavity and calculate the function $K(\omega)$ (see the procedure in Sec. 4.3.4),

$$K(\omega) = \omega - \omega_r + \frac{i}{2}\left(\kappa_L + \kappa_1 \frac{R(\omega) - 1}{R(\omega) + 1}\right). \tag{5.2}$$

By examining the various profiles of $\mathrm{Im}[K(\omega)]$ plotted in Fig. 5.7b-d, we can make a few conclusions about the behavior of the spins. The first is that the system achieves population inversion, with an incredibly long lifetime of the inverted spins. This is governed almost entirely by the NV spin lattice relaxation time. In fact, such is the length of the time that spins remain inverted even after > 4 hours of measurement time. To our knowledge, this is the longest-lived and strongest inversion ever seen in thermal maser setup (*cf.* Refs. [72]-[74]).

The second is the fact that the spins achieve inversion very quickly, already showing a negative value of $\mathrm{Im}[K(\omega)]$ by the time that the measurement is started. The rise time of the inversion is governed by the relaxation time T_1 of the R5 centers, which we estimate to be around 100 ms based on the data in Fig. 5.7d. Based on this, it would seem sensible that the start of the measurement, i.e. $t = 0$, be moved to the point when the heater is shut off. This solution, too, is not without its problems. We know that the R5 centers begin to relax immediately, during the re-condensation and cooldown of the MXC, and the lattice relaxation time T_1 itself has a strong temperature dependency. Starting at the instant the heater is stopped would present a difficult situation for our model, which assumes a constant T_1 throughout. The nature of the recondensation procedure of the ^{3}He/^{4}He mixture may also mean that the temperature of the MXC and spin ensemble do not follow any sort of predictable pattern and can be slightly different each time. Our

solution to this problem, implemented in the next section, is to monitor the temperature of the MXC and begin the measurement immediately upon reaching a certain value of T (e.g. 50 mK).

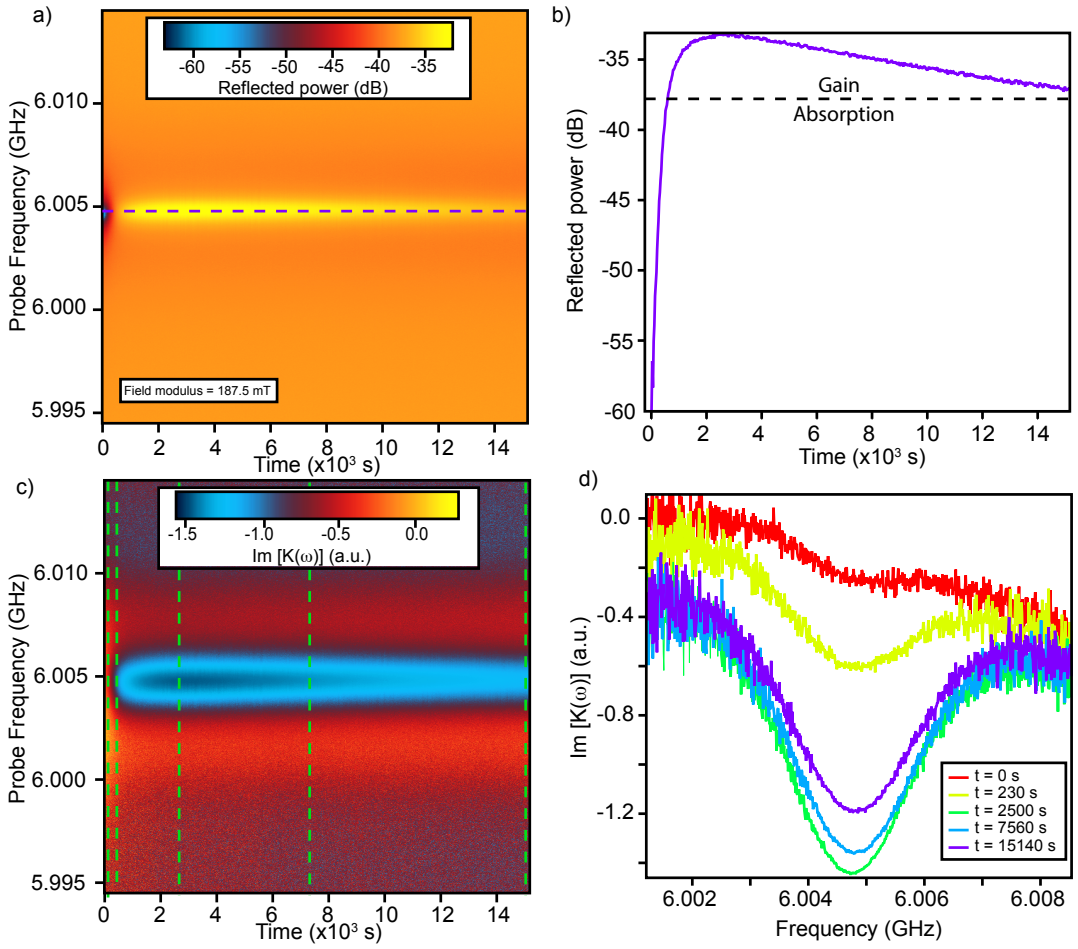

Figure 5.7: The long-lived thermal maser in diamond. a) Time evolution of the reflected power spectrum as a function of probe frequency, after warming the sample to 4 K and cooling back to <20 mK. The field modulus is set so that the anticipated NV transition frequency is resonant with the cavity ($\omega_s = \omega_r$). After a brief initial absorption period, the system shows amplification of the microwave probe signal, peaking around 1 hour and eventually returning to equilibrium after a lengthy relaxation period. The central spin frequency is noted with a purple dashed line. b) Profile of the reflected power at the center frequency 6.0046 GHz over time (purple dashed line in (a)). The area where the reflected power exceeds the background is indicated by the black dashed line. c) Im$[K(\omega)]$ function extracted from the raw data by deconvoluting the resonator from the spin ensemble. The spin system is clearly already inverted ($K(\omega) < 0$) upon the start of the measurement, and the inversion persists throughout the entire measurement. Positions of frequency profiles are indicated with vertical green dashed lines. d) Frequency profiles of Im$[K(\omega)]$ at various times during the measurement. At $t = 0$ the function is already slightly inverted, and the function becomes more negative until $\approx$ 2500 s, where is begin to return toward equilibrium. The long lifetime of the inversion indicates a bottleneck in the middle level of NV, indicating high asymmetry in the relaxation times.

5.2.2 Optimization of the thermal maser

With the process for creating an inverted ensemble established, we set about characterizing and optimizing the maser performance. The procedure described above is repeated over a range of misalignment angles. Using the same MATLAB program that generated the plots of Fig. 5.5, we calculate the detuning between R5 and the upper NV transition as a function of the misalignment angle. Using this, we will identify the optimum angle for operation and provide evidence that NV-R5 spin flip-flops are indeed the primary cause of the population inversion.

As mentioned above, the measurement process is started at the same temperature for each iteration ($T_0 = 50$ mK), over a range of misalignment angles from $\theta = 4.5 - 10°$. One such example of inversion is seen in Fig. 5.8a, which follows the same pattern established in previous measurements. At each point, the frequency trace at the maximum gain was fitted using the expression for the imaginary portion of $K(\omega)$, as derived in Ch. 3,

$$\begin{aligned} K(\omega) &= \frac{g_{ens,eff}^2}{\omega - \omega_s - i\Gamma} \\ \mathrm{Im}[K(\omega)] &= \frac{\Delta N g^2 \Gamma}{(\omega - \omega_s)^2 + \Gamma^2}. \end{aligned} \tag{5.3}$$

From this we can determine that the linewidth of the NV1 subensemble is $\Gamma = 2.2 \pm 0.4$ MHz, which is consistent with the value derived from the absorption measurements in Ch. 4. The population difference between the NV levels 2 and 1, in terms of number of spins, was obtained by integrating the region between the cyan dashed lines of 5.8a. In order to make this quantity into the population difference ratio, the absolute number of spins had to be determined. Given the incredibly long lifetime of NV1, we instead deduced the number of spins from another nearby NV transition (NV3), which at the time of measurement was fully relaxed. From this, we could calculate the ratio $p_2 - p_1$ as depicted in 5.8c. Transforming the data in this way allowed us to fit our model to the data using a least-squares method. The lattice relaxation rates were first determined to be $\Gamma_{NV} = 0.5 \times 10^{-6}$ Hz and $\Gamma_{R5} = 10$ Hz, these values were kept constant for each fit, with initially only Γ_{flip} as a free parameter. However, it was quickly discovered that the initial population in the ground state, $p_{1,i}$, was a critically important parameter that also needed to be determined for each data set. As discussed earlier, the nature of the experimental procedure results in poor control over the initial conditions of the spins. The value $p_{1,i}$ correlates strongly with the maximum inversion ratio achieved by the spins during a given experiment, more so than the flip-flop rate Γ_{flip}. However, it was found that Γ_{flip} does indeed have a dependence on the detuning between NV and R5. Using the values of D_{xx}, D_{yy}, and D_{zz} calculated in Ch. 4, it was found that the flip-flop rate reaches its maximum reasonably close to the point where the detuning is zero (see Fig. 5.8d. The flip-flop rate drops off as the detuning is increased, and tilting to an angle smaller than $\theta = 4.5$ results in no inversion of the spin ensemble at all.

5.2.3 Towards a self-oscillating thermal maser

Lastly, we want to compare the value ΔN extracted from the data to the masing threshold ΔN_{th} to see if the thermal maser is capable of reaching the self-oscillation regime.

Recalling Eq. 3.131 and inserting our values calculated from Fig. 5.8b, we get

$$\begin{aligned}\Delta N_{th} &= \frac{(2\pi \times 6.0046 \times 10^9\,\mathrm{Hz})^3 (11.5\,\mathrm{mm}^3)(2\pi \times 2.24 \times 10^6\,\mathrm{Hz})}{\pi^2 c^3 (5 \times 10^{-13}\,\mathrm{Hz})(1300)} \\ &= 4.9 \times 10^{13}\,\mathrm{spins}.\end{aligned} \tag{5.4}$$

For these parameters, the observed amplifier behavior in this cavity configuration falls just short of the maser threshold. This is consistent with our own observations, as we have not yet detected any emission from the cavity-spin system in the absence of the applied probe tone. Future experiments on this system should be repeated with a higher-Q cavity, or a spin ensemble with a narrower linewidth. If the other parameters are preserved as they are, Q_{tot} need only be increased to ≈ 1600 to push the spins across the masing threshold. This seems easily within reach even with the current resonator geometry, for example, by improving the contact at the seam between the two resonator halves.

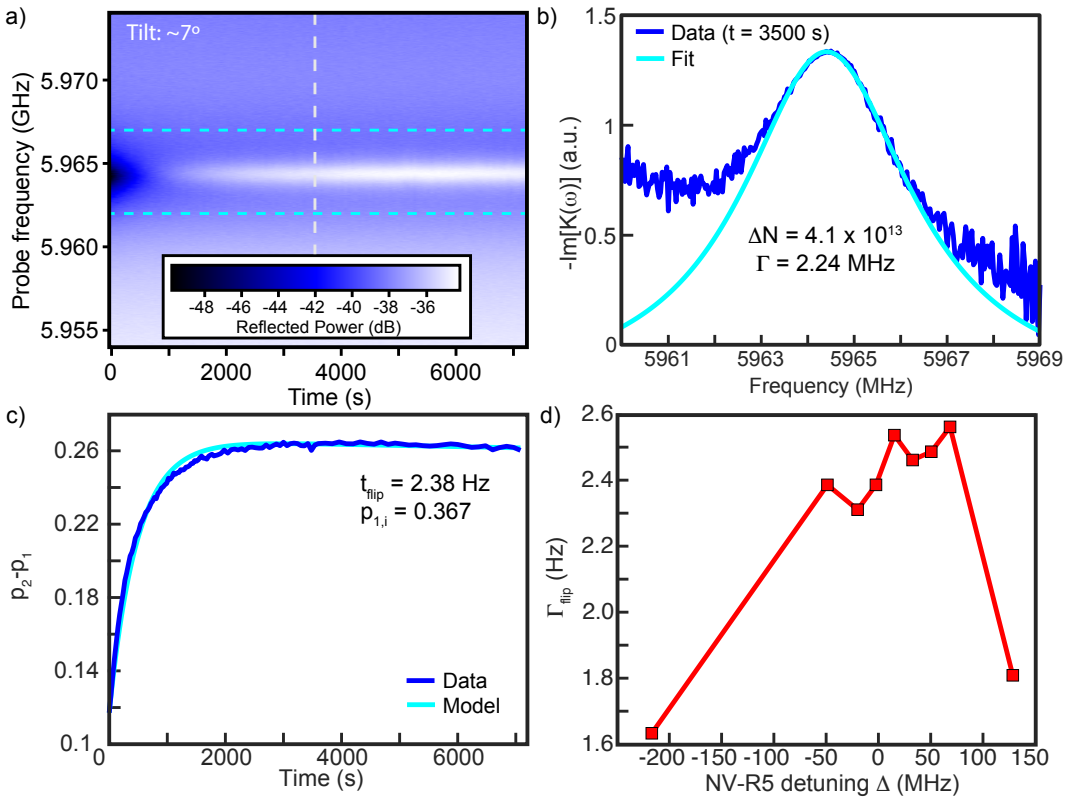

Figure 5.8: Optimizing the thermal maser. a) Time evolution of the reflected microwave signal as a function of probe frequency, after warming the sample to 4.5 K and cooling, starting measurement once the mixing chamber temperature reaches 50 mK. The B-field is tiled $\approx 7°$ about the y-axis, and the field modulus is set so that NV transition frequency is resonant with the cavity (determined in a prior measurement). The frequency profile at the approximate maximum gain is indicated with a dashed white line. The bandwidth used in (c) is labeled with cyan dashed lines. b) The values of $\mathrm{Im}[K(\omega)]$ as a function of frequency at maximum gain, converted from the raw data in (a). The profile is fit with a Lorentzian, from which the spin linewidth (2.24 MHz) and number of inverted spins ΔN are extracted (see Eq. 5.3) in main text). c) The population difference ratio $p_2 - p_1$, derived from integration of $\mathrm{Im}[K(\omega)]$, as a function of time, with the accompanying model. The model fits the data well and from it the spin flip-flop rate Γ_{flip} and initial population p_1 are extracted. d) Plot of Γ_{flip} as a function of the detuning between the upper NV transition and R5 center, which itself is proportional to the component of the B-field along x. The maximum spin flip-flop rate occurs close to $\Delta \approx 0$, showing that R5 centers are likely responsible for the behavior of the thermal maser. The flip-flop rate quickly drops as the angle detuning is increased.

5.3 Summary

In this section we observed the thermally induced population inversion of an ensemble of NV centers coupled to a resonant cavity, manifested by the amplification of a microwave

probe tone applied to the cavity. The pump power was supplied completely by heat energy trapped within the system as it cooled from 4 K to <20 mK, demonstrating what is known as a "thermal maser," a type of heat engine that converts thermal energy to microwave photon energy. This is achieved through spin flip-flop interactions with what were determined to be R5 centers also present in the spin ensembles, which accelerate the relaxation from the upper NV level to the middle level. This creates a long-lived inverted state that persists on a timescale equal to the NV lattice relaxation time (T_1). Although no self-oscillating coherent signal has been detected at the time of writing, our quantitative estimation predicts that such conditions should be achievable using an improved resonator and spin ensemble.

Chapter 6

A spin-based microwave amplifier

6.1 Generating inversion in P1 centers

In Chs. 1 and 2 we discussed the electronic structure of the substitutional nitrogen (P1) center in diamond, as well as the mechanism of the four-spin, energy-conserving cross-relaxation process between the central P1 transition (P1B) and its two satellites (P1A/P1C). This mechanism was first observed in Ref. [38], and it was noted that under certain conditions inversion could be achieved on one of the satellites. Specifically, it required that the lattice relaxation times of P1A and P1C be asymmetric, which could be simulated by using a rate equation model [38]. The authors attributed this asymmetry to spin flip-flops with other defects in the diamond, in a manner similar to what we have seen with the NV thermal maser. In Ch. 4, we have determined via time-domain spectroscopy that P1C does, in fact, relax faster than P1A and thus we should meet the conditions required to generate inversion on P1A.

The mechanism by which cross-relaxation and spin flip-flops can generate inversion on P1A is illustrated in Fig. 6.1. Under normal circumstances, a pump signal applied to the central transition will saturate all of the satellites via the cross-relaxation mechanism. If another spin defect (most likely a vacancy cluster) is resonant with the P1 satellite, a second decay channel opens for the P1 center and the lattice relaxation time is accelerated. This allows the central transition to continue to be pumped without saturating P1C, which will eventually result in the generation of an inverted population on P1A. Using this mechanism, it may be possible to generate a continuous maser amplifier or self-oscillating maser.

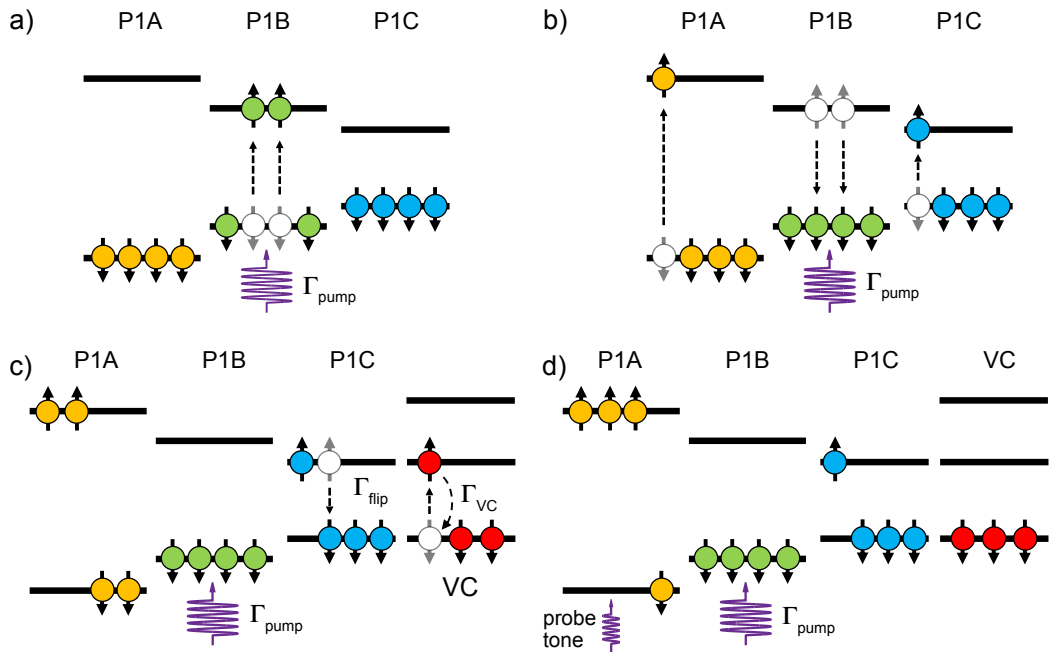

Figure 6.1: Inversion of P1 satellite transition. a) At a given magnetic field, the main P1 transition (P1B, green) is flanked by two hyperfine satellites equidistant in frequency space: a higher-energy transition (P1A, yellow) and a lower-energy transition (P1C, blue). A microwave pump tone is applied to the center transition, which excites the spins at a rate Γ_{pump}. b) The P1 centers undergo a four-spin, energy-conserving cross relaxation process in which two spins on the center transition exchange energy with a single spin on each satellite, occurring at a rate Γ_{cr}. If Γ_{pump} is continuously applied, then this will eventually result in the saturation of all three satellites. c) The same arrangement, but with a vacancy cluster (VC) whose lower transition is co-resonant with P1C. P1C and VC center exchange spin flip-flops at a rate Γ_{flip}. The fast relaxation of the VC center (Γ_{flip}) ensures that this process is asymmetric, resulting in accelerated relaxation of the P1C satellite spins. d) Under these circumstances, P1C does not become saturated. This allows the population in the higher energy level of P1A satellite to build up via cross-relaxation, eventually resulting in population inversion on P1A.

6.2 Experimental observation

6.2.1 Maser amplifier

For this experiment, we perform cw-microwave spectroscopy on sample #2 by measuring the reflected power from the cavity under a continuous pump applied to P1B and a probe signal applied to P1A. See App. B, Fig. B.2 for the electronic and wiring diagrams of the dilution refrigerator.

Firstly, the reflection profile was measured at zero magnetic field in order to determine the resonator background and line profile. By fitting the bare cavity reflection data, we obtain the following values: $\omega_r = 6.383\,\mathrm{GHz}$, $\kappa_{int} = 2.67\,\mathrm{MHz}$, $\kappa_{ext} = 9.64\,\mathrm{MHz}$. In

this case, the external coupling (linewidth) was intentionally made larger so that the spins could be pumped off-resonantly. Knowing these parameters, it is now possible to deconvolute the spin profile from the resonator.

The second step is to estimate the total number of spins on P1A by measuring the absorption profile on resonance when the spins are in thermal equilibrium at 20 mK. We use the cavity deconvolution procedure (see Ch. 4) to extract the following information about the spin ensemble $\Gamma = 3.16\,\mathrm{MHz}$, $\Delta N_{eq} = 2 \times 10^{15}$. This value of ΔN_{eq} is consistent with the value of g_{ens} determined in Ch. 4 for sample #2, and as a result we can safely assume that the spins are indeed in thermal equilibrium. This value provides a baseline so that the inversion ratio can be accurately determined.

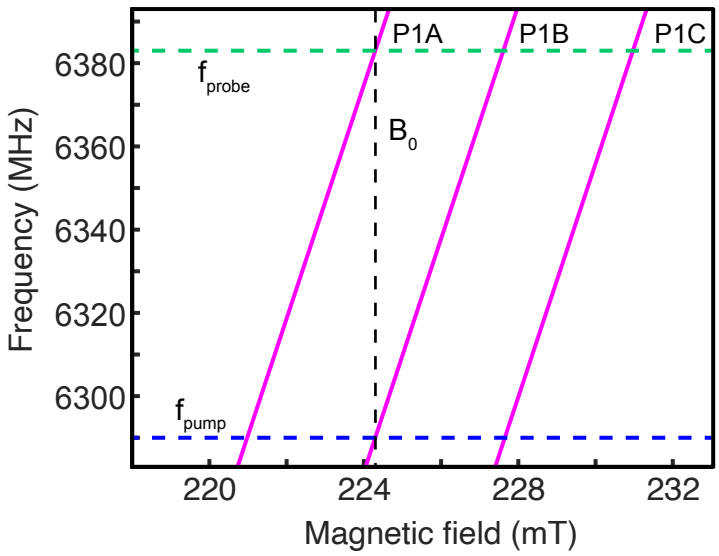

Figure 6.2: Pumping scheme for the P1 cw maser. The transition frequencies as a function of B-field of the three major P1 transitions are plotted with pink lines. The static B-field is set at ≈ 224 mT (black dashed line), so that the P1A transition is resonant with the probe (and cavity) frequency (green dashed line). The pump frequency is set at 6.29 GHz so that it is resonant with the P1B transition.

The field magnitude is kept so that the P1A spin transition is resonant with the cavity, while the pump signal is applied at a frequency $f_{pump} = 6.29\,\mathrm{GHz}$ and power $P_{in} = -26$ dBm at the resonator, approximately 94 MHz away from the resonator frequency. The pump-probe scheme is depicted in Fig. 6.2. The variable attenuator and phase shifter on the cancellation line are calibrated so that the pump signal reflected from the cavity is neutralized and does not enter the return line. The results can be seen in Fig. 6.3. At the time of the initial application of the pump signal, the spins of P1A are close to their equilibrium state ($\mathrm{Im}[K(\omega) > 0]$), but slowly begin to saturate over time. This process is limited by the cross-relaxation time of the P1 centers ($\sim 10\,\mathrm{ms}$). After a lengthy period of pumping ($> 10\,\mathrm{min}$), the spins finally begin to show inversion ($\mathrm{Im}[K(\omega)] < 0$). The inversion continues to grow until around 2500 s, where it levels off and provides a steady gain of around 30 dB. By taking the profile of $\mathrm{Im}[K(\omega) > 0]$ at the final timestamp and fitting it to the formula 5.3, we determine the linewidth Γ to be 3.18 MHz. The number

of inverted spins obtained is $\Delta N = 6.6 \times 10^{14}$, which when compared to ΔN_{eq} gives an inversion ratio of around

$$p_{inv} = \frac{6.6 \times 10^{14}}{2.0 \times 10^{15}} \approx 0.33. \tag{6.1}$$

This large inversion should be enough to overcome the maser threshold, but we have also increased the linewidth of the resonator, which pushes the threshold higher. We recalculate the maser threshold ΔN_{th} for this new configuration and compare it to the value of ΔN extracted in Fig. 6.3d above,

$$\begin{aligned} \Delta N_{th} &= \frac{(2\pi \times 6.383 \times 10^{9}\,\mathrm{Hz})^3 (11.5\,\mathrm{mm}^3)(2\pi \times 3.16 \times 10^{6}\,\mathrm{Hz})}{\pi^2 c^3 (5 \times 10^{-13}\,\mathrm{Hz})(520)}, \\ \Delta N_{th} &= 2.1 \times 10^{14}\,\mathrm{spins}. \end{aligned} \tag{6.2}$$

Despite the decrease of the total quality factor, the masing threshold is surpassed in this case due to the large inversion ratio, meaning that the observation of a self-oscillating maser should be possible.

Before we attempt to detect the self-oscillating maser, we want to conduct experiments to determine two key parameters of the amplifier, the first of which is the gain-bandwidth product. This value essentially provides a hard cap on the amount of gain which can be generated by the maser, and comes at the sacrifice of bandwidth. This quantity must be high enough that sufficient gain can be provided to the microwave probe signal, while over a bandwidth at least comparable to the cavity linewidth. The second parameter is the noise temperature, which should be close to the quantum-limited value [66]. This is a necessary condition in order for the spin maser to be useful for quantum information experiments. These quantities are discussed in the following sections.

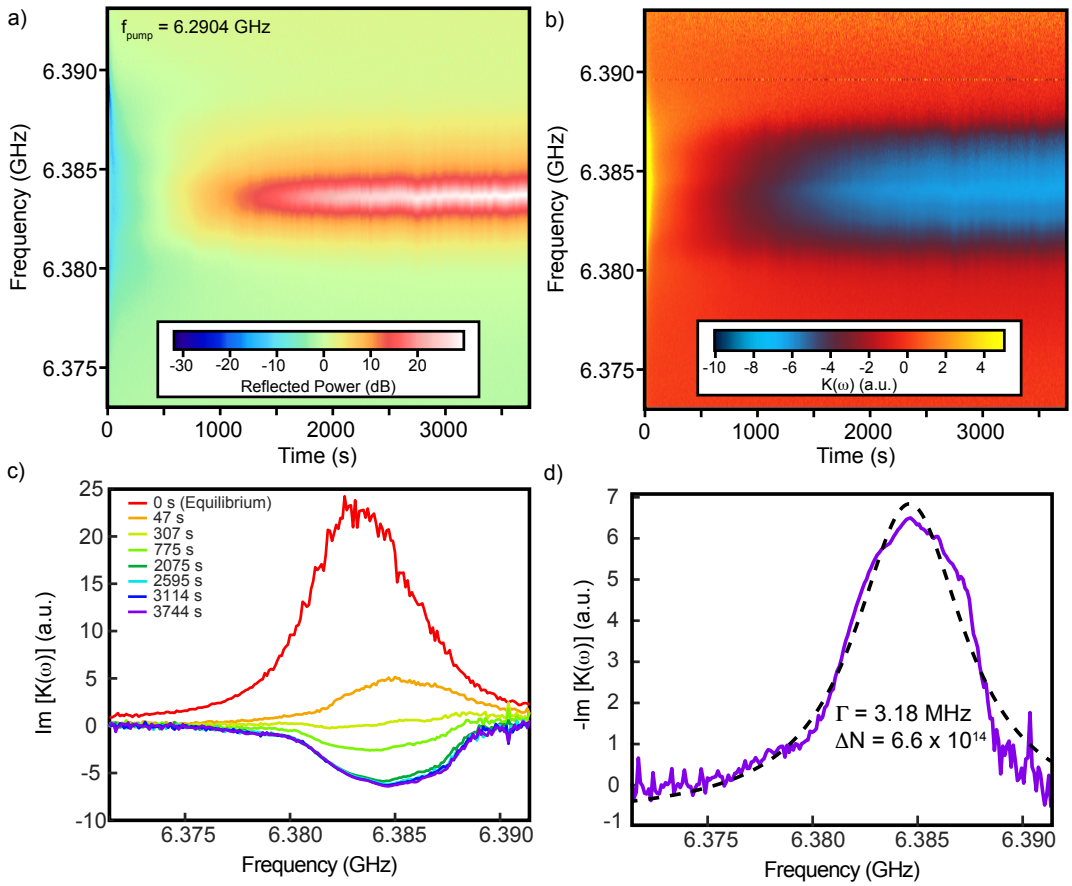

Figure 6.3: Maser amplifier using P1 centers in diamond. a) Raw reflection data as a function of probe frequency in time. The pump frequency is applied at the central P1 transition, ≈ 95 MHz detuned from the cavity. As the pump power is applied, the reflected power grows, and after 15 minutes the signal levels off around 30 dB. b) Spin profile $\mathrm{Im}[K(\omega)]$ obtained by deconvoluting the spins and the cavity. Initially, $\mathrm{Im}[K(\omega)] > 0$, indicating absorption. However, the value of $K(\omega)$ approaches zero as the system is pumped, finally turning negative after ≈ 10 minutes. c) Profiles of $\mathrm{Im}[K(\omega)]$ at various times during the measurement. At $t = 0$ the profile resembles the equilibrium spin profile, which quickly decays as the spins are excited from the lower energy levels. By $t = 307$ s, $\mathrm{Im}[K(\omega)] \approx 0$, corresponding to an equal population in the upper and lower spin state (i.e. saturation). The system reaches an inverted state ($\mathrm{Im}[K(\omega)] < 0$) shortly after, and begins to level off after about 30 minutes of pumping. The profile remains relatively consistent as the pumping is continued for another 30 minutes. Note that the shift in the center spin frequency is due to saturation of the nearby P1B transitions as well as hole burning due to pumping. d) The profile of -$\mathrm{Im}[K(\omega)]$ at $t = 3744$ s. By fitting the spin profile to a Lorentzian, a spin linewidth of 3.18 MHz is obtained. The number of inverted spins, ΔN, is calculated to be 6.6×10^{14}. When compared to the value obtained at equilibrium (see main text), this corresponds to an inversion ratio of $p_{inv} = 0.33$.

Gain-bandwidth product

Using the extracted spin parameters, we calculate the magnetic loss rate κ_{mag} according the formula derived in Ch. 4,

$$\begin{aligned} |\kappa_{mag}| &= \frac{2\Delta N g_{single}^2}{\Gamma} \\ &= \frac{2(6.6 \times 10^{14})(0.19)^2}{3.18 \times 10^6} \\ &= 14.9\,\text{MHz}. \end{aligned} \tag{6.3}$$

The system linewidths $\kappa_{mag}, \kappa_{ext}$, and κ_{int} can be used to calculate the maximum gain and bandwidth of the system. Since κ_{int} is of comparable magnitude to the other two linewidths, we must use the full formula for the gain:

$$\begin{aligned} G &= \left(\frac{\kappa_{int} - \kappa_{ext} - |\kappa_{mag}|}{\kappa_{int} + \kappa_{ext} - |\kappa_{mag}|} \right)^2 \\ &= \left(\frac{2.67\,\text{MHz} - 9.64\,\text{MHz} - 14.9\,\text{MHz}}{2.67\,\text{MHz} + 9.64\,\text{MHz} - 14.9\,\text{MHz}} \right)^2 \\ &= 71.3. \end{aligned} \tag{6.4}$$

A multiplicative factor of 71.3 corresponds to a power gain of 18.53 dB. The corresponding bandwidth is $\Delta f = 2.59$ MHz. This results in a total gain-bandwidth product of

$$\begin{aligned} B\sqrt{G} &= (2.59\,\text{MHz})\sqrt{71.3} \\ &= 21.9\,\text{MHz}. \end{aligned} \tag{6.5}$$

This value is in the range of calculated gain-bandwidth products for spin masers based on ruby [63][64], but about half of a typical JPA [2], and far below that of a Josephson traveling wave parametric amplifier [3]. Nonetheless, the gain-bandwidth value is promising and could be improved further by any of the following:

- increase the magnetic loss rate κ_{mag} by increasing the spin inversion ratio, the cavity coupling, or reducing the spin linewidth,
- increase the cavity coupling linewidth κ_{ext} by moving the capacitive coupling pin closer to the sample,
- reduce the resonator linewidth κ_{int} by improving the contact at the seam, or eliminating the seam altogether (see Ch. 4 for details).

Rate equations

In order to estimate the spin flip-flop rate and vacancy cluster relaxation rate within the P1 maser system, we construct a system of rate equations similar to that of Ch. 5. In addition to spin lattice relaxation times and spin flip-flop rate, the cross relaxation of P1 must also be taken into account, as well as the active pump that is applied to P1B. We

establish eight energy levels - six for P1 and two for VCs - to simulate the maser pumping scheme. We assume that the system always begins in equilibrium, allowing us to ignore the uppermost level of the VCs, as no population exists there. A visualization of these energy levels with all associated rates can be seen in Fig. 6.4a. The equations themselves are

$$\begin{aligned}
\frac{dn_1}{dt} &= n_4\Gamma_{P1A} + (n_2^2 n_4 n_6 - n_5^2 n_1 n_3)\Gamma_{cross}, \\
\frac{dn_2}{dt} &= n_5\Gamma_{P1B} - (n_2 - n_5)\Gamma_{pump} - 2(n_2^2 n_4 n_6 - n_5^2 n_1 n_3)\Gamma_{cross} \\
\frac{dn_3}{dt} &= n_6\Gamma_{P1C} + (n_2^2 n_4 n_6 - n_5^2 n_1 n_3)\Gamma_{cross} + (n_6 n_7 - n_3 n_8)\Gamma_{flip}, \\
\frac{dn_4}{dt} &= -n_4\Gamma_{P1A} - (n_2^2 n_4 n_6 - n_5^2 n_1 n_3)\Gamma_{cross} \\
\frac{dn_5}{dt} &= -n_5\Gamma_{P1B} + (n_2 - n_5)\Gamma_{pump} + 2(n_2^2 n_4 n_6 - n_5^2 n_1 n_3)\Gamma_{cross} \\
\frac{dn_6}{dt} &= -n_6\Gamma_{P1C} - (n_2^2 n_4 n_6 - n_5^2 n_1 n_3)\Gamma_{cross} - (n_6 n_7 - n_3 n_8)\Gamma_{flip} \\
\frac{dn_7}{dt} &= n_8\Gamma_{VC} - (n_6 n_7 - n_3 n_8)\Gamma_{flip} \\
\frac{dn_8}{dt} &= -n_8\Gamma_{VC} + (n_6 n_7 - n_3 n_8)\Gamma_{flip}
\end{aligned} \tag{6.6}$$

For our system, the P1A and P1C relaxation times used will be those directly measured in Ch. 4,

$$\begin{aligned}
\Gamma_{P1A} &= 1/T_1 = 1.45 \times 10^{-3}\,\text{Hz}, \\
\Gamma_{P1C} &= 2.47 \times 10^{-3}\,\text{Hz},
\end{aligned} \tag{6.7}$$

whereas the P1B relaxation rate will be the average of these two values, $\Gamma_{P1B} = 1.9 \times 10^{-3}\,\text{Hz}$. The cross relaxation rate was not measured directly but the value of $T_{cross} = 10\,\text{ms}$ was used from Ref. [38], so that $\Gamma_{cross} = 100\,\text{Hz}$. The pump rate was directly calculated by using the expression for the n-photon Rabi frequency,

$$f_{Rabi} = 2g_{single}\sqrt{\bar{n}}, \tag{6.8}$$

where $\bar{n}$ is the average number of pump photons in the cavity based on the input power and cavity parameters as shown in Eq. 3.28. For a pump power of $-26\,\text{dBm}$, the corresponding Rabi frequency is $\approx 9\,\text{kHz}$, a rate which is much larger than the others in our system. The terms Γ_{flip} and Γ_{VC} were used as fitting parameters. The results are plotted in Fig. 6.4b along with experimental data extracted from Fig. 6.3 for fitting. Values of $\Gamma_{flip} = 5\,\text{Hz}$ and $\Gamma_{VC} = 10\,\text{Hz}$ are extracted from the fit; these are consistent with values determined from a similar fitting in Ch. 5.

For a sufficiently large pumping power, the steady-state value of the inversion is primarily determined by Γ_{flip}, whereas the quick initial response is dominated by Γ_{cross}. However, obtaining a proper fit in this region did require reducing Γ_{cross} by a factor of 10. This will be investigated by independently determining Γ_{cross} within our system. The intermediate region displays the correct qualitative behavior but overestimates the value

of the inverted population. It is unknown exactly why this is the case, but it is clear that the vacancy clusters within our system need to be properly characterized, with their concentration and lattice relaxation times determined precisely. Hopefully by doing this we will help improve the qualitative results of the spin flip-flop model. It also remains to be seen if the spin flip-flop rate Γ_{flip} can be altered by tilting the magnetic field and changing the detuning between the P1 and VC centers, as is the case with the NV thermal maser. This would be strong evidence that our model is correct and that the primary mechanism of operation is a result of spin flip-flop interactions between P1 and VC centers.

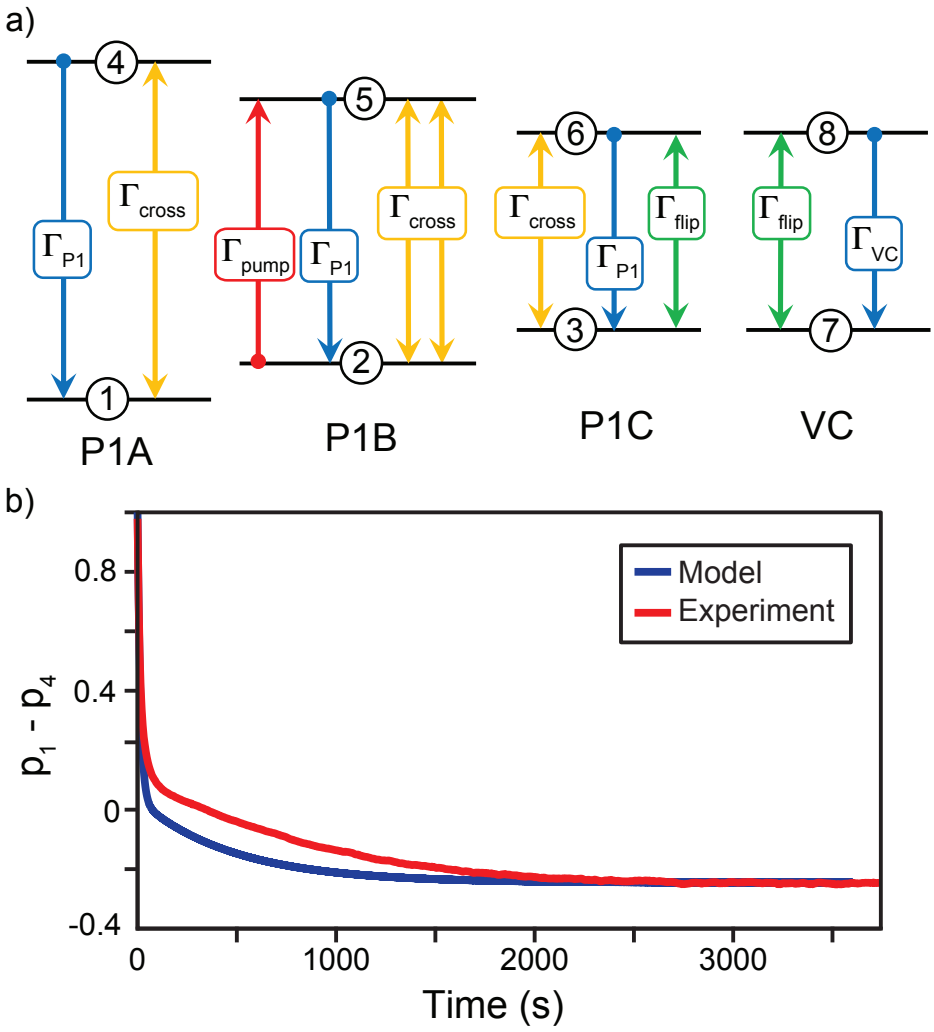

Figure 6.4: Simulation of P1 maser. a) The energy levels and terms used in the rate equations model for the three P1 transitions and the VC lower transition. b) Population difference between level 1 and level 4 as a function of time. Experimental results were calculated from the $K(\omega)$ data presented in Fig. 6.3, whereas the simulated populations p_1 and p_4 are determined by solving Eq. 6.6. The fast-response ($t < 50\,\mathrm{s}$) and steady-state regimes ($t > 2000\,\mathrm{s}$) are well-described by the rate equations, with some discrepancy in the intermediate region. Nonetheless, the model qualitatively reproduces the behavior of the P1 maser.

Noise temperature calculation

In order to estimate the noise temperature of the spin amplifier, we measure the respective gain and noise temperature of each amplifier in the chain sequentially, working backwards. In our setup (see Fig. B.2) we have a three-amplifier chain, consisting of the spins (0.01 mK), the HEMT amplifier (4 K), and the room-temperature (RT) amplifier (297 K). The total noise temperature can thus be calculated by Eq. 2.21,

$$P_{nf} = k_B \Delta f \times G_{RT}[G_{HEMT}[G_{spins}(T_N + T_{spins}) + T_{N,HEMT}] + T_{N,RT}], \tag{6.9}$$

where G_{RT}, G_{HEMT}, and G_{spins} are the gains of the room-temperature (RT) amplifier, 4 K cryogenic (HEMT) amplifier, and the spin maser amplifier, respectively. The corresponding noise temperatures of the amplifiers are $T_{N,RT}$, $T_{N,HEMT}$, and T_N, whereas the actual spin temperature of the maser amplifier is given by T_{spins}. See the relevant section in Ch. 2 for the derivation of the formula. The procedure for measuring the RT amplifier is as follows:

1. Disconnect the input line from the RT amplifier and terminate with a 50 Ω resistor.
2. Connect the amplifier output to the spectrum analyzer (SPA).
3. Set the detection bandwidth of the SPA to 1 kHz and measure the power spectrum.
4. Calculate $T_{N,RT}$ via Eq. 2.21, removing the HEMT and spin terms.

Likewise, we repeat the procedure for the HEMT / RT amplifier chain. We reconnect the RT amplifier to the DR return line and observe the change in the SPA power spectrum, which allows the determination of T_{HEMT} by Eq. 2.21 when the spin terms are removed.

Finally, we can calculate the noise temperature of the spins. After turning on the pump, properly calibrating the cancellation line, and waiting for the inversion to be established, we record the change in the SPA reading. The gain of the spins is determined from the data presented in Fig. 6.3. We use the following table of values for the final calculation.

Parameter	Value
Δf	1000 Hz
G_{RT}	302
G_{HEMT}	1320
G_{spins}	724
T_{RT}	2000 K
T_{HEMT}	2.7 K

Table 6.1: The parameters measured for each of the amplifiers in the measurement chain. Note that the values of the amplifier gains are represented as linearized values as opposed to dB.

With all the amplifiers connected in a chain, the noise floor was measured with an SPA to be -86.1 dBm over the bandwidth, which corresponds to 2.45 pW. Note that the

value of gain for the spin amplifier was measured using different cavity parameters and thus is different from the previous section. Using the above formula, we extract a value $T_N + T_{N,spins} = 0.61\,\mathrm{K}$, which corresponds to an added noise in terms of number of photons equal to

$$n_{th} = \frac{2k_B(0.61\,\mathrm{K})}{h(6.383\,\mathrm{GHz})} \approx 4. \tag{6.10}$$

Which is near the quantum limit of $n_{th} = 1/2$, however the amplifier needs to be further optimized in order to reach truly quantum-limited amplification.

6.2.2 Free-running maser

We now determine if the maser is capable of operating in self-oscillation mode. As we have calculated previously, the inversion ratio is high enough that it should be detectable. The experimental setup is mostly identical to that of the pump-probe experiments, see App. B. The magnetic field is fixed to be resonant with P1A and the pump is applied off-resonantly at $f_{pump} = 6.292\,\mathrm{GHz}$ and power $P_{in} = -36\,\mathrm{dBm}$. The cancellation tone is calibrated prior to measurement. In this case we do not apply the probe tone to the cavity; the return line is connected to the SPA (500 Hz bandwidth) and the results are monitored there. The data can be seen in Fig. 6.5. After around ten minutes of pumping, the threshold condition is met and the system begins emitting microwave photons. The magnitude of the signal remains relatively consistent in amplitude and drifts in frequency over a range of 10-20 kHz.

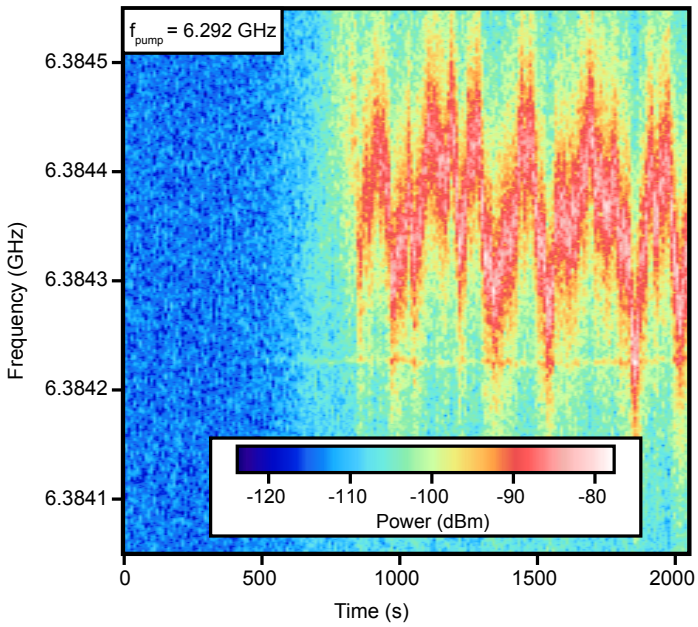

Figure 6.5: Observation of a self-oscillating maser in diamond. A pump tone is applied at 6.292 GHz, while the response is measured using a spectrum analyzer. No probe tone is applied. After more than ten minutes of pumping, the threshold is suddenly surpassed and the P1 satellite begins to emit microwave photons. The center frequency shifts in time over a range of about 15 kHz, while the amplitude remains relatively steady.

Using the profile of the SPA, the linewidth of the maser signal is calculated to 40 kHz, assuming a Lorentzian spin distribution, and the maximum power output is around 2 nW. We will compare this value to a theoretical value based in the number of spins. Recall the formula for P_{out} which we used to define the maser threshold in Ch. 3,

$$P_{out} = \frac{\Delta N B E_{tot} \hbar \omega}{\mathcal{V}_c}, \tag{6.11}$$

where ΔN is the number of inverted spins, B is the Einstein coefficient for stimulated emission given by $B = 3\pi^2 c^3 \gamma_{rad}/\hbar\omega^3$, and $E_{tot}/\mathcal{V}_c$ the total amount of electromagnetic energy per volume contained in the resonator mode. This value can be represented in terms of the oscillating magnetic field δB as

$$E_{tot}/\mathcal{V}_c = \frac{1}{2}\frac{1}{2\mu_0}|\delta B|^2. \tag{6.12}$$

Combining these expressions and using previously determined values for the variables, we get

$$\begin{aligned} P_{out} &= \frac{3\pi^2 c^3 \gamma_{rad} \Delta N |\delta B|^2}{4\mu_0 \omega^2} \\ &= \frac{3\pi^2 c^3 (5\times 10^{-13}\,\mathrm{Hz})(6.6\times 10^{14})|14\times 10^{-12}\,\mathrm{T}|^2}{4\mu_0 (2\pi \times 6.383\times 10^9\,\mathrm{Hz})^2} \\ &= 6.2\,\mathrm{nW}. \end{aligned} \tag{6.13}$$

The measured power is roughly 1/3 of this value, although there is a significant degree of noise in the measured power spectrum. A more thorough or faster measurement with a higher amount of averaging may be needed to smooth out the SPA spectrum.

We also wish to calculate the mean photon number n_{ph} inside the cavity in order to determine if the P1 maser is truly in the oscillation regime. Unlike traditional optical lasers, which can have an extremely large number of modes, our P1 maser only contains one microwave cavity mode within the linewidth of the spins. The time evolution of the inverted population and total photon number can be determined through a series of rate equations, and the steady-state solution for n_{ph} is determined in Ref. [136] to be

$$n_{ph} = \frac{1}{2\beta}\left(-(1-\beta\tilde{P}) + \sqrt{(1-\beta\tilde{P})^2 + 4\beta^2\tilde{P}}\right), \tag{6.14}$$

where β is the fraction of photons emitting into the main laser (or maser) mode and is ≈ 1 in our case. $\tilde{P} = P/\kappa_{tot}$ is the input power normalized by the total cavity linewidth [136]. In the case where $\beta \approx 1$, the above equation becomes linear and simplifies to

$$n_{ph} = \frac{P}{\kappa_{tot}}. \tag{6.15}$$

Likewise, the inverted population N can be determined in terms of P and β through the rate equations, and the steady-state solution is [136]

$$N = \frac{P/\gamma_{rad}}{\beta n + 1}. \tag{6.16}$$

By combining Eqs. 6.15 and 6.16 and eliminating P we arrive at

$$n_{ph} = \frac{\gamma_{rad} N}{\kappa_{tot} - \gamma_{rad} N}. \tag{6.17}$$

Into this equation we substitute the inverted population at the threshold, $N_{th} \approx 2 \times 10^{14}$, the total linewidth $\kappa_{tot} = 12\,\text{MHz}$, and the Purcell rate $10^{-7}\,\text{Hz}$ determined in Ch. 3, obtaining

$$n_{ph} \sim \mathcal{O}(1). \tag{6.18}$$

This is the expected result. The number of cavity photons at the threshold is given by the square root of the number of available modes [127]. For our case, there is only one mode and thus $n_{ph} = 1$. Our results support the conclusion that our maser has entered the self-oscillating regime.

6.3 Summary and perspectives

We have demonstrated a cw spin maser based on P1 centers in diamond, as the result of asymmetric relaxation due to spin flip-flop interactions between P1C and local vacancy clusters (VCs). Unlike previous maser schematics in diamond [35], our P1-based maser operates at millikelvin temperatures and is pumped with microwave frequencies as opposed to optical. The maser can act as a microwave amplifier, having a low noise as well as a

satisfactory gain-bandwidth product that could be made higher through improvements to the resonator and coupling setups. As mentioned in Ch. 2, it is possible that the dynamic range could be quite large, on the order of $50 - 70$ dBm, and with a high saturation power given the number of spins [66]. Even in its current state, the maser can enter self-oscillation mode after being pumped for 10 minutes, generating a few nanowatts of power with a linewidth of order 40 kHz. If sufficiently optimized, such a spin maser could be used for quantum technology applications such as a low-noise amplifier or microwave source operating at millikelvin temperature.

Conclusion and Perspectives

Spin defects in diamond for quantum technologies

In this thesis work we have developed and tested microwave loop-gap resonators (LGR), initially for use as a quantum transducer, and have been able to demonstrate strong coupling between the LGR and ensembles of both P1 and NV centers in diamond at millikelvin temperatures. Additionally, we have shown that diamond also contains a significant number of additional defects; most prominently triple-vacancy chains (R5). These centers have much shorter relaxation times than P1 and NV centers, and thus the net effect of accelerating the lattice relaxation times of the normally long-lived P1 and NV centers due to spin flip-flop interactions. Using cw-microwave spectroscopy we were able to estimate the D-tensors of the R5 centers' spin Hamiltonian.

We have discovered two different maser effects, both of which are a result of spin flip-flops with R5 centers or other, longer vacancy chains. The first effect was a thermal maser using NV centers, where the pumping energy was provided by heat alone. By warming the sample to 4 K and cooling it back to $<$20 mK, a population inversion was created between the $m_s = -1$ and $m_s = 0$ energy levels of NV. The inverted state was incredibly long-lived, with its rise time and decay time governed by the relaxation rates of the R5 and NV centers, respectively. A rate-equation model was developed alongside the measurements, which could extract the spin flip-flop rate Γ_{flip} from the data. We found that Γ_{flip} had a dependence on the detuning between R5 and NV, and matched well with the estimated R5 parameters. The maser threshold was not met in this particular configuration, but should be achievable.

The second effect was a cw maser effect using the P1 centers in diamond. As a result of asymmetric interactions between the satellites of the P1 centers themselves and nearby vacancy cluster centers, population inversion was achieved on one of the P1 satellites. This effect could be used as an amplifier, providing over 30 dB of gain to the microwave probe tone with near quantum-limited added noise ($\sim 0.6\,\mathrm{K}$). In this case the inversion is large enough to overcome the maser threshold and enter the self-oscillation regime. Given more optimization of the power and bandwidth, a spin maser based on diamond could potentially compete with other common microwave amplification technology, particularly Josephson parametric amplifiers.

Let us briefly highlight two projects in which the loop-gap resonator and diamond maser could be developed further.

Future research directions

The traveling-wave maser amplifier

One of the major drawbacks of a cavity maser is the limited gain-bandwidth product and fixed operation frequency. For a maser amplifier to be competitive with Josephson parametric amplifiers, these issues must be addressed. One potential solution is to move from a 3D resonant-cavity geometry to a 2D traveling wave guide geometry. This removes the resonance condition and allows operation over a wider frequency range while still preserving the desirable attributes of the spin maser such as a large gain and low noise power. Demonstration of such a device exist in the early maser era[65], but to our knowledge have never been implemented for quantum information purposes at millikelvin temperatures.

The quantum transducer

The realization of a quantum network requires the ability to coherently and bidirectionally convert between microwave and optical photons, i.e. a quantum transducer with unity efficiency. One scheme for achieving such a device involves an ensemble of solid-state spins coupled to a loop-gap resonator and optical (Fabry-Perot) cavity simultaneously. The geometry of the LGR allows for the maximum mode overlap between the optical and microwave fields, and the quality factor can be high enough that unit efficiency could be achieved [13]. This was, in fact, the initial motivation for designing the resonator in such a way. However, the large optical linewidth of NV centers disqualifies them from consideration in such a device. For this reason, another spin system will need to be used, whether it is rare-earth ions in crystals or another diamond color center such as negatively-charged silicon vacancy centers.

Bibliography

[1] D. M. Pozar. *Microwave Engineering.* John Wiley & Sons, Inc., 3rd ed. edition, 2005.

[2] J. Aumentado. Superconducting Parametric Amplifiers: The State of the Art in Josephson Parametric Amplifiers. *IEEE Microwave*, 21(8):45–59, 2020.

[3] C. Macklin, K. O'Brien, D. Hover, M. E. Schwartz, V. Bolkhovsky, X. Zhang, W. D. Oliver, and I. Siddiqi. A near-quantum-limited Josephson traveling-wave parametric amplifier. *Science*, 350(6258):307–310, 2015.

[4] A. P. Higginbotham, P. S. Burns, M. D. Urmey, R. W. Peterson, N. S. Kampel, B. M. Brubaker, G. Smith, K. W. Lehnert, and C. A. Regal. Harnessing electro-optic correlations in an efficient mechanical converter. *Nature Phys*, 14(10):1038–1042, October 2018.

[5] R. W. Andrews, R. W. Peterson, T. P. Purdy, K. Cicak, R. W. Simmonds, C. A. Regal, and K. W. Lehnert. Bidirectional and efficient conversion between microwave and optical light. *Nat. Phys.*, 10(4):321–326, 2014.

[6] M. Forsch, R. Stockill, A. Wallucks, I. Marinković, C. Gärtner, Richard A. Norte, Frank van Otten, Andrea Fiore, Kartik Srinivasan, and Simon Gröblacher. Microwave-to-optics conversion using a mechanical oscillator in its quantum ground state. *Nat. Phys.*, 16(1):69–74, January 2020.

[7] M. Mirhosseini, A. Sipahigil, M. Kalaee, and O. Painter. Superconducting qubit to optical photon transduction. *Nature*, 588(7839):599–603, December 2020.

[8] A. Rueda, F. Sedlmeir, M. C. Collodo, U. Vogl, Birgit Stiller, G. Schunk, D. V. Strekalov, C. Marquardt, J. M. Fink, O. Painter, G. Leuchs, and H. G. L. Schwefel. Efficient microwave to optical photon conversion: an electro-optical realization. *Optica*, 3(6):597, 2016.

[9] C. O'Brien, N. Lauk, S. Blum, G. Morigi, and M. Fleischhauer. Interfacing superconducting qubits and telecom photons via a rare-earth-doped crystal. *Phys. Rev. Lett.*, 113(6):063603, 2014.

[10] S. Blum, C. O'Brien, N. Lauk, P. Bushev, M. Fleischhauer, and G. Morigi. Interfacing microwave qubits and optical photons via spin ensembles. *Phys. Rev. A*, 91(3):033834, 2015.

[11] R. Hisatomi, A. Osada, Y. Tabuchi, T. Ishikawa, A. Noguchi, R. Yamazaki, K. Usami, and Y. Nakamura. Bidirectional conversion between microwave and light via ferromagnetic magnons. *Phys. Rev. B*, 93(17):174427, 2016.

[12] M. Hafezi, Z. Kim, S. L. Rolston, L. A. Orozco, B. L. Lev, and J. M. Taylor. Atomic interface between microwave and optical photons. *Phys. Rev. A*, 85(2), 2012.

[13] L. A. Williamson, Y.-H. Chen, and J. J. Longdell. Magneto-Optic Modulator with Unit Quantum Efficiency. *Phys. Rev. Lett.*, 113(20):203601, 2014.

[14] X. Fernandez-Gonzalvo, Y.-H. Chen, C. Yin, S. Rogge, and J. J. Longdell. Coherent frequency up-conversion of microwaves to the optical telecommunications band in an Er:YSO crystal. *Phys. Rev. A*, 92(6):062313, 2015.

[15] J. H. N. Loubser and J. A. van Wyk. Electron spin resonance in the study of diamond. *Rep. Prog. Phys.*, 41:1201–1248, 1978.

[16] J. Ruan, W. J. Choyke, and W. D. Partlow. Si impurity in chemical vapor deposited diamond films. *Appl. Phys. Lett.*, 58(3):295–297, 1991.

[17] J. Isoya, H. Kanda, Y. Uchida, S. C. Lawson, S. Yamasaki, H. Itoh, and Y. Morita. EPR identification of the negatively charged vacancy in diamond. *Phys. Rev. B*, 45(3):1436–1439, 1992.

[18] J. K. Kirui, J. A. van Wyk, and M. J. R. Hoch. ESR studies of the negative divacancy in irradiated type-I diamonds. *Dia. Rel. Mat.*, 8(8):1569–1571, 1999.

[19] K. Iakoubovskii and A. Stesmans. Dominant paramagnetic centers in 17 O - implanted diamond. *Phys. Rev. B*, 66(4):045406, 2002.

[20] M. W. Doherty, N. B. Manson, P. Delaney, F. Jelezko, J. Wrachtrup, and L. C. L. Hollenberg. The nitrogen-vacancy colour centre in diamond. *Phys. Rep.*, 528(1):1–45, 2013.

[21] G. Burkard. Diamond Spins Shining Bright. *Physics*, 7:131, 2014.

[22] V. Nadolinny, A. Komarovskikh, Y. Palyanov, I. Kupriyanov, Y. Borzdov, M. Rakhmanova, O. Yuryeva, and S. Veber. EPR study of Si- and Ge-related defects in HPHT diamonds synthesized from Mg-based solvent-catalysts. *Phys. Stat. Sol. (A)*, 213(10):2623–2628, 2016.

[23] J. N. Becker, J. Görlitz, C. Arend, M. Markham, and C. Becher. Ultrafast all-optical coherent control of single silicon vacancy colour centres in diamond. *Nat. Comms.*, 7:13512, 2016.

[24] M. V. G. Dutt, L. Childress, L. Jiang, E. Togan, J. Maze, F. Jelezko, A. S. Zibrov, P. R. Hemmer, and M. D. Lukin. Quantum Register Based on Individual Electronic and Nuclear Spin Qubits in Diamond. *Science*, 316(5829):1312–1316, 2007.

[25] T. Astner, J. Gugler, A. Angerer, S. Wald, S. Putz, N. J. Mauser, M. Trupke, H. Sumiya, S. Onoda, J. Isoya, J. Schmiedmayer, P. Mohn, and J. Majer. Solid-state electron spin lifetime limited by phononic vacuum modes. *Nat. Mat.*, 17(4):313–317, 2018.

[26] L. Robledo, L. Childress, H. Bernien, B. Hensen, P. F. A. Alkemade, and R. Hanson. High-fidelity projective read-out of a solid-state spin quantum register. *Nature*, 477(7366):574–578, 2011.

[27] A. Batalov, C. Zierl, T. Gaebel, P. Neumann, I.-Y. Chan, G. Balasubramanian, P. R. Hemmer, F. Jelezko, and J. Wrachtrup. Temporal Coherence of Photons Emitted by Single Nitrogen-Vacancy Defect Centers in Diamond Using Optical Rabi-Oscillations. *Phys. Rev. Lett.*, 100(7):077401, February 2008.

[28] N. B. Manson, J. P. Harrison, and M. J. Sellars. Nitrogen-vacancy center in diamond: Model of the electronic structure and associated dynamics. *Phys. Rev. B*, 74(10):104303, September 2006.

[29] F. Dolde, H. Fedder, M. W. Doherty, T. Nöbauer, F. Rempp, G. Balasubramanian, T. Wolf, F. Reinhard, L. C. L. Hollenberg, F. Jelezko, and J. Wrachtrup. Electric-field sensing using single diamond spins. *Nat. Phys.*, 7(6):459–463, 2011.

[30] P. C. Maurer, G. Kucsko, C. Latta, L. Jiang, N. Y. Yao, S. D. Bennett, F. Pastawski, D. Hunger, N. Chisholm, M. Markham, D. J. Twitchen, J. I. Cirac, and M. D. Lukin. Room-Temperature Quantum Bit Memory Exceeding One Second. *Science*, 336(6086):1283–1286, June 2012.

[31] Y. Kubo, C. Grezes, A. Dewes, T. Umeda, J. Isoya, H. Sumiya, N. Morishita, H. Abe, S. Onoda, T. Ohshima, V. Jacques, A. Dréau, J.-F. Roch, I. Diniz, A. Auffeves, D. Vion, D. Esteve, and P. Bertet. Hybrid Quantum Circuit with a Superconducting Qubit Coupled to a Spin Ensemble. *Phys. Rev. Lett.*, 107(22):220501, 2011.

[32] Cécile Grèzes. *Towards a spin ensemble quantum memory for superconducting qubits.* PhD thesis, University Paris IV, 2016.

[33] A. Angerer, K. Streltsov, T. Astner, S. Putz, Hitoshi Sumiya, S. Onoda, J. Isoya, W. J. Munro, K. Nemoto, J. Schmiedmayer, and J. Majer. Superradiant emission from colour centres in diamond. *Nat. Phys.*, 14(12):1168–1172, 2018.

[34] R. H. Dicke. Coherence in Spontaneous Radiation Processes. *Phys. Rev.*, 93(1):99–110, 1954.

[35] J. D. Breeze, E. Salvadori, J. Sathian, N. McN. Alford, and C. W. M. Kay. Continuous-wave room-temperature diamond maser. *Nature*, 555(7697):493–496, 2018.

[36] W. V. Smith, P. P. Sorokin, I. L. Gelles, and G. J. Lasher. Electron-Spin Resonance of Nitrogen Donors in Diamond. *Phys. Rev.*, 115(6):1546–1552, 1959.

[37] K. Iakoubovskii and G. J. Adriaenssens. Optical transitions at the substitutional nitrogen centre in diamond. *J. Phys.: Condens. Matter*, 12:6, 2000.

[38] P. P. Sorokin, G. J. Lasher, and I. L. Gelles. Cross Relaxation Studies in Diamond. *Physical Review*, 118(4):939–945, 1960.

[39] E. J. Kamp, B. Carvajal, and N. Samarth. Continuous wave protocol for simultaneous polarization and optical detection of P1-center electron spin resonance. *Phys. Rev. B*, 97(4):045204, 2018.

[40] F A Raal. A spectrographic study of the minor element content of diamond. *Am. Minerologist*, 42:354–361, 1957.

[41] W. Kaiser and W. L. Bond. Nitrogen, A Major Impurity in Common Type I Diamond. *Phys. Rev.*, 115(4):857–863, 1959.

[42] N. A. Poklonski, N. M. Lapchuk, and T. M. Lapchuk. Inverted EPR signal from nitrogen defects in a synthetic diamond single crystal at room temperature. *Jo. Expt. Theoret. Phys. Lett.*, 80(12):748–751, 2004.

[43] N. A Poklonski, N. M Lapchuk, A. V Khomich, L. Fan-Xiu, T. Wei-Zhong, V. G Ralchenko, I. I Vlasov, M. V Chukichev, and S. Munkhtsetseg. Nitrogen-Doped Chemical Vapour Deposited Diamond: a New Material for Room-Temperature Solid State Maser. *Chi. Phys. Lett.*, 24(7):2088–2090, 2007.

[44] C. Ma, Z. Wang, Y. Wu, Z. Bao, Y. Song, H. Zhang, and L. Duan. Four-spin cross relaxation in a hybrid quantum device. *Phys. Rev. A*, 100(1):012322, 2019.

[45] R. Hanson, O. Gywat, and D. D. Awschalom. Room-temperature manipulation and decoherence of a single spin in diamond. *Phys. Rev. B*, 74(16):161203, 2006.

[46] J. R. Maze, J. M. Taylor, and M. D. Lukin. Electron spin decoherence of single nitrogen-vacancy defects in diamond. *Phys. Rev. B*, 78(9):094303, 2008.

[47] J. A. van Wyk, E. C. Reynhardt, G. L. High, and I. Kiflawi. The dependences of ESR line widths and spin - spin relaxation times of single nitrogen defects on the concentration of nitrogen defects in diamond. *J. Phys. D: Appl. Phys.*, 30(12):1790–1793, 1997.

[48] D. J. Twitchen, M. E. Newton, J. M. Baker, T. R. Anthony, and W. F. Banholzer. Electron-paramagnetic-resonance measurements on the divacancy defect center R 4 / W 6 in diamond. *Phys. Rev. B*, 59(20):12900–12910, 1999.

[49] M. A. Lea-Wilson, Jenifer N. Lomer, and J. A. Van Wyk. Electron spin resonance of the R4/W6 defect in irradiated diamond. *Phil. Mag. B.*, 72(1):81–89, 1995.

[50] Jenifer N. Lomer and A. M. A. Wild. Electron spin resonance in electron irradiated diamond annealed to high temperatures. *Rad. Eff.*, 17(1-2):37–44, 1973.

[51] R. C. Barklie and J. Guveni. 13C Hyperfine structure and relaxation times of the P1 centre in diamond. *J. Phys. C: Solid State Phys.*, 14(3621):12, 1981.

[52] G. Davies. Current problems in diamond: towards a quantitative understanding. *Physica B: Cond. Matt.*, 273-274:15–23, 1999.

[53] J. H. N. Loubser and W. P. van Ryneveld. Electronic Spin Resonance of Nickel in Synthetic Diamonds. *Nature*, 211:517, 1966.

[54] A. Einstein. On the quantum theory of radiation, 1917.

[55] N. G. Basov and A. M. Prokhorov. Theory of the molecular generator and molecular power amplifier. *J. Exptl. Theoret. Phys. (U.S.S.R.)*, 3(3):426–429, 1956.

[56] N. V. Karlov, O. N. Krokhin, and S. G. Lukishova. History of quantum electronics at the Moscow Lebedev and General Physics Institutes: Nikolaj Basov and Alexander Prokhorov. *Appl. Opt.*, 49(25):F32, 2010.

[57] J. P. Gordon, H. J. Zeiger, and C. H. Townes. Molecular Microwave Oscillator and New Hyperfine Structure in the Microwave Spectrum of N H 3. *Phys. Rev.*, 95(1):282–284, 1954.

[58] J. P. Gordon, H. J. Zeiger, and C. H. Townes. The Maser—New Type of Microwave Amplifier, Frequency Standard, and Spectrometer. *Phys. Rev.*, 99(4):1264–1274, 1955.

[59] D. Kleppner, H. M. Goldenberg, and N. F. Ramsey. Theory of the Hydrogen Maser. *Phys. Rev.*, 126(2):603–615, 1962.

[60] N. F. Ramsey and D. Kleppner. Atomic hydrogen maser, June 1966.

[61] N. Bloembergen. Proposal for a New Type Solid State Maser. *Phys. Rev.*, 104(2):324–327, 1956.

[62] H. E. D. Scovil, G. Feher, and H. Seidel. Operation of a Solid State Maser. *Phys. Rev.*, 105(2):762–763, 1957.

[63] J. Weber. Masers. *Rev. Mod. Phys.*, 31(3):681–710, 1959.

[64] F. Arams and S. Okwit. Packaged Tunable L-Band Maser System. *Proc. IRE*, 48(5):866–874, 1960.

[65] W. Chang, J. Cromack, and A. Siegman. Cavity and traveling-wave maser using ruby at S-band. In *WESCON/59 Conference Record*, volume 3, pages 142–150, San Francisco, CA, USA, 1959. Institute of Electrical and Electronics Engineers.

[66] A. Siegman. *Microwave Solid-state Masers*. McGraw-Hill, 1964.

[67] N. Bloembergen, S. Shapiro, P. S. Pershan, and J. O. Artman. Cross-Relaxation in Spin Systems. *Phys. Rev.*, 114(2):445–459, April 1959.

[68] H. E. D. Scovil and E. O. Schulz-DuBois. Three-Level Masers as Heat Engines. *Phys. Rev. Lett.*, 2(6):262–263, 1959.

[69] J. E. Geusic, E. O. Schulz-DuBois, and H. E. D. Scovil. Quantum Equivalent of the Carnot Cycle. *Phys. Rev.*, 156(2):343–351, 1967.

[70] E. O. Schulz-DuBios and H. E. D. Scovil. Thermal Maser, December 1961.

[71] N.G. Basov and N.A. Oraevskii. Attainment of negative tempatures by heating and cooling of a system. *J. Exptl. Theoret. Phys. (U.S.S.R.)*, 44(5):1742–1745, 1963.

[72] M. P. Vaisfel'd, F. S. Imamutdinov, and A. Kh. Khasanov. Inverse population in a paramagnetic crystal produced as a result of thermal excitation of the spin system by a pulsed magnetic field. *J. Exptl. Theoret. Phys. Lett. (U.S.S.R.)*, 34(5):240–242, 1981.

[73] M. P. Vaisfel'd, F. S. Imamutdinov, and A. Kh. Khasanov. Maser effect due to thermal excitation of the spin system in a paramagneticcrystal by a pulsed magnetic field. *J. Exptl. Theoret. Phys. (U.S.S.R.)*, 84:2168–2179, 1983.

[74] F. S. Imamutdinov and A. Kh. Khasanov. Conversion of thermal energy of a heater into coherent microwave radiation in a paramagnetic crystal. *Sov. Phys. Solid State*, 26(11):1949–1951, 1984.

[75] M. P. Vaisfel'd. Feasibility of stationary cw maser effect on thermal and microwave excitation of paramagnetic crystals. *J. Exptl. Theoret. Phys. (U.S.S.R.)*, 89:1280–1288, 1985.

[76] John D. Anderson. *Gasdynamic Lasers: An Introduction.* Academic Press, 1976.

[77] M. S. Reid. Low-noise systems in the deep space network, 2008.

[78] A. L. Schawlow and C. H. Townes. Infrared and Optical Masers. *Phys. Rev.*, 112(6):1940–1949, 1958.

[79] T. H. Maiman. Simulated Optical Radiation in Ruby. *Nature*, 187:493–494, 1960.

[80] M. Oxborrow, J. D. Breeze, and N. M. Alford. Room-temperature solid-state maser. *Nature*, 488(7411):353–356, 2012.

[81] L. Jin, M. Pfender, N. Aslam, P. Neumann, S. Yang, J. Wrachtrup, and R.-B. Liu. Proposal for a room-temperature diamond maser. *Nat. Comms.*, 6(1):8251, 2015.

[82] Y.-Y. Liu, J. Stehlik, C. Eichler, M. J. Gullans, J. M. Taylor, and J. R. Petta. Semiconductor double quantum dot micromaser. *Science*, 347(6219):285–287, 2015.

[83] H. Nyquist. Thermal Agitation of Electric Charge in Conductors. *Phys. Rev.*, 32(1):110–113, 1928.

[84] W. Shockley. The Theory of p-n Junctions in Semiconductors and p-n Junction Transistors. *Bell Sys. Tech. J.*, page 55, 1949.

[85] D. Kahng and M. Atalla. Silicon-silicon dioxide field induced surface devices. In *IRE Solid-State Device Research Conference*, Carnigie Institute of Technology, 1960.

[86] T. Mimura. The early history of the high electron mobility transistor (HEMT). *IEEE Trans. Microwave Theory Techn.*, 50(3):780–782, 2002.

[87] R. Dingle, H. L. Störmer, A. C. Gossard, and W. Wiegmann. Electron mobilities in modulation-doped semiconductor heterojunction superlattices. *Appl. Phys. Lett.*, 33(7):665–667, 1978.

[88] T. Mimura. Development of High Electron Mobility Transistor. *Jpn. J. Appl. Phys.*, 44(12):8263–8268, 2005.

[89] A. Wallraff, D. I. Schuster, A. Blais, L. Frunzio, R.-S. Huang, J. Majer, S. Kumar, S. M. Girvin, and R. J. Schoelkopf. Strong coupling of a single photon to a superconducting qubit using circuit quantum electrodynamics. *Nature*, 431(7005):162–167, 2004.

[90] H. Zimmer. Parametric amplification of microwaves in superconducting Josephson tunnel junctions. *Appl. Phys. Lett.*, 10(7):193–195, 1967.

[91] C. M. Caves. Quantum limits on noise in linear amplifiers. *Phys. Rev. D*, 26(8):1817–1839, 1982.

[92] R. Movshovich, B. Yurke, P. G. Kaminsky, A. D. Smith, A. H. Silver, R. W. Simon, and M. V. Schneider. Observation of zero-point noise squeezing via a Josephson-parametric amplifier. *Phys. Rev. Lett.*, 65(12):1419–1422, 1990.

[93] M. A. Castellanos-Beltran and K. W. Lehnert. Widely tunable parametric amplifier based on a superconducting quantum interference device array resonator. *Appl. Phys. Lett.*, 91(8):083509, 2007.

[94] T. Yamamoto, K. Inomata, M. Watanabe, K. Matsuba, T. Miyazaki, W. D. Oliver, Y. Nakamura, and J. S. Tsai. Flux-driven Josephson parametric amplifier. *Appl. Phys. Lett.*, 93(4):042510, 2008.

[95] R. Vijay, D. H. Slichter, and I. Siddiqi. Observation of Quantum Jumps in a Superconducting Artificial Atom. *Phys. Rev. Lett.*, 106(11):110502, 2011.

[96] C. Eichler and A. Wallraff. Controlling the dynamic range of a Josephson parametric amplifier. *EPJ Qu. Tech.*, 1(1):2, 2014.

[97] M. Göppl, A. Fragner, M. Baur, R. Bianchetti, S. Filipp, J. M. Fink, P. J. Leek, G. Puebla, L. Steffen, and A. Wallraff. Coplanar waveguide resonators for circuit quantum electrodynamics. *Journal of Applied Physics*, 104(11):113904, 2008.

[98] C. W. Gardiner and M. J. Collett. Input and output in damped quantum systems: Quantum stochastic differential equations and the master equation. *Physical Review A*, 31(6):3761, 1985.

[99] C.P. Slichter. *Principles of Magnetic Resonance.* Springer, second revised and expanded edition, 1980.

[100] A. Abragam. *Principles of Nuclear Magnetism.* Clarendon Press, 1961.

[101] R. P. Feynman, F. L. Vernon, and R. W. Hellwarth. Geometrical Representation of the Schrödinger Equation for Solving Maser Problems. *J. Appl. Phys.*, 28(1):49–52, 1957.

[102] A. Schweiger and G. Jeschke. *Principles of pulse electron paramagnetic resonance*. Oxford University Press, 2001.

[103] F. Bloch. Nuclear Induction. *Phys. Rev.*, 70(7-8):460–474, 1946.

[104] F. Bloch, W.W. Hansen, and M. Packard. The Nuclear Induction Experiment. *Phys. Rev.*, 80(7-8):474–485, 1946.

[105] H. Y. Carr and E. M. Purcell. Effects of diffusion on free precession in nuclear magnetic resonance experiments. *Physical Review*, 94(3):630–638, 1954.

[106] T. A. Kennedy, J. S. Colton, J. E. Butler, R. C. Linares, and P. J. Doering. Long coherence times at 300 K for nitrogen-vacancy center spins in diamond grown by chemical vapor deposition. *Appl. Phys. Lett.*, 83(20):4190–4192, November 2003.

[107] Susumu Takahashi, Ronald Hanson, Johan van Tol, Mark S. Sherwin, and David D. Awschalom. Quenching Spin Decoherence in Diamond through Spin Bath Polarization. *Phys. Rev. Lett.*, 101(4):047601, July 2008.

[108] E. L. Hahn. Spin Echoes. *Phys. Rev.*, 80(4):580–594, 1950.

[109] S. Meiboom and D. Gill. Modified Spin-Echo Method for Measuring Nuclear Relaxation Times. *Rev. Sci. Instr.*, 29:688–691, 1958.

[110] W. M. Walsh and L. W. Rupp. Enhanced ESR sensitivity using a dielectric resonator. *Rev. Sci. Instr.*, 57(9):2278–2279, 1986.

[111] A. C. Torrezan, T. P. Mayer Alegre, and G. Medeiros-Ribeiro. Microstrip resonators for electron paramagnetic resonance experiments. *Rev. Sci. Instr.*, 80(7):075111, 2009.

[112] S. Haroche and J.-M. Raimond. *Exploring the Quantum*. Oxford University Press, 2006.

[113] I. I. Rabi. On the process of space quantization. *Physical Review*, 49(4):324, 1936.

[114] E. T. Jaynes and F. W. Cummings. Comparison of Quantum and Semiclassical Radiation Theories with Application to the Beam Maser. *Proceedings of the IEEE*, 51(1):89–109, 1963.

[115] M. Tavis and F.W. Cummings. Approximate solutions for an N-molecule-radiation-field Hamiltonian. *Physical Review*, 188(2):692–695, 1969.

[116] C. W. Zollitsch. *Single Excitation Transfer in the Quantum Regime: A Spin-Based Solid-State Approach*. PhD thesis, Technical University of Munich, 2016.

[117] I. Diniz, S. Portolan, R. Ferreira, J. M. Gérard, P. Bertet, and A. Auffèves. Strongly coupling a cavity to inhomogeneous ensembles of emitters: potential for long-lived solid-state quantum memories. *Phys. Rev. A*, 84(6):063810, 2011.

[118] Z. Kurucz and K. Mølmer. Multilevel Holstein-Primakoff approximation and its application to atomic spin squeezing and ensemble quantum memories. *Physical Review A*, 81(3), 2010.

[119] T. Holstein and H. Primakoff. Field dependence of the intrinsic domain magnetization of a ferromagnet. *Physical Review B*, 58:1098–1113, 1940.

[120] Z. Kurucz, J. H. Wesenberg, and K. Mølmer. Spectroscopic properties of inhomogeneously broadened spin ensembles in a cavity. *Physical Review A*, 83(5), 2011.

[121] Y. Kubo, F. R. Ong, P. Bertet, D. Vion, V. Jacques, D. Zheng, A. Dréau, J.-F. Roch, A. Auffeves, F. Jelezko, J. Wrachtrup, M. F. Barthe, P. Bergonzo, and D. Esteve. Strong Coupling of a Spin Ensemble to a Superconducting Resonator. *Phys. Rev. Lett.*, 105(14):140502, 2010.

[122] B Julsgaard, C. Grezes, P. Bertet, and K. Mølmer. Quantum Memory for Microwave Photons in an Inhomogeneously Broadened Spin Ensemble. *Phys. Rev. Lett.*, 110(25):250503, 2013.

[123] Eisuke Abe, Hua Wu, Arzhang Ardavan, and John J. L. Morton. Electron spin ensemble strongly coupled to a three-dimensional microwave cavity. *Appl. Phys. Lett.*, 98(25):251108, June 2011.

[124] C.P. Slichter. *Principles of Magnetic Resonance*. Springer, 3rd edition, 1990.

[125] E. M. Purcell, H. C. Torrey, and R. V. Pound. Resonance Absorption by Nuclear Magnetic Moments in a Solid. *Phys. Rev.*, 69(37), 1946.

[126] A Bienfait. Controlling spin relaxation with a cavity. *Nature*, 531:74–77, 2016.

[127] A. Siegman. *Lasers*. University Science Books, 1986.

[128] J. R. Ball, Y. Yamashiro, H. Sumiya, S. Onoda, Takeshi Ohshima, J. Isoya, D. Konstantinov, and Y. Kubo. Loop-gap microwave resonator for hybrid quantum systems. *Appl. Phys. Lett.*, 112(20):204102, 2018.

[129] Atac Imamoğlu. Cavity QED Based on Collective Magnetic Dipole Coupling: Spin Ensembles as Hybrid Two-Level Systems. *Phys. Rev. Lett.*, 102(8), 2009.

[130] R. Amsüss, Ch. Koller, T. Nöbauer, S. Putz, S. Rotter, K. Sandner, S. Schneider, M. Schramböck, G. Steinhauser, H. Ritsch, J. Schmiedmayer, and J. Majer. Cavity QED with Magnetically Coupled Collective Spin States. *Phys. Rev. Lett.*, 107(6), 2011.

[131] Stefan Stoll and Arthur Schweiger. EasySpin, a comprehensive software package for spectral simulation and analysis in EPR. *Jo. Mag. Res.*, 178(1):42–55, 2006.

[132] A. Cox, M. E. Newton, and J. M. Baker. ^{13} C, ^{14} N and ^{15} N ENDOR measurements on the single substitutional nitrogen centre (P1) in diamond. *J. Phys.: Condens. Matter*, 6(2):551–563, 1994.

[133] K. Iakoubovskii and A. Stesmans. Characterization of hydrogen and silicon-related defects in CVD diamond by electron spin resonance. *Phys. Rev. B*, 66(19):195207, 2002.

[134] V. Ranjan, G. de Lange, R. Schutjens, T. Debelhoir, J. P. Groen, D. Szombati, D. J. Thoen, T. M. Klapwijk, R. Hanson, and L. DiCarlo. Probing Dynamics of an Electron-Spin Ensemble via a Superconducting Resonator. *Phys. Rev. Lett.*, 110(6), 2013.

[135] S. E. de Graaf, A. A. Adamyan, T. Lindström, D. Erts, S. E. Kubatkin, A. Ya. Tzalenchuk, and A. V. Danilov. Direct Identification of Dilute Surface Spins on Al 2 O 3 : Origin of Flux Noise in Quantum Circuits. *Phys. Rev. Lett.*, 118(5):057703, January 2017.

[136] Naotomo Takemura, Masato Takiguchi, and Masaya Notomi. Low- and high-β lasers in the class-A limit: photon statistics, linewidth, and the laser-phase transition analogy. *J. Opt. Soc. Am. B*, 38(3):699, March 2021.

[137] C. Grezes, B. Julsgaard, Y. Kubo, M. Stern, T. Umeda, J. Isoya, H. Sumiya, H. Abe, S. Onoda, T. Ohshima, V. Jacques, J. Esteve, D. Vion, D. Esteve, K. Mølmer, and P. Bertet. Multimode Storage and Retrieval of Microwave Fields in a Spin Ensemble. *Phys. Rev. X*, 4(2):021049, June 2014.

[138] J. N. Lomer and A. M. A. Wild. *Rad. Eff.*, 17(37), 1973.

[139] C. A. J. Ammerlaan, O. (ed.) Madelung, and M. (ed.) Schulz. Numerical Data and Functional Relationships in Science and Technology. In *Numerical Data and Functional Relationships in Science and Technology*, volume 22 of *New Series*, pages 177–206. Springer, Berlin, 1990.

Appendix A

Information on diamond samples

A.1 Samples #1 and #2

The first two samples used in this work are type-Ib synthetic diamond crystals grown by temperature gradient method at high pressure and high temperature (HPHT). These samples were grown and prepared by Dr. Hitoshi Sumiya at the Advanced Materials R&D Laboratories at Sumitomo Electric Company. The initial nitrogen impurity concentration of Sample #1 was about 40 ppm, which are incorporated during the growth. In order to create highly concentrated NV centers, the crystal was irradiated by 2 MeV electrons with a total fluence of $6 \times 10^{18}\,\mathrm{cm}^{-2}$ at 800° C and annealed at 1000° C in a vacuum for two hours. Sample #2 was also treated in similar way, but started with a lower initial concentration of nitrogen (20 ppm). The sample was also irradiated in two steps, first irradiated at room temperature with a fluence of $5 \times 10^{17}\,\mathrm{cm}^{-2}$ and annealed at 800° C for 5 hours in vacuum. In the second stage it was irradiated at 700° C with a fluence of $5 \times 10^{17}\,\mathrm{cm}^{-2}$. The sample was then finally annealed at 1000° C for 2 hours in vacuum. Sample #2 is the same diamond sample as the one that was used in Ref. [137]. Since Sample #2 is used for the NV thermal maser, here we provide an estimate of the concentration of the R5 centers that act at the spin bath. The formation and behavior of vacancy clusters have been studied as a function of annealing temperature [138] [139], determining an R5 concentration of $10^{17}\,\mathrm{cm}^{-3}$ for an annealing temperature of 1000° C and an electron irradiation fluence of $8 \times 10^{19}\,\mathrm{cm}^{-2}$. Given that the electron fluence used in our sample irradiation was an order of magntitude less, we place a lower bound on the concentration to be 2 ppb, which we use in the main text of Ch. 5.

The impurity concentrations of Samples #1 and #2 are summarized in Table A.1 below, as well as the vertical orientation direction.

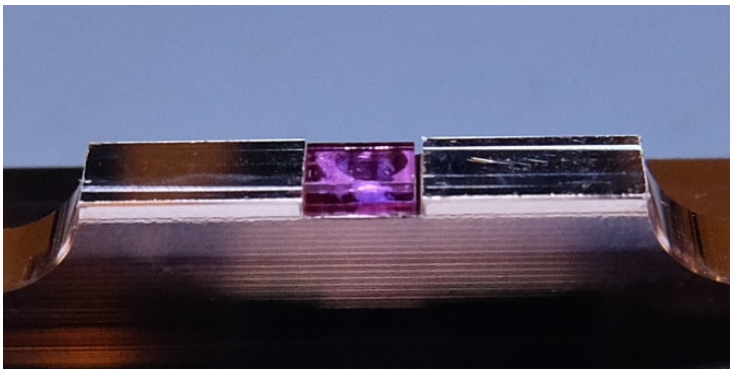

Figure A.1: A picture of Sample #2 when it is loaded into the resonator.

A.2 Sample #3

This sample is also a type-Ib synthetic diamond crystal grown by HPHT method, commercially available for purchase from Sumitomo Electric Company. It is suspected to have a higher nitrogen concentration than the other samples (50-100 ppm), and has not been treated with electron beam irradiation. This means that the concentration of NV centers and other vacancy clusters should be negligible.

The parameters of the samples are listed below. The value of the P1 concentration post-irradiation in Sample #2 is revised from the reported 10 ppm in Ref. [128].

Sample	Size (mm^3)	Orientation	[P1]	[NV]
#**1**	$3 \times 1.5 \times 1.1$	[110]	20 ppm	10 ppm
#**2**	$3 \times 1.5 \times 0.5$	[001]	16 ppm	2 ppm
#**3**	$2.5 \times 2.5 \times 0.5$	[001]	50 ppm	negligible

Table A.1: The parameters of the synthetic diamond samples used in this work. The orientation corresponds to the axis of diamond which is aligned along the diamond's smallest dimension.

Appendix B

Experimental setup information

All of the experiments performed in this thesis take place in a BlueFors dilution refrigerator (DR), a dry cryogenic system which is able to reach temperatures as low as 10 mK. Samples are placed in an enclosure which is thermally anchored to the lowest temperature plate, known as the mixing chamber (MXC), of the DR. Details about the resonator and enclosure are detailed in Ch. 4. Since several types of measurements, involving different wiring and electronic configurations, are performed throughout the work of this thesis, they will be discussed in detail in the subsequent sections.

B.1 Continuous-wave (CW) spectroscopy

B.1.1 The magnet

In all measurements a superconducting magnet, anchored to the 4 K stage of the DR, surrounds the sample and provides the static B-field, as seen in Fig. B.1. The current is provided to the magnet by a DC current source at room temperature, itself controlled by the measurement computer. In experiments from Ch. 4.4 onward, we were able to implement a three-axis vector magnet (American Magnetics, Inc.) to allow arbitrary orientation of the B-field. The only change in the experimental configuration is the addition of two more (identical) DC current sources to provide a magnetic field to each axis.

B.1.2 Transmission measurement

Frequency-domain, alternatively continuous wave (cw), spectroscopy measurements comprise most of experiments performed in this work. Of these measurements, there are two types: transmission and reflection. Early experiments, such as those in [128], are performed by measuring the transmitted power. The room-temperature electronic and DR wiring schemes are shown in Fig. B.1.

When measuring S_{21}, the signal begins at port 1 of the vector network analyzer (VNA), usually outputting power between -30 and -10 dBm. As the probe signal travels through the probe coaxial line (black line) in the DR, thermal noise from room temperature is suppressed by attenuators at several temperature stages. Total power attenuation from the source to the resonator enclosure is about -76 dB at 5-6 GHz, meaning that the power at the resonator is typically in the range of -105 to -85 dBm. The signal transmitted

through the resonator is passed through two isolators, a low pass filter, and then amplified via a HEMT amplifier at 4 K. The isolators serve to prevent noise signals of the HEMT from entering back into the resonator. Passing out of the fridge, the signal is fed through another isolator and room-temperature amplifier. The signal can either be returned to port 2 of the VNA or be diverted to a spectrum analyzer (SPA) if needed, which is coupled into the return line via a directional coupler.

In the cases where a pump signal is needed, this can be provided by a microwave source (MWS) at room temperature and transmitted to the resonator by the pump (green) line. The pump line is less attenuated in order to allow for larger pump powers. The pump and probe lines are joined together via a directional coupler at the lowest temperature stage, configured so that the pump line is attenuated by -10 dBm.

In order to properly calibrate transmission measurements, the amount of attenuation throughout the fridge in the absence of the resonator must be known to a high degree of precision. Given the difficulty of obtaining this information, we decided to reconfigure the wiring inside the DR to measure reflection.

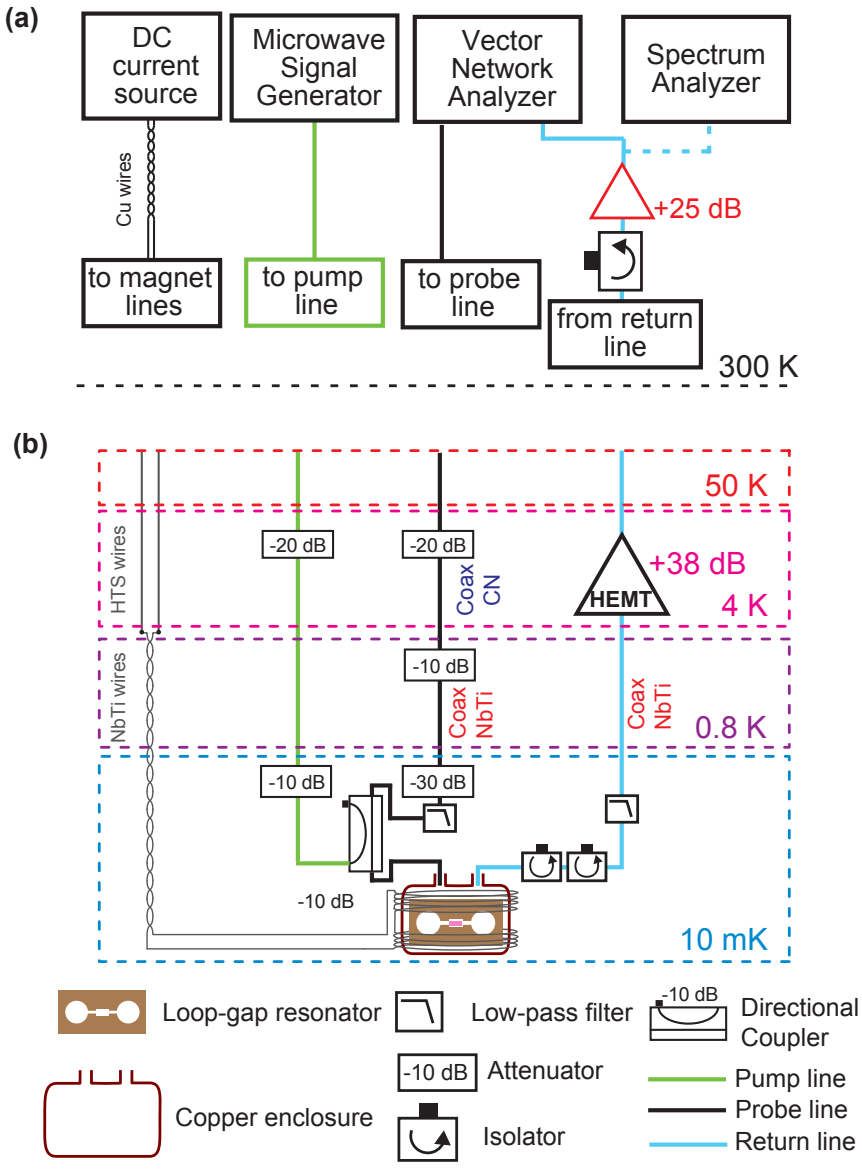

Figure B.1: Experimental setup for cw-microwave transmission spectroscopy. a) Room-temperature electronic setup used in in cw measurements. b) Measurement setup and wiring diagram inside the DR. Symbols used for electronic components are indicated below the diagram.

B.1.3 Reflection measurement

Measuring in reflection allows for much easier calibration of the resonator profile, as off resonance the reflected signal should be ≈ 1, which can then be used as the background level. The room-temperature electronic and DR wiring schemes are shown in Fig. B.2. A few changes are made to the wiring at the mixing chamber of the DR. Two isolators are added to the probe (black) line in order to prevent signal from being reflected back through the line. The probe/pump (black/green) lines terminate at a circulator, which transfers the signal into the resonator, which is then reflected out through the blue line.

Another isolator in the return (blue) line prevents microwave reflection and thermal noise from the HEMT, as done in the transmission measurement. A microwave switch is added to the return line in from of the HEMT. During situations where high power is applied to the resonator (saturation, pumping, pulses), the microwave switch can terminate the signal at the 4 K stage and avoid saturation of the HEMT. The rest of the return line is unchanged.

A pump signal can once again be provided by a microwave source (MWS) at room temperature and transmitted to the resonator by the pump (green) line. In this case, however, we have added a microwave cancellation (red) line. During cases when the probe and pump are applied simultaneously (i.e. the P1 maser in Ch. 6), most of the pump tone, which is detuned from the cavity, gets reflected from the resonator. It is thus necessary to remove (or "cancel") the pump tone so that the much weaker probe tone can be accurately measured by the VNA. This is accomplished by splitting the signal from the microwave signal generator and feeding it through a variable attenuator and phase shifter such that the pump tone and cancellation tone have the same amplitude but 180° out of phase at the lowest temperature. The values of the attenuator and phase shifter are optimized by turning on the pump tone and measuring the results of the cancellation on the SPA, in absence of the probe tone. When the power spectrum measured on the SPA is at a minimum, then the pump tone is well-cancelled.

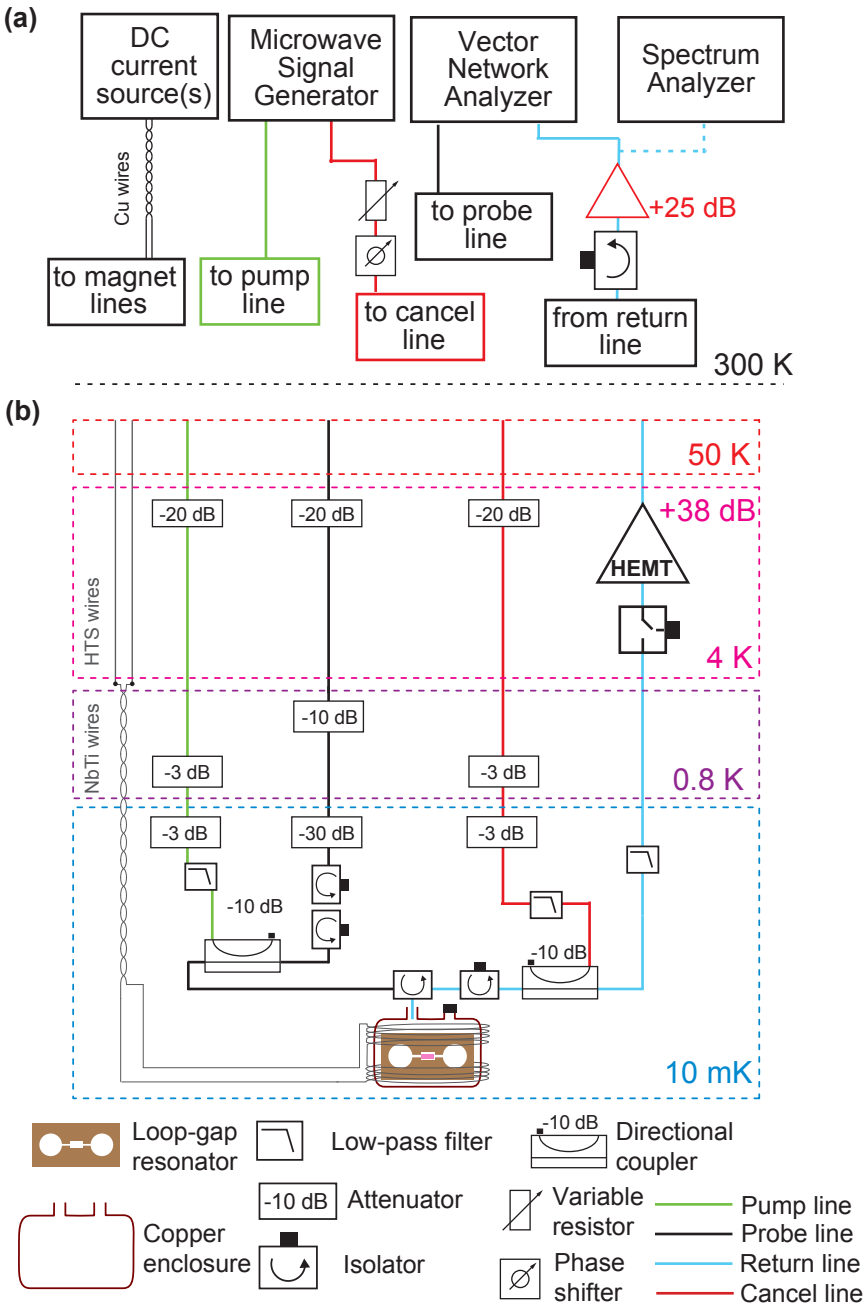

Figure B.2: Experimental setup for cw-microwave reflection spectroscopy. a) Room-temperature electronic setup used in in cw measurements. b) Measurement setup and wiring diagram inside the DR. Symbols used for electronic components are indicated below the diagram.

B.2 Time-domain experiments

For the time-domain measurements performed in Ch. 4, a more complex electronic setup is needed. The wiring inside the DR remained exactly the same as in B.2, and the new schematic for the room temperature electronics can be seen in Fig. B.3. When the

measurement script is started, the pulse sequence is triggered by an arbitrary function generator (AFG). Pulse envelopes of I- and Q-quadratures are generated by the arbitrary waveform generator (AWG), which are then mixed within the microwave signal generator (MSG). The pulses emitted from the MSG is gated via an internal switch and another room-temperature switch to improve the on/off ratio, with the switch also controlled by the the AWG. The pulses are then amplified, and transmitted through the coaxial line in a manner similar to the cw experiments. After amplification at 4 K via the HEMT and again at room temperature, the signal is passed into the RF input of an IQ mixer, where it is demodulated using the original frequency of the MSG as the local oscillator (LO) input. The signal, now down-converted into fast DC I and Q quadratures, is then passed through low-pass filters. The final signal is collected by a fast digitizer board attached to the measurement PC. The digitizer board, AFG, AWG, and MSG are all synchronized by a 10 MHz frequency standard reference. The pulses can also be monitored with a spectrum analyzer.

B.3 Thermal maser experimental procedure

Here we include some extra details about the procedure for initializing the thermal maser, described in Ch. 5. After finding the resonance field of NV1 and keeping the B-field magnitude and angle fixed there, the mixing chamber (MXC) heater of the dilution fridge was supplied with current to raise the sample temperature to 4.5 K. Raising the temperature started to boil the helium mixture, which raised the pressure inside the injection line and thus required some of the ^{3}He/^{4}He mixture to be recollected in the storage tank. This was done by manually opening the valves through which the mixture could return to its storage tank. The heater was kept on for 15 minutes, which allowed all of the spins time to equilibrate according to the Boltzmann distribution. The temperature was kept relatively stable around 4.5 K using a PID temperature controller. After this waiting time the heater was shut off and the mixture that had been collected in the storage tank was re-condensed and injected back into the ^{3}He/^{4}He mixture circulation line of the DR, controlled electronically via a custom script. The MXC temperature return to $<$20 mK within one hour, however the exact amount of time the procedure took tended to vary. This means that the NV1 spins had slightly different amounts of time to relax before the measurement, and it is likely for this reason that the initial population of the NV1 ground state has a degree of variability.

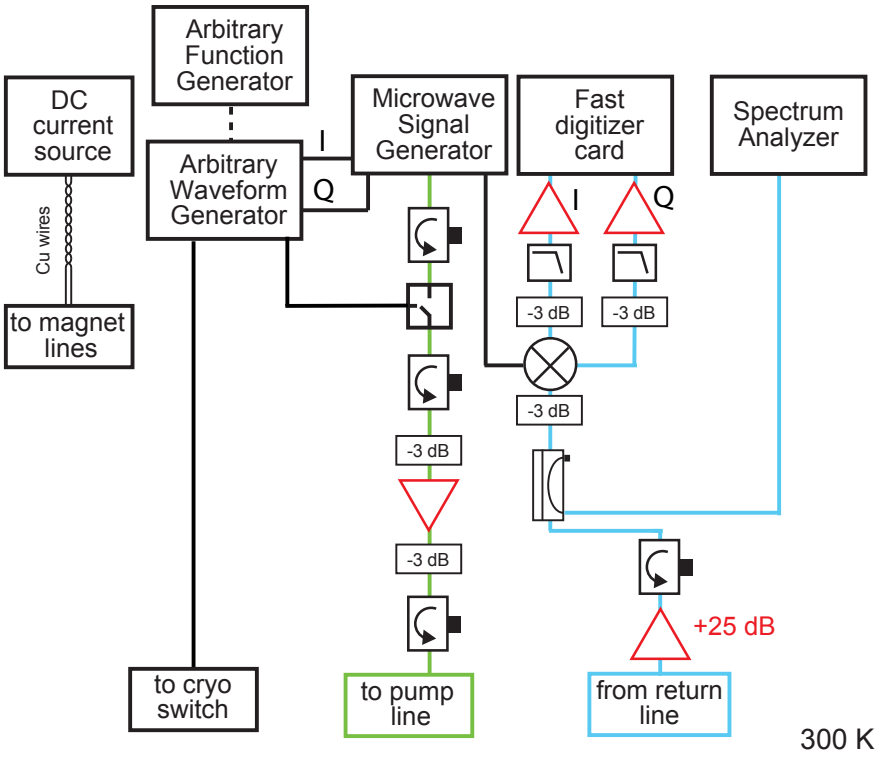

Figure B.3: Experimental setup for time-domain microwave spectroscopy. The room-temperature electronic setup is shown, along with notes where the connections are made to the existing measurement lines inside the DR.